COMPARISON OF LIQUID MERCURY AND HYDROGEN EMBRITTLEMENT ON 4142 STEEL

By

RICHARD GARY NORMAN

Bachelor of Science in Mechanical Engineering

University of Tulsa

Tulsa, Oklahoma

1982

Submitted to the Faculty of the Graduate College
of the Oklahoma State University
in partial fulfillment of the requirements
for the degree of
MASTER OF SCIENCE
December, 1984

COMPARISON OF LIQUID MERCURY

AND HYDROGEN EMBRITTLEMENT

ON 4142 STEEL

Thesis Approved:

C E Lum

Thesis Adviser

J. K. Good

R. L. Lowery

Norman N. Durham

Dean of the Graduate College

PREFACE

A study of liquid mercury and hydrogen embrittlement was conducted on a 4142 steel. A computer program was developed to generate engineering stress-strain graphs in order to further enhance the fractographs of samples from air, mercury or hydrogen environments. This program was developed to use load and displacement values of the MTS machine in the stroke control mode in order to control strain rate accurately. Various axisymmetric geometries may be used and samples of reasonably close geometries may be compared for their respective stress-strain characteristics.

The study revealed that hydrogen and mercury samples do have the intergranular characteristic fractures of adsorption induced reduction in cohesion, but the graphs of comparable mercury and hydrogen samples show a difference. Hydrogen samples break before the nominal yield strength while mercury samples break after yield. Study of this steel reveals trends in strain rate and microstructure worthy of further investigation and is recommended with the aid of the MTS stress-strain program.

To everyone who encouraged me to continue this research at Oklahoma State University, my sincerest thanks. My major advisor, Dr. C. E. Price, I would thank the most for his patience and his thoughtful professional approach to our work.

Dr. Karl Reid and Dr. Wiebelt I would also like to thank for opening the door to study in and work with the Mechanical and Aerospace Engineering Department. To the members of my committee, Drs. J.K. Good and R. L. Lowery, a special thanks for studying instrumentation under them and becoming inspired enough to write a program about it.

The support of my family helped me though months of hard work. Warm appreciation goes to my Mother and Father. Lastly, to the man who inspired me most to finish my education, my heartfelt thanks to my Grandfather, Clarence Norman.

TABLE OF CONTENTS

CHAPTER Page

LIST OF TABLES

LIST OF FIGURES

Figure Page

Figure

Page

Figure

Page

Figure

Page

Figure

Page

LIST OF NOMENCLATURE

LME	Liquid Metal Embrittlement
UNS	Unified Numbering System
HE	Hydrogen Embrittlement
SEM	Scanning Electron Microscope
μ	Micro or 10^{-6}
σ_{max}	Ideal Cleavage Stress
τ_{max}	Ideal Shear Stress
Φ	Fracture Energy
τ^*	Critical Local Shear Strength
K_{IISC}	Shear Stress Crack Fracture Toughness
μ	Chemical Potential
α^1	Austenite, not full FCC
σ_H	Hydrostatic Tensile Stress
V_H	Partial Molar Volume
C_o	Initial Concentration
YS	Yield Strength
SAY	Strain At Yield
FS	Fracture Strength
SEY	Strain Energy to Yield
SEF	Fracture Strain Energy
MPW	Macroscopic Plastic Work

TTF	Time to Failure
RC	Rockwell C Hardness
UTS	Ultimate Tensile Strength
TEM	Transmitting Electron Microscope
MTS	Multiple Testing System

CHAPTER I

INTRODUCTION

In this investigation, Liquid Metal Embrittlement (LME) by mercury of a quenched and tempered 4142 steel (UNS H41420) is compared to Hydrogen Embrittlement (HE). This study follows similar studies by Lynch (1,2,3) upon nickel single crystals, an aluminum alloy containing zinc and magnesium, and titanium 6-4. Lynch recently published a comparative fractographic study of a D6ac steel (4) in which the gaseous H_2 and liquid mercury environments produced similar intergranular fractures on notched three point bend test specimens. Lynch has advocated that dislocation nucleation at crack tips is enhanced by liquid metals and that the mechanism of HE is similar to that of LME. Lynch published the D6ac study on crack propagation while this study was in progress. It did not include stress-strain characteristic curves or cover the crack initiation stage. This report will cover these aspects of LME and HE of 4142 steel.

Hirth (5) outlines many competing mechanisms of HE; however, Lynch shows a striking similarity in fracture of the HE and LME specimens. Comparable surface phenomena occur during HE and LME. This is important because according to Lynch's calculations (4), hydrogen diffuses in steels on the order of 1 μms^{-1}. According to Hirth (5), hydrogen will cause changes in the plastic zone ahead of the crack tip, but, if cracks propagate as fast or faster than hydrogen is transported through

the bulk metal in a specimen not precharged with hydrogen, then the change in surface energy at the crack tip will logically control the fracture and crack growth rate. This feature allows a comparison of HE to LME because both embrittlers are adsorbed at the crack tip (4,5,6).

The adsorption of hydrogen is shown to be an important mechanism of embrittlement by Vehoff and Rothe (7). They knew that oxygen replaced adsorbed hydrogen on {100} surfaces of iron. With equal partial pressures of hydrogen and oxygen, the hydrogen average adsorption rate would decrease 10,000 fold (7). To test this they placed a hydrogen precharged specimen made of Fe-2.6% Si in an all hydrogen environment. The mode of crack growth rate changed within one second after switching the environment from hydrogen to oxygen. If HE is diffusion controlled the change in fracture mode would be less abrupt, therefore the fracture is controlled at the surface. Ficalora and Ransome (8) show the adsorption of hydrogen to be a result of two competing mechanisms which reach a local peak around room temperature. Physical chemisorption increases with increasing temperature whereas an ionic desorption process activates just past room temperature. One way of visualizing the local peak is to imagine that as hydrogen atoms experience a temperature increase, more energy is available to initiate the adsorption reaction with more hydrogen atoms being crowded onto a unit area. Physical chemisorption therefore increases with a temperature increase. The local peak results as electrons are ionized into a higher energy state, which increases the ionic radius. This reduces the number of embrittler atoms able to interact with the surface, thereby reducing adsorption. This ionic desorption is likely a result of the majority of electrons jumping to a higher energy state just past room temperature and would thereafter

remain constant for higher temperatures. Adsorption would again increase with temperature increasing as a result of physical chemisorption increasing.

The adsorption of Hg at the crack tip does bear some relation to the adsorption of H_2 at room temperatures. (See Figure 1 to 4 - All figures will be in Appendix A.) The ability of an embrittler, Hg or H_2, to be adsorbed and change the bulk metal lattice parameter can be seen from equilibrium phase diagrams. If two metals form stable high melting point compounds then embrittlement is unlikely, Kamdar (9). Therefore, miscible metals with similar molar densities, i.e., similar quantity of atoms per unit volume, will be chemi-physically stable. At standard temperature and pressure, the elements will reach a nominal spacing for component atoms which is reflected for example by the molar densities of iron, mercury and hydrogen (see Table I - All tables will be in Appendix B). When a mercury or hydrogen atom adsorbs to an iron surface the severity of embrittlement after adsorption becomes a matter of the local reduction in atomic bond strengths and enhanced shear at stress concentrations like a dislocation pile up or at a crack tip, Stoloff, Ashok, Glicksman, and Slavin (10). If the embrittler forms a different solid crystal with the bulk metal, the adsorption of the embrittler will change the lattice parameter of the surface area. The change in the lattice parameter can either help or hinder embrittlement. For example, oxygen and hydrogen have similar partial molar volumes, but have different common valences and solid crystal structures (see Table I). Their effect on iron alloys is also different. In addition to Vehoff and Rothe (7) discussing oxygen replacing hydrogen, G. Hancock and H. Johnson (11) demonstrated hydrogen embrittlement of steels

whereas oxygen bonded so strongly that its heat of adsorption blocked the hydrogen out and blunted the crack tip advance.

LME has been studied less than HE, but enough to promote periodic reviews by Rostoker, McCaughey and Markus (12), Kamdar (9), Stoloff (13,14) and Nicholas and Old (15). Many specific embrittlement couples have been identified by Kamdar (9) and by Shunk and Warke (16). In all the liquid metal-metal combinations, embrittlement has a prerequisite of plastic deformation, even though macroscopic plastic deformation is not apparent, Stoloff, Ashok, Glicksman, and Slavin (10). This is true of amorphous metals as well as crystalline metals (10).

Stoloff, Ashok, Glicksman, and Slavin (10) show that for four amorphous iron based alloys without crystallographic slip planes or grain boundaries to provide "barriers to plastic deformation" or without "low energy crack paths," the amorphous alloys will have plastic deformation as a result of enhanced localized shear 45^{o} from the stress axis. The macroscopic strains are very small but the amorphous alloys will fracture at yield because localized shear strain is so great. The fractography of samples in hydrogen and liquid Hg-In alloy reveal enhanced shear in both environments. This bears out Lynch's 1977 work (17) of the enhanced shear in environment sensitive cracking materials.

The amorphous iron alloys show shear, mode II fractures, while crystalline iron alloys show cleavage, Mode I, type fractures. One reason that there is a difference in the type of fractography for the embrittlement of both types of alloy is related to the effect the adsorbed liquid metal atom has on reducing the ideal cleavage stress, σ_{max}. Kelly and Gillman (18,19), as attributed by Kamdar (9, p. 304), stated that "if the ratio of largest tensile fracture stress, σ, in the

vicinity of the crack tip to the largest shear stress, τ , . . . is greater than the ratio of the ideal cleavage, σ_{max}, to the ideal shear stress, τ_{max}, then the crack will propagate by cleavage." Thus, cleavage in high strength steels is intergranular and indicates brittle fracture. Generally, for $\sigma/\tau \leq 10$ fracture is by cleavage. For $\sigma/\tau > 20$ then fracture is primarily shear. Therefore the embrittler atom reduces σ_{max} with respect to τ_{max} where τ_{max} is a function of internal properties subject to tempering, alloy, and cold working. Gillman's criteria applies to crystalline structures but the iron based amorphous alloys of Stoloff, Ashok, Glicksman, and Slavin (10) also show a quasicleavage type of fracture.

CHAPTER II

LITERATURE REVIEW

1. Susceptibility to Embrittlement

A figure by Miller (20), (Figure 5), illustrates the relation of the resistance of metals to liquid metal corrosive attack. For example, chromium nickel steel shows poor resistance to mercury but mild carbon steel is reduced by gallium and not by mercury. Liquid metal corrosion is only one micro-mechanism driving embrittlement but it does emphasize that chemistry, the anodic corrosion as a function of electronegativity, has a role in the severity of embrittlement. Westwood, Preece, and Kamdar (21) have shown embrittlement is most severe when the electronegativity of the liquid metal is equal to the electronegativity of the solid metal. Table I illustrates the relation of electronegativities and valences when compared to Figure 5 and Table II of a few of the known embrittlement couples. The susceptibility as a function of corrosion (Figure 5), of a liquid metal embrittling a solid metal when compared to the closeness of their respective valence (Table I) generally parallels but sometimes contrasts with the severity of the embrittlement when compared to their respective electronegativities (Table I). In other words, susceptibility to embrittlement as measured by the closeness of valences of an embrittlement couples is loosely allied to the severity of embrittlement which is a function of the closeness of

electronegativities of the embrittlement couple.

Microstructural changes occur during tempering. These changes reported by Tsutsui (22) in a chromium molylbdenum steel and by Bernabi, Bombari, and Borruto (23) in a chromium manganese steel create conditions of extreme hydrogen embrittlement. Tsutsui (22) showed a maximum hydrogen embrittlement that occurred with the chromium molybdenum steel tempered at 400 C while Bernabi, Bombari, and Borruto (23) reveal similar maximum hydrogen embrittlement for their steel tempered at 500 C. These tempers in their respective steels are reported (22,23) to cause the most grain boundary segregation and temper embrittlement. Davies (24) determined in a tempered low alloy steel that for less than 10 percent martensite there is no significant HE. Above 10 percent, the severity of embrittlement increases with increasing martensite content. A plateau of embrittlement is obtained around 30 percent martensite (i.e., the elongation to fracture stays the same for martensite content greater than 30 percent).

Impurity grain boundary segregation also has a significant effect with liquid metal embrittlement. According to Friehe (25), surface coatings like hot dip galvanizing steels can bring on a form of liquid metal stress corrosion cracking. Pickens, Precht, and Westwood (26) emphasize that a powder metallurgy aluminum alloy has greater resistance to Hg - 1.5% Ga than an ignot mold aluminum alloy due to a partial grain boundary corrosion of $MgZn_2$ in the ingot mold aluminum alloy.

Another factor to consider in embrittlement susceptibility is grain size. A finer grain size may increase ductility and delay LME initiation (Kamdar (9)), but with respect to Davies's work (24) that may not optimize the best resistance to HE. The susceptibility of a metal to HE

and LME can differ, but a similarity develops when the embrittlers initiate a crack.

2. Initiation of a Crack

Krishtal's proposed mechanism (27) for LME has the embrittler atom diffusing into grain boundaries by tens of molecular diameters. Therefore, time is necessary for diffusion to occur which Gordon and An (28) refer to as the incubation period. Gordon and An (28) supported and extended Krishtal's proposed mechanism by investigating the embrittlement of 4140 steel by solid and liquid indium. They concluded that because of this incubation period, crack nucleation with embrittler grain boundary diffusion is controlling crack initiation. Thus, two separate stages in crack growth are controlled by two activation energies. The activation energies are for atoms diffusing from the adsorbed state and for atoms actually diffusing through grain boundaries. Gordan and An also illustrated that some embrittlement couples do indeed relate to a delay in crack initiation (see Table II). In contrast to the argument of diffusion controlled crack initiation, Westwood and Kamdar (29) have calculated closely the instantaneous initiation of cracks in a zinc-mercury system as a function of an overall crack initiation energy. The energy, Φ, to fracture the bonds across the fracture plane for zinc in liquid mercury is 1/2 that in the inert nitrogen environment.

Hydrogen embrittlement can also cause a type of delayed failure with hydrogen interacting in the plastic zone about a crack tip as a function of diffusion and adsorption. For example, Bernabi, Bombari, and Borruto (23) revealed the delayed HE failure of a 1 Cr - 1 Mn steel

will reach a maximum at a temper that produces the most grain boundary impurity segregation and temper embrittlement. Delayed failure must meet two criteria for the onset of hydrogen induced delayed plasticity and cracking. Chu, Li, Hsiao, and Ju (30) have shown in a 30 Cr2MoV steel as well as eight other steels that if $K_I > K_{ISCC}$ and if the strength of these steels exceeds a critical value then the plastic zone size was increased and the degree of plastic deformation increased continuously with time. According to Hsiao and Chu (31), hydrogen induced delayed plasticity and cracking in a 30 CrMnSiNi2 steel will enlarge the plastic zone ahead of a crack as a function of the reduced local shear strength. The critical local shear strength, γ^*, relates directly to the onset of the induced shear stress crack fracture toughness, K_{ISCC}. Charging with hydrogen lowers γ^* which lowers K_{ISCC}. Also, if the hydrogen exceeds the solid solubility limit in a hydride forming metal, a metal hydride, MH_x, will precipitate out. Charging or precipitation will both increase the lattice parameter and increase the embrittlement. Also according to Hsiao and Chu (31), surface cracking will also initiate after MH_x forms. Formation of MH_x locally imposes a tensile stress that aids martensite in transforming to α^1, and this results in surface cracking.

3. Propagation of Cracks

Under hydrostatic tensile stress, σ_H, van Leeuwan (32) proved hydrogen can induce cracking when the lattice chemical potential is reduced. With the assumption of a constrained yield stress, van Leeuwan modified the chemical potential equation of Li, Oriani, and Darken (33) by dropping the quadratic terms. The resulting equation of chemical

potential, μ , becomes a function of the hydrostatic stress, σ_H, and the partial molar volume of hydrogen, V_H

$$\mu = \mu_o - \sigma_H V_H \qquad 1.$$

Hsiao and Chu (26) presented the concentration of hydrogen, C, at a crack tip as another function of V_H and σ_H.

$$C = C_o \, e^{(\sigma_H V_H / R T)} \qquad 2.$$

The ability of the embrittler, H_2 or Hg, to stay and adsorb at the crack tip will assist the rate of crack nucleation, but is dependent on the embrittler being there. As a gas, hydrogen transports easily and quickly to the crack tip, but some question remained if Hg is fast enough to keep up with a propagating crack. Gordon (34) showed bulk liquid flow is the means of embrittler transport for liquid metals. For equivalent crack depths of one to two mm, Gordon and An (28) deliver the time of crack propagation as less than 0.1 seconds. Kamdar (9) has noted that LME can occur on the order of ms^{-1}.

One method of crack propagation studied by Lynch (4) is dislocation ingress at crack tips which is helped by the adsorbed hydrogen and mercury atoms which coalesce cracks with voids ahead of the crack tip. It is debatable whether the resultant intergranular fracture is a result of localized slip of Beachem (35) and Stolof (36) or if it is entirely the lattice decohesion mechanism of Oriani (37). Both mechanisms may be valid, but, according to Liaw, Roth, Saxena, and Landes (38) neither explain why the rate of fracture propagation is independent of the amount of intergranular fracture observed. They (38) also report fatigue crack growth rates for a Mn-Cr austenitic steel comparable to the results of Irving and Kurzfield (39) on a 4340 steel. Briefly, the

combined information (38,39) on these steels have cracks growing twice as fast in H_2 than in air and 10 times as fast in Hg than in H_2.

4. Fracture of Nickel Alloys at O.S.U.

Recent studies conducted at Oklahoma State University under the advisement of Dr. C. E. Price for nickel alloys in wet H_2 and liquid mercury environments led to the present investigation of 4142 steel in mercury. The tensile fracture characteristics and fatigue behavior of nickel, Monel, Inconel, and Incoloy alloys investigated by Price and Good (40,41) show an interesting transition from intergranular to transgranular to microvoid coalescence across the cross section of the specimens. The higher the strain levels the more microvoids form at fracture. Some alloys (Nickel 200, Inconel 600, Incoloy 800, and Incoloy 825) that did not show intergranular fracture in slow strain rate tensile tests did show intergranular fracture in fatigue tests.

Price and Traylor (42) compared HE to LME for Nickel 200 at room temperature and found that nickel is embrittled similarly by hydrogen and mercury. Prior cold working reduced the amount of intergranular cracking under fatigue loading. Plastic deformation was necessary for crack initiation since the coldworked material was stronger than the unworked metal.

By varying grain size and strain rate, Price and Fredell (43) studied the comparative behavior of Monel 400 in hydrogen and mercury. An increase in grain size, with one exception at the coarsest (500 mm) grain size in mercury, resulted in increasing embrittlement in mercury. In mercury, loss of ductility was conspicuous leading to abrupt totally

intergranular fracture. As strain rate increased in the mercury environment, tensile strength rose from 398 to 653 MPa and reduction in area increased from 9 to 64 percent. Hydrogen environments produced less embrittlement. The tensile strengths started at 563 MPa and reduction in area started at 30 percent for the $1.6.10^{-6}s^{-1}$ strain rate. Price and Morris (44) reported similar tendencies for strain rate sensitivity for Inconel 600 and Incoloy 800.

CHAPTER III

EXPERIMENTAL PROCEDURE

1. Selection of Material and Sample Geometry

An initial investigation of 1045 carbon steel and 4142 chromium molybdenum steel in air and Hg confirmed embrittlement in both steels (Table III). 4142 steel did not require a vacuum anneal and had a controlled range of hardness from RC 25 to RC 45. For 4142 steel grain size was a constant 20 μm throughout these hardnesses. Martensitic 4142 steel therefore became the steel of choice for this experiment.

AISI 4142 contains approximately 0.42 C, 0.03 P_{max}, 0.04 S_{max}, 0.2 Si, 1.1 Cr and 0.2 Mo. Cold rolled round bar stock was machined as shown in Figure 6 into a symmetric smooth specimen. This specimen geometry was required to evaluate the initiation and propagation parts of crack growth in the tensile tests and was also used in some fatigue tests. The small diameter section was chosen to be 0.2 inches diameter by 1.3 inch long due to the threaded holders breaking before larger diameter specimens fractured.

2. Preparation and Testing on Samples

The specimen's test surface was mechanically polished using a final light grind with 600 grit alumina sandpaper on a lathe running at 5000 rpm. An additional chemical polish was performed by immersing the specimens in a solution of diluted 100g/l oxalic acid (25% acid to

water) for 20 minutes at room temperature (Tegart, 45).

Heat treatment consisted of: 1) austenize at 900 C for 10 minutes, 2) oil quench to room temperature, 3) temper at desired temperature for five minutes, 4) air cool three minutes, and 5) again oil quench to room temperature. By tempering at 338, 627, and 716 C, hardnesses of RC 45, 35 and 25 resulted, respectively. (See Figure 7)

Special threaded holders were made to hold the higher hardness steel specimens (Figure 8) on the MTS machine and improve the data at lower loads and displacements. This improvement resulted from the slight compressive stress used to set the threads which in turn prevented any slipping that regular friction grips would have. Accurate control of the initial specimen strain rate was then possible.

At 50% stroke control, strain rate was derived (see Appendix C) in terms of an equivalent initial length (see Appendix D). Strain rate was held at either 1.10^{-4} s^{-1} or 1.10^{-5} s^{-1} for a given sample.

The environment was controlled by running the tests at room temperature and then varying the environment from air to Hg to H_2 (wet) on a sample set of equivalently heat treated specimens. The Hg and wet H_2 environment chambers (Figure 9 and Figure 10, respectively) are made of clear plastic to enable the observer to note whatever might be of interest. H_2 was electrically generated by exposing the specimen's surface (see Appendix E) to 200 amp/m^2 in an electrolyte solution of dilute H_2SO_4 acid with .25 g/l $NaAsO_2$ at a pH = 3.2 (10). The H_2 samples were not precharged before stress/strain was applied.

3. Reduction of Data

Tensile engineering stress and strain data generated by the MTS

Stress-Strain program (Appendix F) are summarized in Table 4 and are listed according to their environment, strain rate and hardnesses. The values for hydrogen in parenthesis were extrapolated from the closest values to their respective hardness and strain rate in air. After the stress-strain values were calculated from the loads and displacements read from the MTS machine, the stress-strain values were graphed. For examples see Figures 11 through 16.

The graphs were then used to derive the yield strength, YS, and strain at yield, SAY, by using the o.2 percent offset method. The fracture strength, FS, and strain of fracture, SAF, were taken where the curves stop. The values of yield strain energy (SEY), fracture strain energy (SEF), and plastic work (MPW) were derived from the graphs by calculating the area under each curve which relates to a certain energy per unit volume. In the case of these graphs a unit area was taken to be 100ksi/1% strain = 1000 lb-in/in^3. The yield strain energy was equivalent to the area under the curve up to yield. The fracture strain energy then became the area under the whole curve while plastic work became the difference of SEF - SEY.

Time to failure, TTF, was calculated by using the initial strain rate, ISR, and total displacement at fracture, TDF.

TDF = Fracture Displacement - Zero Load Displacement

TTF = RATE 1 · TDF/3.

4. Evaluation of Data

In the tensile tests, the investigative procedure was a matter of recording loads and displacements to failure and then cogitating numbers

with a computer program (see Appendix F) to yield engineering stress versus strain diagrams. These stress versus strain diagrams were correlated with SEM and optical microscopy data.

The effect and severity of LME was then evaluated with respect to HE. The initiation of a crack was determined in each specimen as a result of some mechanism of microcrack initiation. Since H_2 can initiate a crack in steels, the crack propagation stage was more important in comparison between HE and LME. Therefore particular attention to intergranular fracture in wet H_2 and Hg helped in investigating the dominant mechanism of crack growth, in either environment.

In fatigue tests, the adsorption theory was put to the test by fracturing specimens cyclically fatigued at 70 to 90% of the ultimate strength. The fatigue and tensile tests were compared with Lynch's work (4) to buttress the favored decohesion theory and hint if other mechanisms are involved.

CHAPTER IV

RESULTS

1. Data from Tensile Tests

Figures 10 through 15 are stress-strain diagrams generated by the MTS strain program listed in Appendix D. Good agreement to values measured with an MTS strain gauge can be seen in Figures 13 and 15. In all the figures, 11 through 16 , some general features are standard.

The air samples reveal with their diagrams that a change in strain rate from 10^{-4} to $10^{-5}s^{-1}$ does not affect the curves at each general range of hardness. At approximately RC 45 the percent strain at failure is 6 to 7 percent while the lower hardness range at approximately RC 35 breaks around 7 percent strain. The hardness of air samples decreases when ductility (measured as percent strain at fracture) increases.

At the slow strain rate, $10^{-5}s^{-1}$, in the hardness range of RC 22, Figure 11 shows Hg and air curves virtually similar with ultimate strength, UTS, very close while ductility is 9 and 10 percent, respectively. A general trend for mercury is a decrease in ductility with an increase in hardness, but some differences with respect to air samples are evident. At the highest hardness range Hg samples fracture before UTS with the higher strain rate sample fracturing closer to UTS than the slow strain rate.

The hydrogen samples have both tensile strength and ductility diminishing as hardness increases. As strain rate increases the

fracture strain and fracture strength increase. (Note here, these samples are not precharged with H_2, therefore diffusion enhanced embrittlement may be happening and will be discussed in the next chapter A faster strain rate allows less time for diffusion, less embrittlement, therefore a greater strain and strength at fracture.) The hydrogen sample in Figure 14 shows a similar bend in the curve that may be an early yield like the early yield in Hg in Figure 12. All in all, hydrogen is far the more strain rate sensitive environment when compared to mercury. A graphic example showing typical curves of Hg, H_2, and air for different hardnesses at a fast strain rate, $10^{-4}s^{-1}$, illustrates in Figures 17 and 18 that there is a strain rate sensitivity for hydrogen not seen in air or mercury.

Another revealing graph is Figure 19 where strains at fracture for Hg, wet H_2, and air samples are plotted as a function of hardness. The slope for Hg samples is steeper than that for air or H_2. Extrapolating from this graph, the Hg samples behave similarly to air at low hardnesses while for the high hardnesses, Hg samples behave like the H_2 samples. Strain at yield, SAY, and strain at ultimate strength, SAT, are shown for air and Hg in Figures 20 and 21, respectively. SAY is not shown here to be strain rate sensitive in air but a significant event is seen in SAY for Hg as a function of strain rate. The higher strain rate Hg samples have higher SAY except at the lowest hardnesses, RC 25 or less. For Hg samples harder than RC 40, SAT is the strain at fracture.

A pertinent relation between strain rate and environment as a function of hardness is detailed in Figure 22. The slow strain rate Hg samples have yield strain energies averaging lower than the air values

while the fast strain rate Hg samples have data points averaging higher than the air values.

The total strain energy to fracture, SEF (derived from the entire area beneath the stress-strain curve), is a good measure for embrittlement, Figure 23. At the slow strain rate, as hardness increases from around RC 25 to 45, air samples taken approximately 25 to 195 times the energy to fracture than H_2 samples need to fracture, while Hg samples take 23 to 60 times the energy to fracture than H_2 samples. At the high strain rate of around RC 45 air samples take about 52 times more energy to fracture than H_2 samples while Hg samples merely take 13 times the energy to fracture. (Note here, a similarity is seen in Figure 19 with respect to Figure 23. Two mercury samples, one at the high strain rate and one at the low strain rate, have higher % strains and higher strain energies than the trends show. These anomalies are likely due to changes in the 4142 steel and/or the Hg with the possibility that mercury oxides and temper hot spots created these two points in Figures 19 and 23.)

Plastic work is taken as the difference of SEF - SEY = MPW and in Figure 24 the similarity to Figure 23 is obvious for air and Hg. (The 0.2 percent offset method for determining yield did not see yield in all but one sample of H_2 and therefore was not included in Figure 24.) About RC 40 where the changes in slope of SAY and SAT for Hg and air occur, the graph of plastic work in air also increases but the plastic work in Hg decreases. The macroscopic plastic work of air increases by a factor of 4.5 over the MPW of Hg as hardness increases from approximately RC 25 to 45. Another similarity is that the two points for Hg in Figures 19 and 23 also show up in Figure 24. A local soft spot in the

samples for these two points might explain why the high values of plastic work (MPW) decrease at about the same slope as the majority of Hg points.

2. Fractography of Tensile Air Samples

All fractures were observed under a stereoscopic zoom microscope and in the scanning electron microscope. An obvious difference in the appearance at higher hardness levels of specimens tested in air was the absence of secondary longitudinal surface cracks, Figures 25 to 27. The separations were completely by microvoid coalescence; a typical example is given in Figure 28. The microvoid fracture at a typical secondary crack is shown in Figure 29. The features of interest are the smooth not jagged edges to the longitudinal crack and the continued occurrence of microvoids.

3. Fractography of Tensile Mercury Samples

In Figures 30 through 32, the slow strain rate fractures illustrate the typical fractures in mercury of samples tempered to different hardnesses. Secondary cracking occurs in all instances. (Note here the striking difference of fracture as hardness increases. Major secondary cracks at the low hardness progress to a very flat horseshoe-shaped fracture at the higher hardness. Except in the lowest hardness samples, the cracks obviously originated at one location at the surface, with shear lips occurring on the opposite side.) A similarity to air fractures is that the secondary cracking is minimal at the highest hardness level. Figure 30 is at a slight angle to show the presence of other surface cracks. The reduction in area can be seen to be much greater in

Figure 30 than in Figures 31 and 32. Along with the fractures revealing definite origin zones, this indicates that cracking initiation in mercury is limited at all these hardness levels but that crack propagation by mercury is limited only in specimens whose hardness is < RC 30.

The fracture control mechanism corresponds to the fracture surface visible at low magnification. Fractures above RC 30 were intergranular initially, Figure 33. A transition to microvoid coalescence eventually occurred, Figure 34. Initially the intergranular zone was largely free of secondary cracks but later the majority of grains were cracked around their boundaries. The transition zone to microvoid coalescence was a region of extensive secondary cracking, Figure 34. The microvoids in mercury were like the well defined microvoids reported by Lynch (4). Figure 35 is a view of one of the major secondary cracks in Figure 32 where the flat microvoids give way to the final fracture shear slip. In contrast to the microvoids shown in the air specimen, Figure 29, the microvoids in mercury have jagged and abrupt secondary cracks. Intergranular cracks appear even when the primary crack is by microvoid coalescence.

At hardness levels below RC 30, the cracking was less intergranular in mercury than a form of transgranular shear without obvious crystallography, Figure 36. A multitude of secondary cracks are revealed at the sample's edge of Figure 36 but do not appear intergranular.

4. Fractography of Tensile Hydrogen Samples

A sequence of four low magnification views is shown in Figures 37

through 40 to contrast with the series of Hg and air shown previously. An extra view is included to illustrate the strain sensitivity by fractography of Figures 38 and 39. (Note here the greater reduction in area of Figure 39 for the higher strain rate as opposed to Figure 38 at the slower strain rate.) Despite the apparent brittleness of fractures, different zones are visible. Figure 41 is a magnified slightly tilted view of the bottom edge of Figure 40 and clearly shows the transition from bottom to top of an initial transgranular to intergranular to microvoid fracture. Secondary cracking is easily observed in the transition from intergranular to microvoids. Figure 40 is particularly interesting because it shows both a series of crack propagation ridges radiating from the origin and a number of primary secondary cracks lying transversely to the crack propagation direction and extending in an area over much of the sample width. Figures 42 through 45 detail the fracture. Figure 42 taken at the edge shows a transgranular fracture propagating from the interior of the sample which gives way to an intergranular fracture, Figure 43. Both the transgranular and intergranular facets appear at the edges which leads to the interesting supposition that the fracture started in a band or zone in the interior, propagated transgranularly to the edge, then transformed to intergranular fracture around the edge to final microvoids in the interior. Small shear ridges were seen around the circumference on some specimens. At one transition of intergranular fracture to microvoids, a secondary crack is visible in Figure 44 transverse to a tear ridge. Figures 42 and 43 are taken close to one of the whitish tear ridges and in Figure 45 an abrupt transition at a tear ridge of intergranular fracture to microvoids indicates that fracture finally proceeds by microvoid coales-

cence to the center of the sample. In contrast to the high hardness sample in Figure 40, Figure 39 was taken at the same strain rate but at RC 33 and shows less secondary cracking in the transition of microvoids and the partially intergranular transgranular fracture, Figure 46. Figure 47 shows microvoids which are at the center of Figure 39 that are less flat and more sharply featured than those found in the center of the higher hardness sample.

5. Fractography of Fatigue Samples

Fatigue testing of smooth tensile specimens provides a means of studying crack initiation at lower stress levels than occur in tensile tests. In this instance specimens of around RC 35 were tested at stress levels of approximately 70 and 90 percent of the tensile strength in the appropriate environment. The lives in all cases were brief, Table V. A fracture in air is seen in Figure 48 with an origin zone detailed in Figure 49. The fracture in air is transgranular and superficially resembles the transgranular fracture found in the tensile hydrogen sample, Figure 42. A late fatigue zone, illustrated in Figure 50 has many small secondary cracks. The fracture in Hg is shown in Figure 51 with details of an origin zone and a late fatigue zone in Figures 52 and 53. The fracture is intergranular initially and largely intergranular subsequently. The fracture in hydrogen, Figure 54, was mainly transgranular with occasional intergranular zones, Figure 55.

CHAPTER V

DISCUSSION

1. Comparison to Selected Research

This investigation of 4142 steel complements the recent work Lynch (4) conducted on D6ac steel. The experimental approaches on 4142 steel and D6ac steel will be discussed first and the results of these slightly differing approaches will then be considered. A comparison to other research will follow.

The grain size in both steels was around 20 μm and the alloy composition of the steels differed only in the molybdenum and vanadium content. Hardness values in this 4142 steel varied from 20 to 48 RC while those in Lynch's (4) D6ac steel varied from 35 to 58 RC. Lynch therefore avoided conditions where embrittlement could be minimal and did not explain whether the limiting hardness was similar in air and mercury. The phosphorous and sulfur impurities in 4142 were most likely higher than those found in D6ac, but neither steel showed temper embrittlement in the fractography. According to Lynch, dislocation egress with strong oxygen bonds at crack tips was not evident since no preference for prior austenite grain boundaries, where impurities would segregate, was revealed in his fractography. In short, intercrystalline fracture surfaces did not dominate in the air environment. Fractography of 4142 steel also reflects this as well the stress-strain graphs

supporting the expected ductilities in air.

The slight difference in alloy content of these steels is less distinct than the geometry and loading of these steels. Lynch sets his notched three point bend specimens to reveal plane strain growth of cracks to final fracture. The smaller diameter smooth tensile specimens of this investigation revealed initiation as well as propagation to the final microvoid stage of fracture. The fact that Lynch maintained crack growth in a mostly plane strain stress regime may be a clue to the unusual similarity in fractography of comparable D6ac samples in Hg and H_2 environments. The differences found in the 4142 study in the 4142 study include surface initiation in Hg where H_2 initiated cracks subsurface-wise in the plane stress regime. Some closeness in fractography also exists in the 4142 fractographs for a given sample condition. The parallel fractographies in both steels of HE and LME showed up under the scanning electron microscope (SEM) but Lynch used the transmitting electron microscope (TEM) to further amplify his fractography.

Because of the remarkable similarity of fracture for a given specimen condition in Hg and H_2, Lynch proposes that HE is largely due to adsorption of hydrogen at the crack tip. Earlier studies by Kamdar (9) and Stoloff (14) generally support LME is by adsorption induced reduction in cohesion. With the aid of TEM fractography, Lynch makes a strong argument with previously unseen dimples that hydrogen also reduces cohesion at the crack tip by adsorption of embrittler hydrogen.

Since adsorption influences the crack tip interatomic bonds, Lynch postulated that the embrittler aids dislocation ingress to counter normal dislocation egress. This in turn would reduce the plastic zone size at the crack tip, and thereby lower the energy necessary to

propagate a crack. Lynch's evidence of crack ingress by TEM revealed shallow microdimples along quasicleavage fracture facets. These microdimples are the probable remains of the reduced void sizes associated with the decreased plastic zone size. Extensive dimpling is not revealed on the SEM fractographs of 4142 steel but secondary microcracking aggravated by tempering (see Figures 56 and 57) is evident on all 4142 samples. Secondary microcracking often is seen at abrupt changes or transition from intergranular fracture to microvoids and this secondary microcracking might explain some of the differences in fractography for 4142 steel in H_2 and Hg. This will be discussed further on in this report, but first to consider the test results of our respective reports.

Adsorption discussed by Lynch (4) on D6ac steel helps the crack propagate because of preferential adsorption at boundary/surface intersections, because of voids forming more easily along grain boundaries, and because embrittlers have greater affinity to impurity grain boundary segregation. He noted in his discussion that D6ac steel definitely sees a 2% segregation of phosphorous and an enrichment of chromium and molybdenum to prior austenite grain boundaries. Tempering probably aids LME and HE slightly by making intercrystalline fracture more probable with the process of grain boundary segregation; however, temper embrittlement is unlikely since no evidence in air revealed fracture along prior austenite grain boundaries. Both investigations of D6ac and 4142 steel revealed differences in the fractography between air and the embrittling environment on comparable samples. The dimples in air for D6ac steel were feathery and less well defined than those found in Hg and H_2. This report found rounded microvoids in air for 4142 steel

while jagged microvoids were revealed in the H_2 and Hg environments. The microvoids found with the aid of the SEM do not reveal as much as the dimples found with the TEM since localized plastic flow along with decohesion might have been at work to allow local slip in the [112] direction from the quasicleavage plane {100}. Therefore, Lynch observed that adsorption may dominate crack growth in D6ac steel. In contrast, some fractographic evidence in 4142 steel indicated areas where secondary cracking probably effected fracture initiation micromechanisms.

Secondary cracking did distort the fractography somewhat in 4142 steel. Initiation of a crack in mercury looked transgranular where extensive surface cracking was even though fatigue and tensile tests in mercury revealed the majority of fractures initiated intergranularly. Since the solubility of this steel with Hg is practically nil as evidenced by the difficulty in wetting the smooth steel surfaces, a certain strain energy probably had to be achieved before adsorption of Hg brought on LME. Lynch noted this for D6ac also.

Initiation of a crack in hydrogen for 4142 appeared transgranular in a fatigue test but in tensile tests, although surface zones were transgranular, the fracture appeared to initiate in the intergranular zone within the sample interiors. The secondary cracks most likely transported enough hydrogen during hydrogen charging to be unable to tell if adsorption or diffusion dominates initiation. Without secondary cracking to complicate fracture, Lynch observed that this effect in D6ac steel of dissolved hydrogen was probably not significant. Nucleation of voids was most likely aided by dislocation activity in transporting hydrogen. In any case, he noted voids and cracks would probably be promoted by adsorption of hydrogen if a significant enough amount of

hydrogen were available within internal cracks and voids.

A question therefore arose for the 4142 steel with respect to adsorption by hydrogen. The $10^{-5}s^{-1}$ strain rate hydrogen samples had lower strengths and less ductility than the $10^{-4}s^{-1}$ samples. If the adsorption induced reduction in cohesion is controlled by the kinetics of the adsorption process (6), should strain rate have had such a significant effect on the hydrogen samples? Ductility as measured as strain at fracture and ultimate tensile strength were both half the values at the slow $10^{-5}s^{-1}$ as they are at $10^{-4}s^{-1}$. The time it took to fracture these comparable samples was only 4 to 6 times longer at $10^{-5}s^{-1}$ than at $10^{-4}s^{-1}$ which is again approximately half the time expected since $10^{-5}s^{-1}$ is 10 times slower than $10^{-4}s^{-1}$. Lynch (4) has shown that diffusion of hydrogen is on the order of one μms^{-1} and since these 4142 samples are not precharged, diffusion may have something to do with these differences. The 4142 samples in H_2 break on the order of a few minutes.

Some micromechanism is probably responsible for increasing the effects seen on the stress-strain generated data listed in Table IV. Since adsorption of hydrogen is a constant at constant room temperature, something might be magnifying the effect hydrogen is having at the crack tip. Void nucleation with extreme internal void pressures augmenting HE might have done the trick but SEM fractographic evidence showed little in the way of increased intergranular fracture as a function of strain rate. The secondary microcracking probably aided diffusion enhanced adsorption but to determine this requires a TEM and is beyond the scope of this investigation. But, beyond the diffusion enhanced adsorption is the practical effect charging has on steels. Lee, Goldenberg, and Hirth

(46) show results on a 4340 steel that indicate precharged specimens have internal crack nucleation while dynamic charged specimens go to a Mode 1 type fracture when the surface reached yield. Similar internal crack nucleation and quasicleavage fracture is seen on the SEM for 4142 steel, Figures 42 and 43.

Another question occurred during the investigation of 4142 steel with respect to Lynch's work. If adsorption is the dominant microcracking mechanism in H_2 and Hg for D6ac steel, why was there such a difference in the comparable stress-strain graphs of H_2 and Hg for 4142 steel? The slow strain rate samples in Hg with respect to the fast strain rate samples in Hg, actually had the strain at fracture increase around RC 45, decrease around RC 35 and then increase again around RC 25. The UTS also showed a slight increase around RC 45, a decrease around RC 35 and slight decrease around RC 25. The comparable H_2 samples consistently were 50% less ductile at slow strain rates while the trend for comparable Hg samples showed a dip around the medium hardness. A difference in the trend of embrittlement and its magnitude for H_2 and Hg exists, but what that difference means is hard to say. The stress strain graphs do give a clue for one basic difference in the comparable Hg and H_2 samples.

The Hg samples of 4142 steel exceed yield in every sample while the hydrogen samples don't. Therefore activation of HE does not require much, if any, plastic deformation as LME does require. Lynch (4) does not indicate what amount of plastic deformation is necessary, but Lee, Goldenberg, and Hirth (46) show that an AISI 4340 steel has plastic strain reduced to essentially zero during dynamic H_2 charging. 4142 steel is dynamically charged, therefore macroscopic plastic deformation

may have been unnecessary since local yielding could occur with favorably oriented grains. Whether this means another micromechanism was at work in HE or if adsorption was enhanced by secondary microcracking could not be determined. What can be said is the micromechanism of fracture of HE and LME has some basic similarities probably largely due to adsorption induced reduction in cohesion of atomic bonds at an advancing crack tip, with the note that microstructure and strain rate are probable important elements in the functioning of adsorption activities.

The fracture surfaces of the 4142 samples in H_2 or Hg do clue one feature of grain boundary segregation that is important in understanding a basic difference of HE and LME of 4142 steel. Intergranular fractures in 4142 steels are dominant in the crack nucleation stage of Hg samples but H_2 samples have a mixture of intergranular and transgranular features. This is not entirely unexpected. For a five percent Ni steel, Takeda and McMahon, Jr. (47) suggest that for samples in gaseous hydrogen, intergranular fracture indicated a plane stress regime where segregated metalloid impurities resulted in a concurrent reduction in cohesive energies while quasicleavage fracture indicated a plane strain regime related to dislocation motion and hydrogen transport to allow glide plane decohesion. An interesting comparison developed in the Hg and H_2 samples in 4142 steel. The plane strain criteria of Hertzberg (48, p. 283) were used to calculate whether stress or strain controlled the fractures in air, Hg, and H_2 for this 4142 steel. Using the fracture toughness values listed in Table VI and the yield strength values in Table IV, the results indicated that the only valid plane strain tests were done in the hydrogen environments for higher hardness

samples. Hg tests were plane stress and Hg initiated intergranularly, while H_2 tests were plane strain with internal crack nucleation. Therefore, the difference in stress-strain regime, as well as the similarities in crack initiation by plastic deformation, relate to the environment affecting the size of the plastic zone at an advancing crack tip.

2. Uses and Limitations of MTS Program

The assumption of equivalent initial length does not include the non-linear portion of the elasto-plastic behavior of materials, especially the nonferrous metals. Accuracy cannot be assured for nonwork hardening materials since the transformation to plasticity with increasing tensile stress is calculated in the constant cross sections under an effective smallest diameter. To keep accuracy, a nonlinear second order equation using aspects of finite elements can base the transformation in a finite mesh, but the computer this program is used on is a Texas Instrument CC-40 and limits the number of points the 8-bit processor can compute in a reasonable amount of time. Fortunately, an order increase in accuracy can be had by doubling the number of points input as load and displacement. Unfortunately, the points have to be input by hand.

Advantages of this program are the flexibility in choosing the modulis of elasticity with a choice of the best incremental modulis or best average in the linear range and being able to input the modulis of choice. The measurements are easy to read and input but are tedious to do. The zero load displacement is calculated from the input data to start all graphs at nominal stress and strain of zero. Precise relative

stress-strain curves are generated and conformity and accuracy are within 5 to 10% at final fracture and 1 to 5% of ultimate tensile stress.

With the generation of stress-strain graphs, many metallurgical factors can be estimated with better than ballpark accuracy. The strain energies calculated for Table IV give a clue to the relative embrittlements of hydrogen and mercury but comparable figures are scarce in the literature. Therefore it was hard to determine how close to real world values these were beyond the comparative strain gauge values. An estimate of fracture toughness derived in Appendix G and listed in Table VI gave reasonable values of fracture toughness and compared well with the plane strain fracture toughness from the Metals Handbook (49, p. 426) for the higher hardness in a similar 4340 steel in air. Estimated values here are within 20% of real world values and probably reflect the difference of smooth tensile specimens of small diameter which carry the stress-strain relations into the plane stress regime from plane strain initiation.

The disadvantages are primarily the finite number of points that can be input and the use of the program requires at least a working knowledge of the material to be studied. Also, the program must be modified somewhat if variable geometry specimens are to be used. Nevertheless, the data generated will amplify and reveal trends that otherwise could not be known with a visual record.

CHAPTER VI

CONCLUSIONS

The research and study of samples in mercury and wet hydrogen charged environments revealed fracture and stress-strain characteristics that were similar in nature, yet also different. In summary, the major findings of this report on hydrogen and liquid mercury embrittlement are:

1. Adsorption induced reduction in cohesion is the major micromechanism of fracture in liquid mercury and wet hydrogen charged environments for quenched and tempered martensitic 4142 steel. The intergranular fracture associated with the adsorption mechanism occurs largely throughout the initiation and propagation phase for mercury, and occurs throughout the propagation stage in hydrogen.

2. Initiation of a crack in Hg requires some surface yielding whereas initiation of a crack in H_2 requires only local plastic deformation. The stress-strain curves for Hg samples show them breaking after yield while the fractures were initiated intergranularly from one surface origin. Hydrogen samples broke before yield and had cracks originate from a transgranular internal zone.

3. Mercury embrittlement is not strain rate sensitive at the strain rates of $10^{-5}s^{-1}$ and $10^{-4}s^{-1}$, but hydrogen embrittlement is. The fractures and stress-strain graphs for mercury samples of comparable hardness but different strain rate have shown close likenesses to each

other. However, the graphs for hydrogen show a decrease in embrittlement for the higher strain rate due in part to diffusion. These hydrogen samples are not precharged, therefore hydrogen diffusion, which is one μms^{-1}, logically will affect samples which break in five minutes. The extensive secondary cracking aids hydrogen transport to grain boundaries which are subsequently embrittled with hydrogen adsorbing onto then diffusing into the grain boundaries.

SELECTED BIBLIOGRAPHY

1. Lynch, S. P. Scripta Metall, Vol. 13, p. 1051 (1979).

2. Lynch, S. P. Hydrogen in Metals, I. M. Bernstein and A. W. Thompson, eds., AIME: Warrendale, Pennsylvania, pp. 863-871 (1981).

3. Lynch, S. P. Acta Metall, Vol. 29, pp. 325-340 (1981).

4. Lynch, S. P., Acta Metall, Vol. 32, No. 1, pp. 79-90 (1984).

5. Hirth, J. P., Met. Trans. A, Vol. 11A, pp. 861-890 (1980).

6. Petch, N. J., and Stables, P. Nature, 169, 842 (1952).

7. Vehoff, H., and Rothe, W. Acta Metall, Vol. 31, No. 11, pp. 1781-1793 (1983).

8. Ransome, C. M., and Ficalora, P. J. Met. Trans. A, Vol. 11A, pp. 801-807 (1980).

9. Kamdar, M. H. Embrittlement by Liquid Metals, Pergamon Press: Oxford, Prog. Mater. Sci., Vol. 15, Part 4, pp. 289-371. (1973).

10. Stoloff, N. S.; Ashok, S.; Glicksman, M. E.; and Slavin, T. Scripta Met, Vol. 15, p. 331 (1981).

11. Hancock, G. G., and Johnson, H. H. Trans. TMS-AIME, Vol. 236, pp. 513-516 (1965).

12. Rostoker, W.; McAughey, J. M.; and Markus, H. Embrittlement by Liquid Metals, Reinhold Publishing Corporation: New York, New York (1960).

13. Stoloff, N. S. Environment-Sensitive Fracture of Engineering Materials, Z. A. Foroulis, ed., AIME: Warrendale, Pennsylvania, pp. 486-518 (1979).

14. Stoloff, N. S. Liquid and Solid Metal Embrittlement, Plenum Press: New York, Atomistics of Fracture, Vol. 5, pp. 921-953 (1983).

15. Nicholas, M. G., and Old, C. F. "Review of Liquid Metal Embrittlement." J. Mater. Sci., Vol. 14, No. 1, pp. 1-18 (1979).

16. Shunk, F. A., and Warke, W. F. Scripta Met, Vol. 8, 519 (1974).

17. Lynch, S. P. ARL Mat. Reports, No. 101, 102, Dept. of Defense: Melbourne, Victoria, Australia (1977).

18. Kelly, A.; Tyson, W. R.; and Cottrell, A. H. Phil. Mag., Vol. 15, p. 567 (1967).

19. Gilman, J. J. Plasticity, Pergamon Press: Oxford, p. 43 (1960).

20. Miller, E. C. Liquid Metals Handbook, 2nd Edition, p. 144, Government Printing Office, Washington, D. C. (1952).

21. Westwood, A. R. C.; Preece, C. M; and Kamdar, M. H. Fracture, Vol. 3, p. 589, H. Leibowitz, ed., Academic Press: New York (1971).

22. Tsutsui, M.; Yamada, T.; Otsuka, R. Nagoya - Shi Kogyo Kenkyusho Kenkyu Hokoku, Vol. 66, pp. 1-4, Japan (1983).

23. Bernabi, V.; Bombari, G.; and Borruto, A. Met. Technol, London (1983).

24. Davies, R. G. Scr. Metall, Vol. 17(7), pp. 889-892.

25. Friehe, W. Worstoffe and Korrosion, Vol. 29, pp. 747-753 (1978).

26. Pickens, J. R.; Precht, W.; and Westwood, A. R. C. J. Mater. Sci., Vol. 18(6), pp. 1872-1880 (1983).

27. Krishtal, M. A. Sov. Phys. Dokl, Vol. 15(6), pp. 614-617 (1970).

28. Gordon, P., and An, H. H. Met. Trans. A, Vol. 13A, pp. 457-472 (March, 1982).

29. Kamdar, M. H., and Westwood, A. R. C. Acta Met., Vol. 16, p. 1335 (1968).

30. Chu, Wu-Yang; Li, Shi-Qun; Hsiao, Chi-mei; and Ju, Shur-Yahn. Corrosion-NACE, Vol. 37, No. 9, p. 514, (September, 1981).

31. Hsiao, Chi-mei, and Chu, Wu-yang. "Some New Aspects of Hydrogen Damage." Beijing University of Iron and Steel Technology: Beijing (1981).

32. van Leeuwen, H. P. An Analysis of Hydrogen Induced Cracking, National Aerospace Laboratory "NLR": Amsterdam, The Netherlands (1975 to Present).

33. Li, J. C. M.; Oriani, R. A.; and Darken, L. S. Z. Phys. Chem. N.F., Vol. 49, p. 271 (1969).

34. Gordon, P. Metall. Trans, p. 437 (1972).

35. Beachem, C. D. Metall. Trans, p. 437 (1972).

36. Stoloff, N. S. Environment Sensitive Fracture of Engineering Materials, Z. A. Foroulis, ed., p. 486, Metall. Soc. AIME: Warrendale, Pennsylvania (1979).

37. Oriani, R. A. Fundamental Aspects of Stress Corrosion Cracking, p. 32, NACE: Houston (1969).

38. Liaw, P. K.; Roth, L.; Saxena, A.; Landes, J. D.; Leax, T. R.; and Kilpatrick, N. L. Scripta Metall, Vol. 17, pp. 611-614 (1983).

39. Irving, P. E., and Kurzfield, A. Met. Sci., Vol. 12, p. 495 (1978).

40. Price, C. E., and Good, J. K. "The Fatigue Behavior of Nickel, Monel, and Selected Superalloys, Tested in Liquid Mercury and Air, A Comparison." ASME Journal of Engineering Materials and Tech., Vol. 106, p. 178 (April, 1984).

41. Price, C. E., and Good, J. K. "The Tensile Fracture Characteristics of Nickel, Monel, and Selected Superalloys Broken in Liquid Mercury." ASME J. of Eng. Mat. and Tech., Vol. 106 (April, 1984).

42. Traylor, Leland Bruce. M.S. Thesis, "A Comparison of Hydrogen and Mercury Embrittlement of Nickel Base Alloys." Dr. C. E. Price, Advising, Oklahoma State University, Stillwater, Oklahoma (1983).

43. Fredell, Robert Stephen. M.S. Thesis, "A Detailed Comparison of Hydrogen and Mercury Embrittlement in Monel 400." Dr. C. E. Price, Advising, Oklahoma State University, Stillwater, Oklahoma (1983).

44. Morris, James Arthur. M.S. Thesis, "Hydrogen and Mercury Embrittlement of Selected Nickel Based Alloys." Dr. C. E. Price, Advising, Oklahoma State University, Stillwater, Oklahoma (1984).

45. Tegart, W. J. M. The Electrolytic and Chemical Polishing of Metals, 2nd Edition, p. 101, Pergamon Press: New York (1959).

46. Lee, T. D.; Goldenberg, T.; and Hirth, J. P. Metallurgical Transactions A, Vol. 10A, pp. 439-448 (April, 1979).

47. Takeda, Y., and McMahon, C. J. Jr. Metallurgical Transactions A, Vol. 12A, pp. 1255-1266 (July, 1981).

48. Hertzberg, R. W. Deformation and Fracture Mechanics of Engineering Materials, John Wiley and Sons: New York (1976).

49. Metals Handbook, 9th Edition, Vol. 1, "Properties and Selections: Irons and Steels," A.S. of M.: Metals Park, Ohio (1978).

50. Physics of the Atom, 3rd Edition, R. M. Wehr, J. A. Richards, Jr., and T. W. Adair III, eds., Addison-Wesley Publishing Company: Reading, Massachusetts, pp. 496-498 (1978).

51. Flinn, R. A., and Trojan, P. K. Engineering Materials and Their Applications. Houghton and Mifflin Company: Boston, Massachusetts, pp. 26, 27, 42 (1975).

52. Bryukhanova, L. S.; Andreeva, I. A.; and Likhtman, V. I. Sov. Phy - Solid State, Vol. 3, pp. 2025-2028 (1962).

53. Nichols, H., and Rostoker, W. Trans. ASM, Vol. 58, pp. 155-163 (1965).

54. Iwata, Y.; Asayama, Y.; and Sakamoto, A. Nippon Kinzaku Gakkaishi (J. Japan Inst. Met.), Vol. 31, pp. 77-83 (1967).

55. Rinnovatore, J. V.; Corrie, J. D.; and Markus, H. Trans. ASM, Vol. 59, pp. 665-671 (1966).

56. Preece, C. M., and Westwood, A. R. C. Fracture, Proc. Sec. Intl. Conf. on Fracture, P. L. Pratt, ed., pp. 439-450, Chapman and Hall: London, England (1969).

57. Zych, J. M.S. Thesis. Illinois Institute of Technology: Chicago, Illinois (1977).

APPENDIX A

FIGURES

Figure 1. Illustration of change in lattice parameter at the crack tip in the presence of a tensile stress shows decrease in the strength of metallic atomic bonds between 1 and 2 by adsorbed E which increases the lattice parameter by sharing more electrons with an extra atom

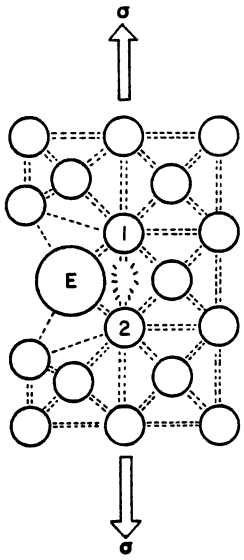

Figure 1.

Figure 2. Intergranular fracture assisted by 1) adsorbed embrittler attacking grain boundary segregation impurities and 2) initiated by Krishtal's diffusion of embrittler ten diameters into grain boundaries to delay plastic flow

Figure 3. Brittle transgranular fracture of embrittler aided trans-crystalline slip up to 2 to 3 diameters deep into grain surfaces

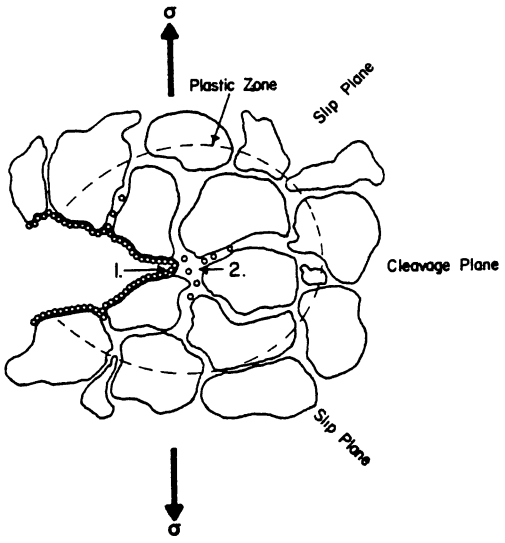

Figure 2.

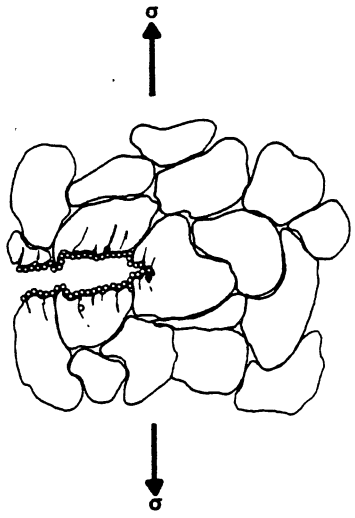

Figure 3.

Figure 4. Hydrogen embrittlement assisted 1) by crack initiation from formation of MHx, 2) by reduction in cohesion strength at propagating crack tip, and 3) by creation of hydrogen cloud in presence of a stress gradient which in conjunction with natural diffusion helps to nucleate voids ahead of cracks

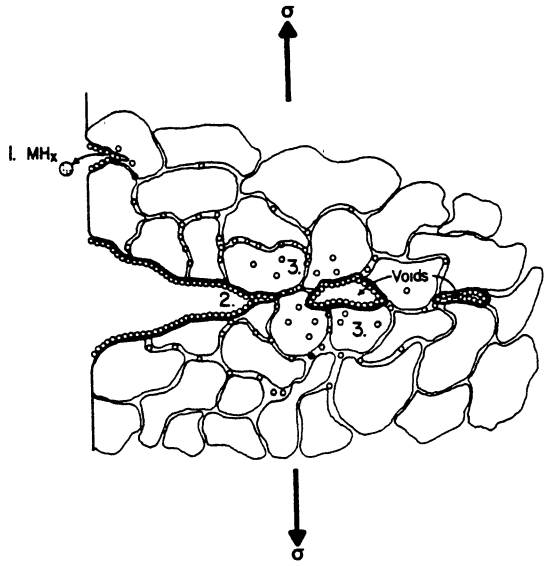

Figure 4.

Figure 5. Special summary of chemical resistance of metals and alloys to liquid metals at 300, 600, and 800 C

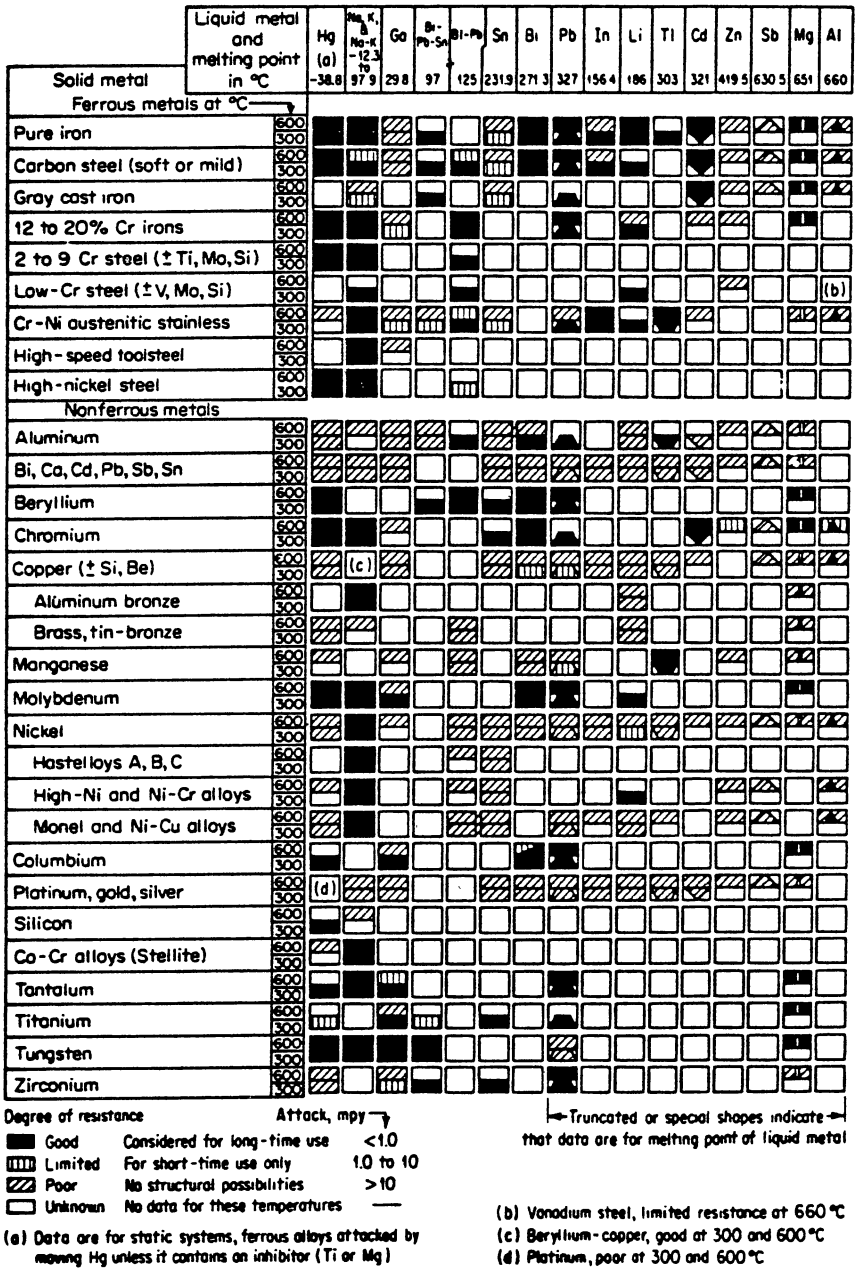

Source:

Miller, E.C., Liquid Metals Handbook, 2nd Edition, p.144, Government Printing Office, Washington, D.C. (1952)

Figure 5.

Figure 6. Geometry of the threaded cylindrical smooth tensile specimen with experimental dimensions

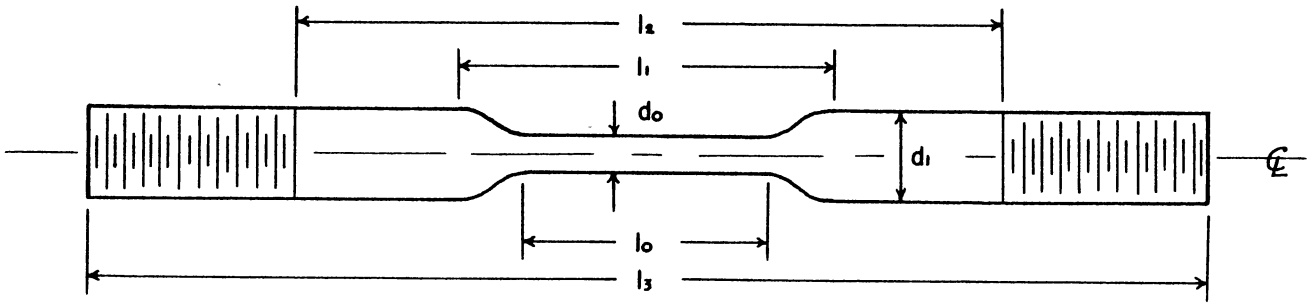

Small Diameter	$d_o = .200"$
Large Diameter	$d_1 = .490"$
Small Diameter Section Length	$l_o = 1.300"$
Total Machined Length	$l_1 = 2.000"$
Grip to Grip Length	$l_2 = 3.800"$
Overall Length	$l_3 = 6.000"$
Thread Size	½ by 20/in.

Figure 6.

Figure 7. Plot of tempering temperature vs hardness for the smooth tensile specimen of 4142 steel where tempering temperature is the temperature a specimen is held at for five minutes during the heat treatment (of austenitizing at 900 C for ten minutes, at temper temperature, air cool for 3 minutes, and final oil quench to room temperature

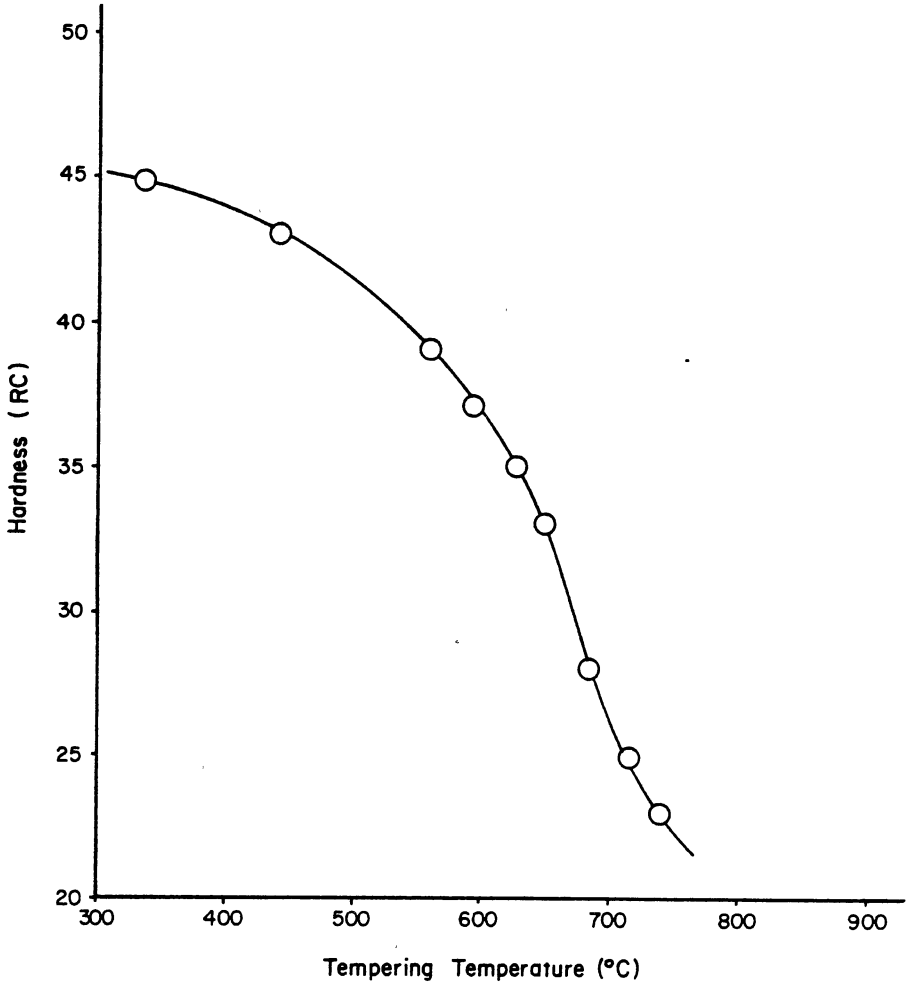
50
45
40
35
30
25
20
Hardness (RC)
300
400
500
600
700
800
900
Tempering Temperature (°C)

Figure 7.

Figure 8. **Diagram of special threaded holders in regular MTS threaded grips to hold the threaded tensile specimens**

1) MTS threaded holders
2) Connection to load cell or hydraulic device
3) Hex screws, 4
4) Adapter, 1/2 by 20 threads
5) Set plug
6) Threaded sample

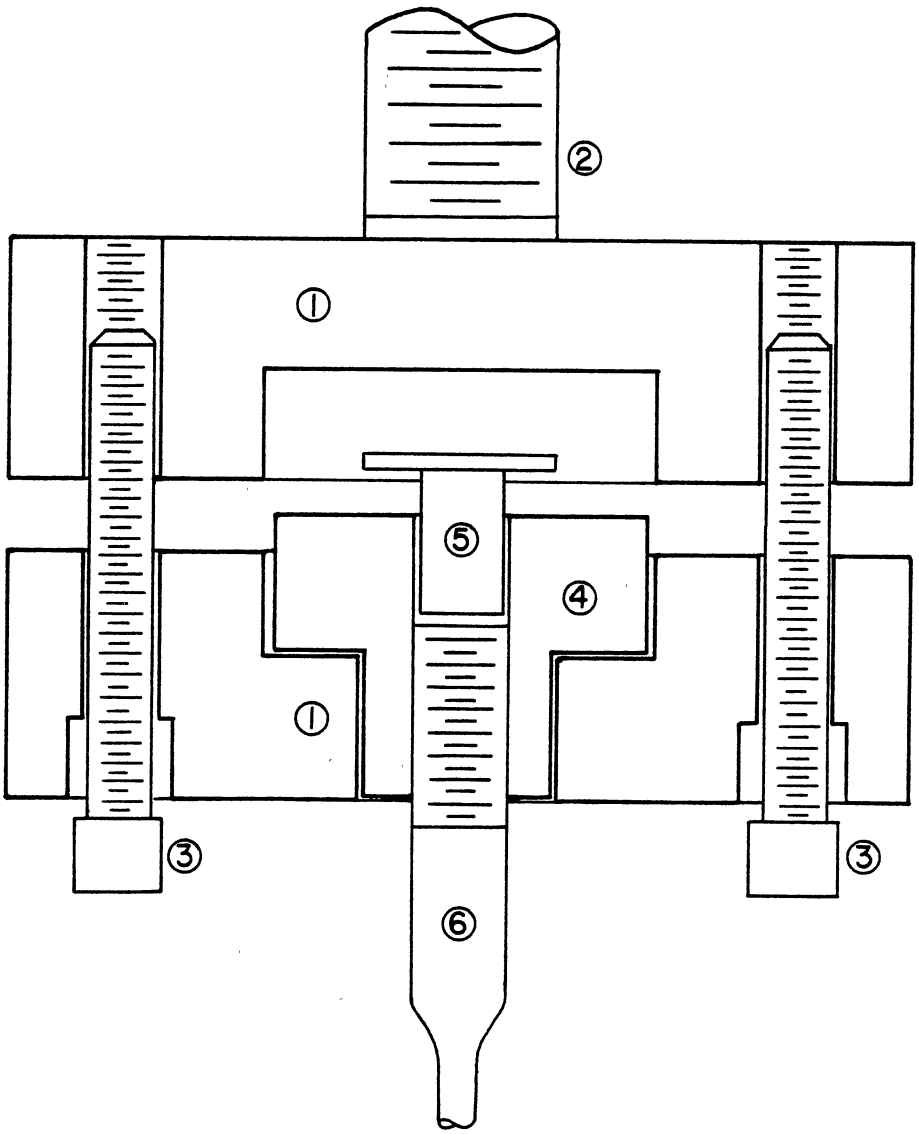

Figure 8.

Figure 9. **Mercury environmental chamber of clear plastic with teflon tape seals**

1) Plastic Hg environment chamber
2) Hex screws, 4
3) Hg fill plug
4) Teflon tape
5) Test sample

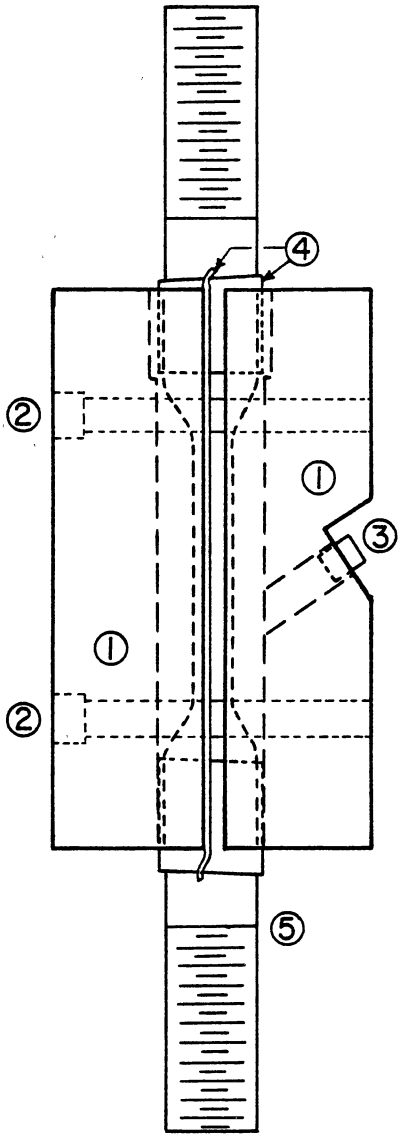

Figure 9.

Figure 10. **Hydrogen environmental chamber showing platinum electrodes with wax seal**

1) H_2 environment chamber
2) Platinum cathode junction
3) Hex screws, 4
4) Plastic lid
5) Wax sealant
6) Electrician's tape

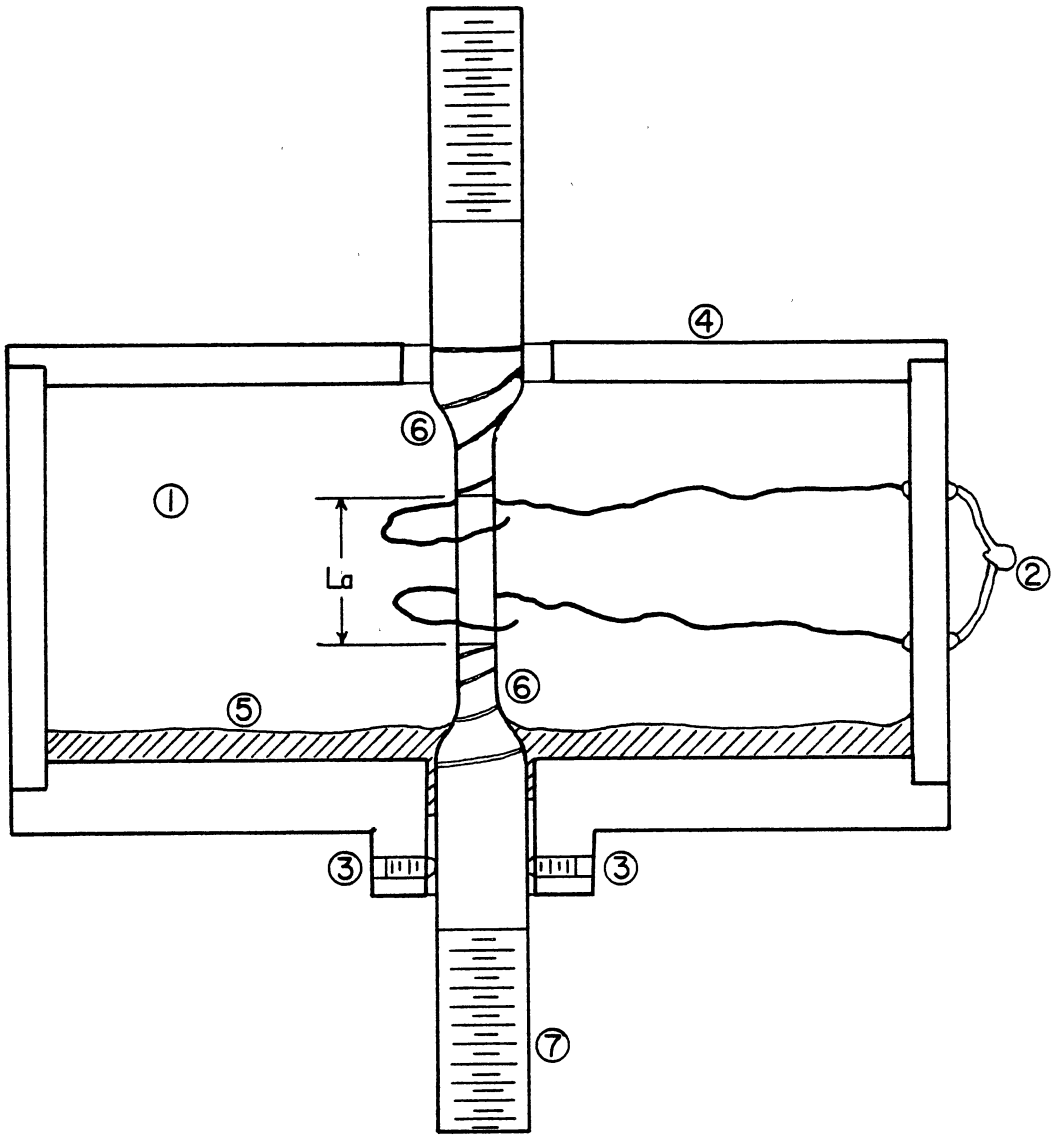

Figure 10.

Figure 11. Tensile stress-strain diagram comparing wet H_2, Hg, and air samples at 24 C with hardness RC 22 at an initial strain rate of $1 \cdot 10^{-5} s^{-1}$

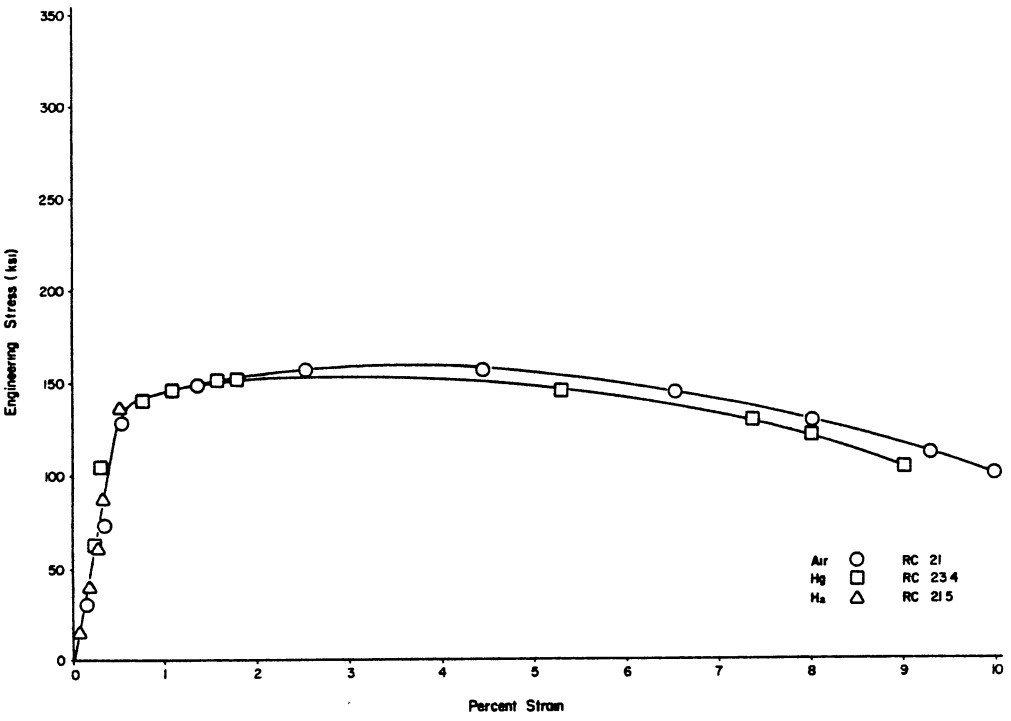
Engineering Stress (ksi)
350
300
250
200
150
100
50
0
0
1
2
3
4
5
6
7
8
9
10
Percent Strain
Air
Hg
He
RC 21
RC 234
RC 215

Figure 11.

Figure 12. Tensile stress-strain diagram comparing wet H_2, Hg, and air samples at 24 C with hardness RC 35 at an inital strain rate of $1 \cdot 10^{-5} s^{-1}$

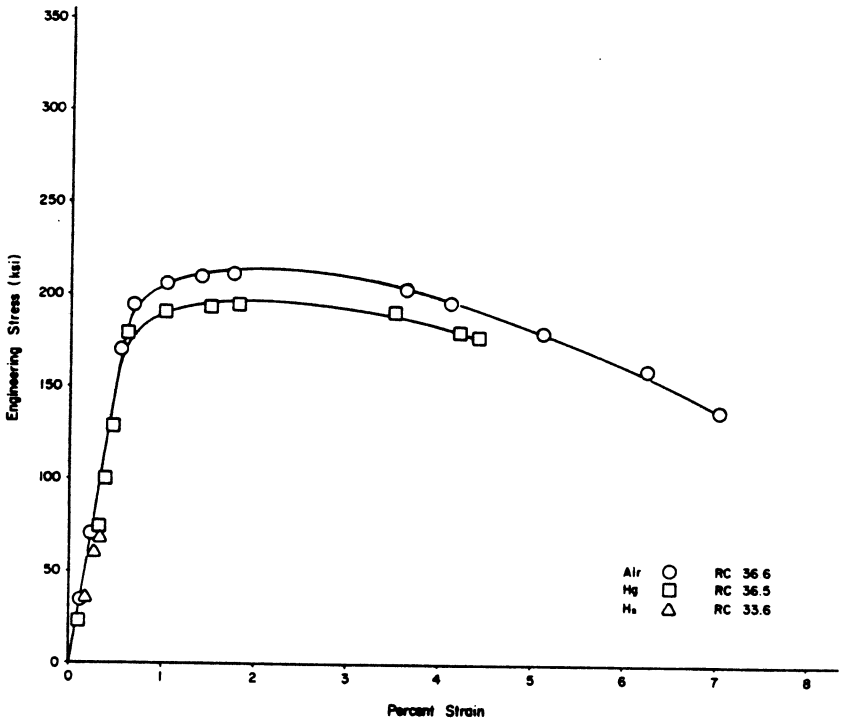
350
300
250
200
150
100
50
0
Engineering Stress (ksi)
0
1
2
3
4
5
6
7
8
Percent Strain
Air
Hg
RC 36.6
RC 36.5
RC 33.6

Figure 12.

Figure 13. Tensile stess-strain diagram comparing wet H_2, Hg, and air samples at 24 C with hardness RC 45 at an initial strain rate of $1 \cdot 10^{-5} s^{-1}$

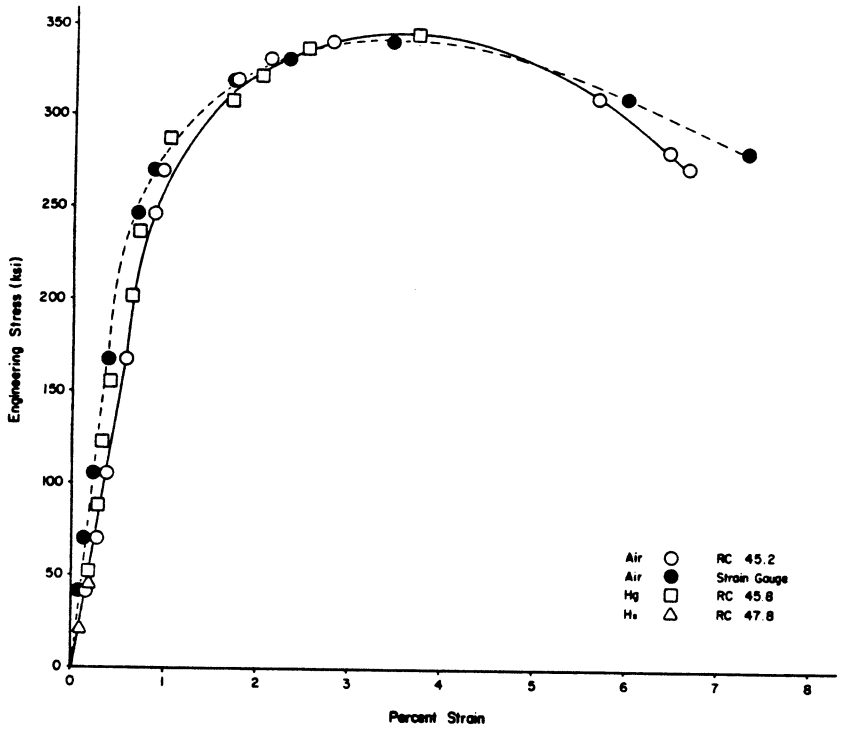
Engineering Stress (ksi)
350
300
250
200
150
100
50
0
0
1
2
3
4
5
6
7
8
Percent Strain
Air
RC 45.2
Air
Strain Gauge
Hg
RC 45.8
RC 47.8

Figure 13.

Figure 14. Tensile stress-strain diagram comparing wet H_2, Hg and air samples of 24 C with hardness RC 35 at an initial strain rate of $1 \cdot 10^{-4}\ s^{-1}$

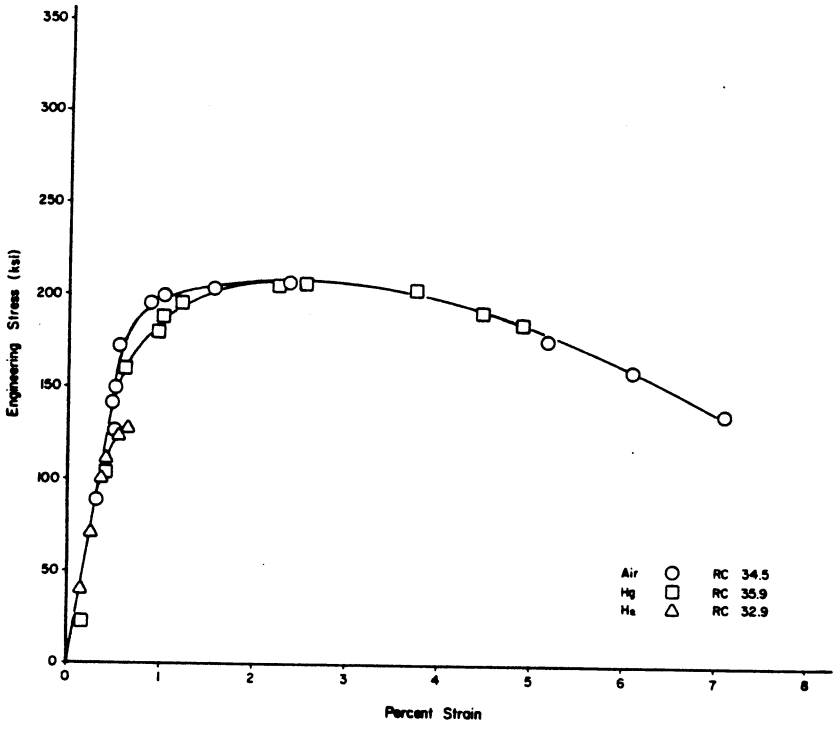
350
300
250
200
150
100
50
0
Engineering Stress (ksi)
0
1
2
3
4
5
6
7
8
Percent Strain
Air
Hg
Ha
RC 34.5
RC 35.9
RC 32.9

Figure 14.

Figure 15. Tensile stress-strain diagram comparing wet H_2, Hg, and air samples at 24 C with hardness RC 45 at an initial strain rate of $1 \cdot 10^{-4}\ s^{-1}$

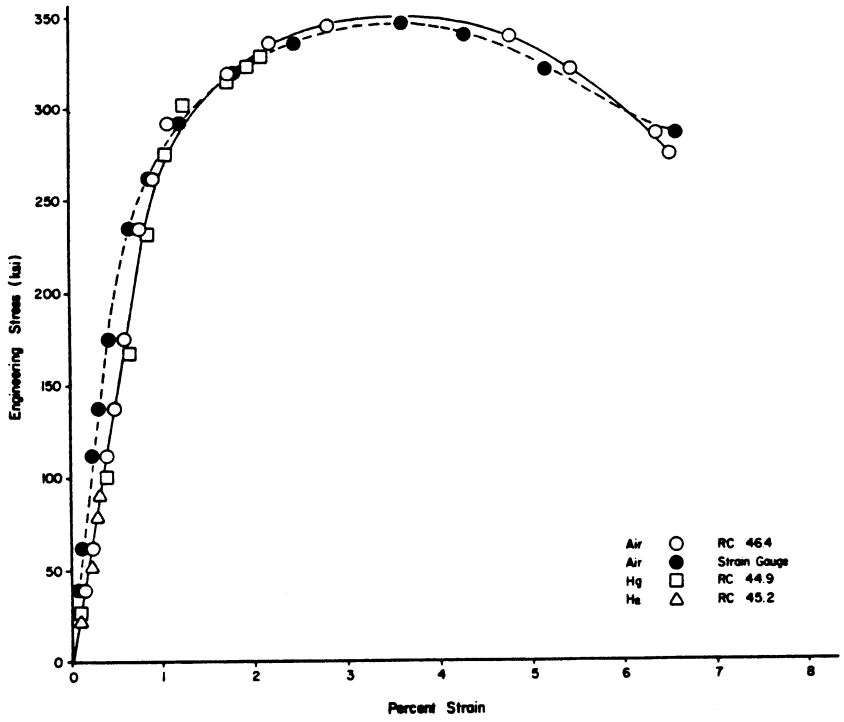
Engineering Stress (ksi)
Percent Strain
Air RC 46.4
Air Strain Gauge
Hg RC 44.9
He RC 45.2

Figure 15.

Figure 16. A tensile stress-strain diagram of samples in a Hg environment to illustrate the change in curve as a function of hardness

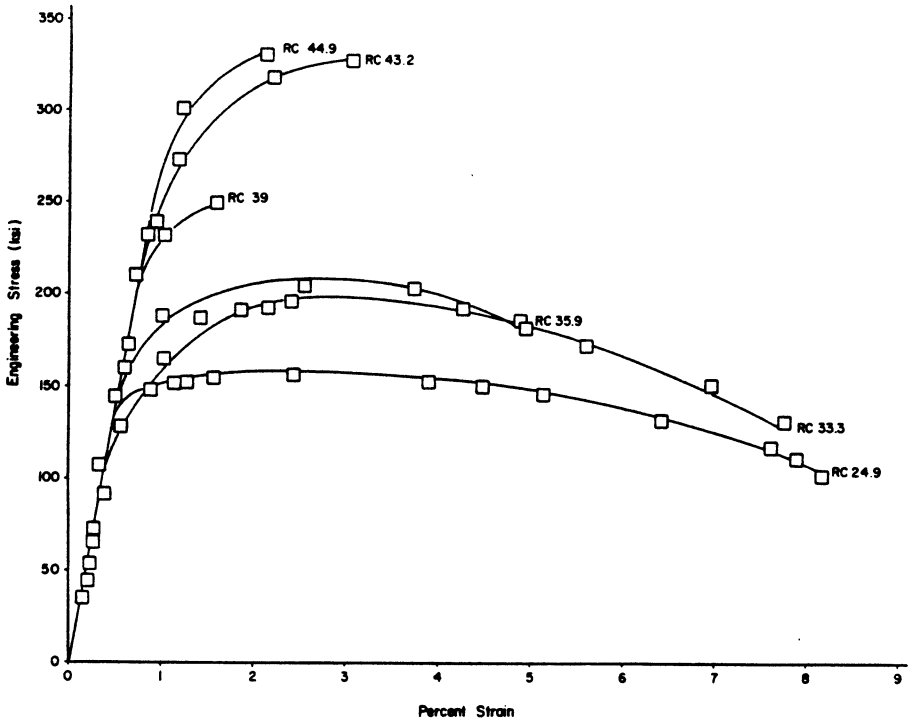
RC 44.9
RC 43.2
RC 39
RC 35.9
RC 33.3
RC 24.9
Engineering Stress (ksi)
Percent Strain
0
50
100
150
200
250
300
350
0
1
2
3
4
5
6
7
8
9

Figure 16.

Figure 17. A comparative diagram of the ultimate strength and fracture strengths to hardness of wet H_2 and Hg samples at 10^{-5} to 10^{-4} s^{-1}. Dark points represent 10^{-5} s^{-1} while light points represent 10^{-4} s^{-1}

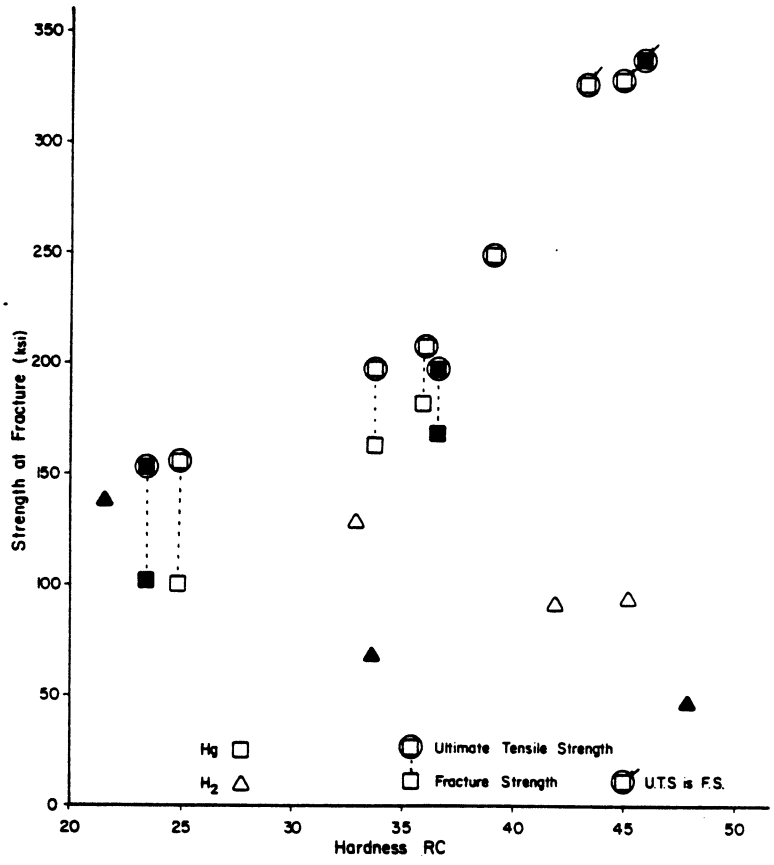
Strength at Fracture (ksi)
350
300
250
200
150
100
50
0
20
25
30
35
40
45
50
Hardness RC
Hg
H2
Ultimate Tensile Strength
Fracture Strength
U.T.S is F.S.

Figure 17.

Figure 18. A diagram of the ultimate strength and fracture strengths to hardness of air samples at 10^{-5} to 10^{-4} s^{-1}. Dark points represent 10^{-5} s^{-1} while light points represent 10^{-4} s^{-1}

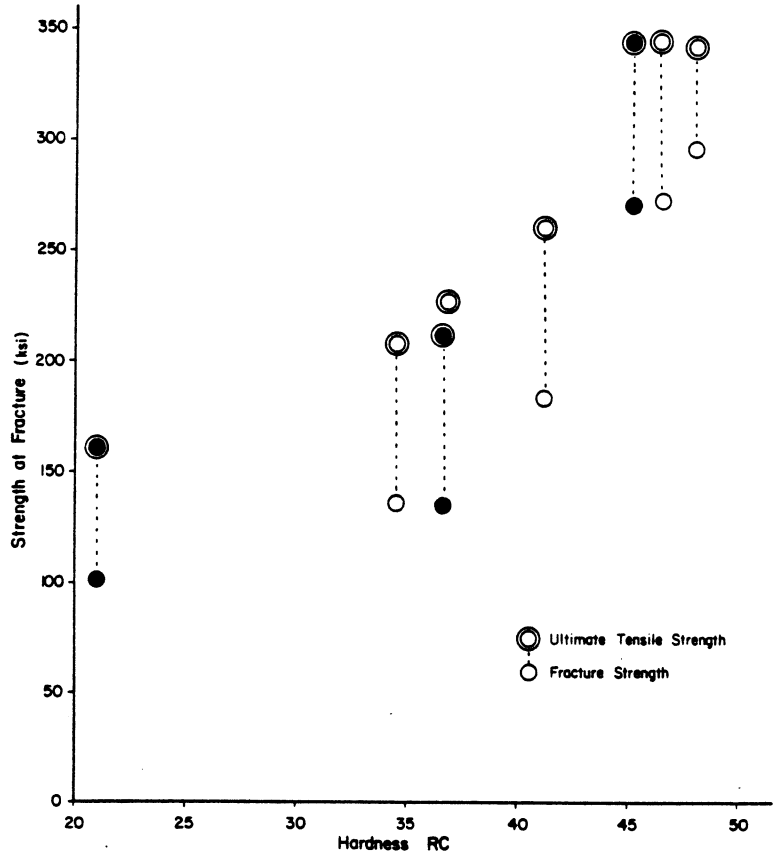
350
300
250
200
150
100
50
0
Strength at Fracture (ksi)
20
25
30
35
40
45
50
Hardness RC
Ultimate Tensile Strength
Fracture Strength

Figure 18.

Figure 19. A comparative diagram of the strain at fracture to hardness of wet H_2, Hg, and air samples at 10^{-5} to $10^{-4} s^{-1}$. Darks points represent $10^{-5} s^{-1}$ while light points represent $10^{-4} s^{-1}$

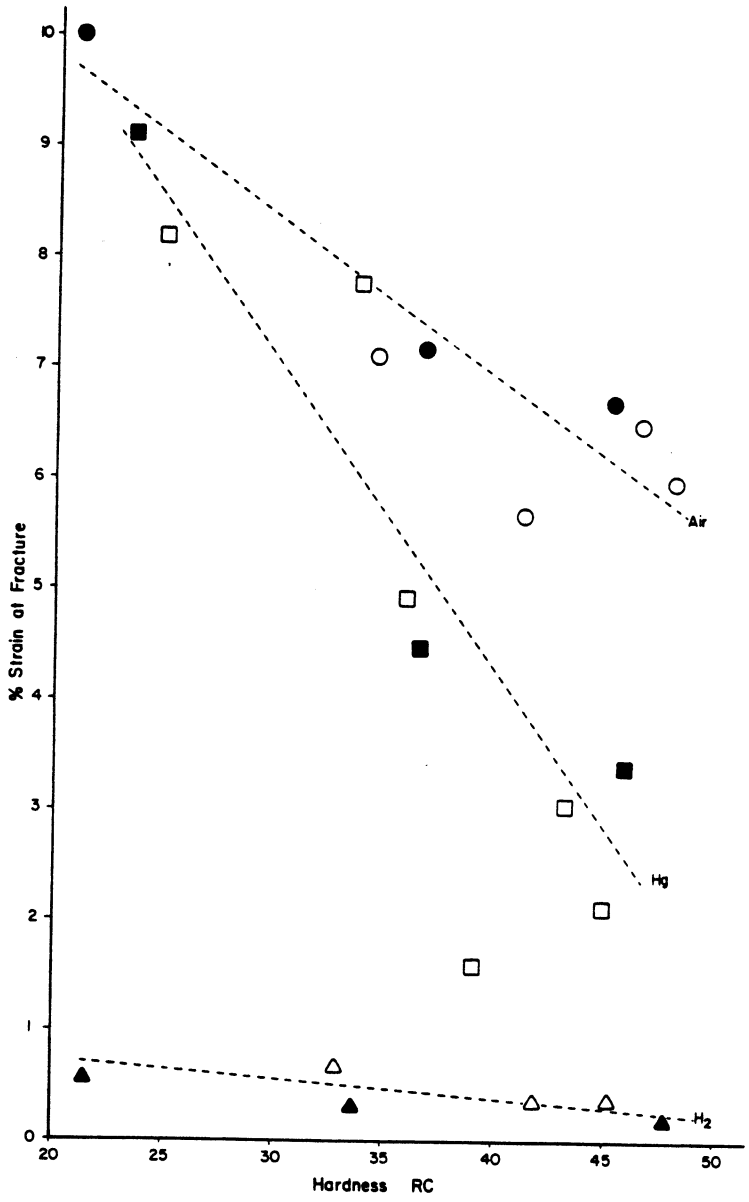
% Strain at Fracture
Hardness RC
Air
Hg
H2
0
1
2
3
4
5
6
7
8
9
10
20
25
30
35
40
45
50

Figure 19.

Figure 20. A comparative diagram of percent strain at ultimate tensile strength, SATS, and at yield strength, SAY, to hardness in air. Darks points represent 10^{-5} s^{-1} while light points represent 10^{-4} s^{-1}

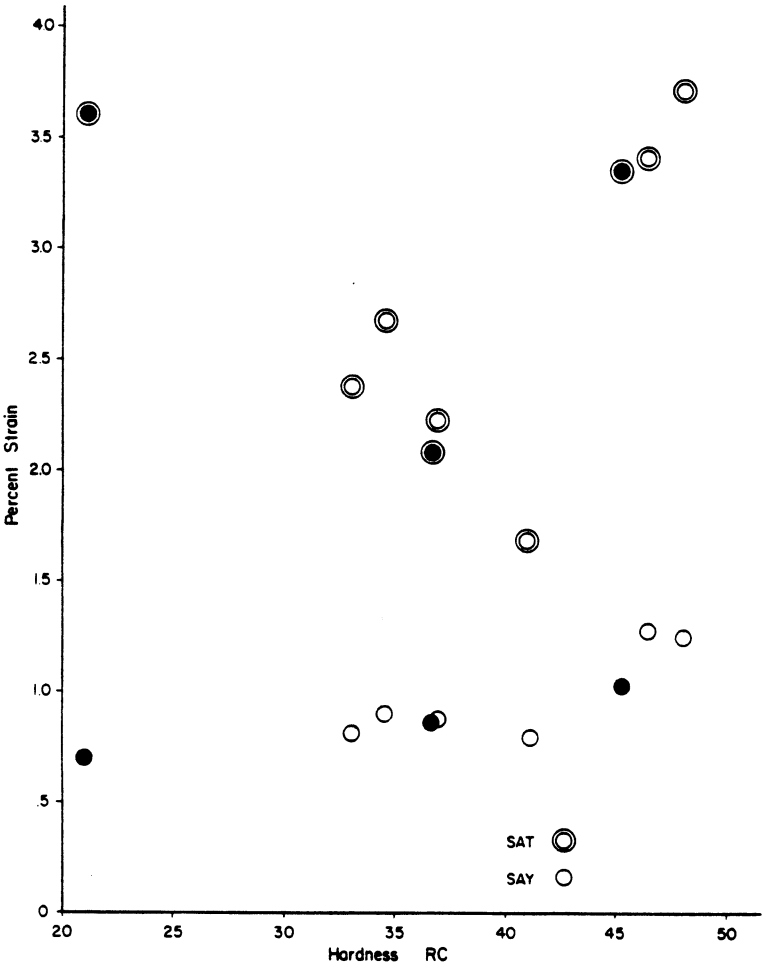
Percent Strain
4.0
3.5
3.0
2.5
2.0
1.5
1.0
.5
0
20
25
30
35
40
45
50
Hardness RC
SAT
SAY

Figure 20.

Figure 21. A comparative diagram of percent strain at ultimate tensile strength, SATS, and at yield strength, SAY, to hardness in Hg . Dark points represent 10^{-5} s^{-1}

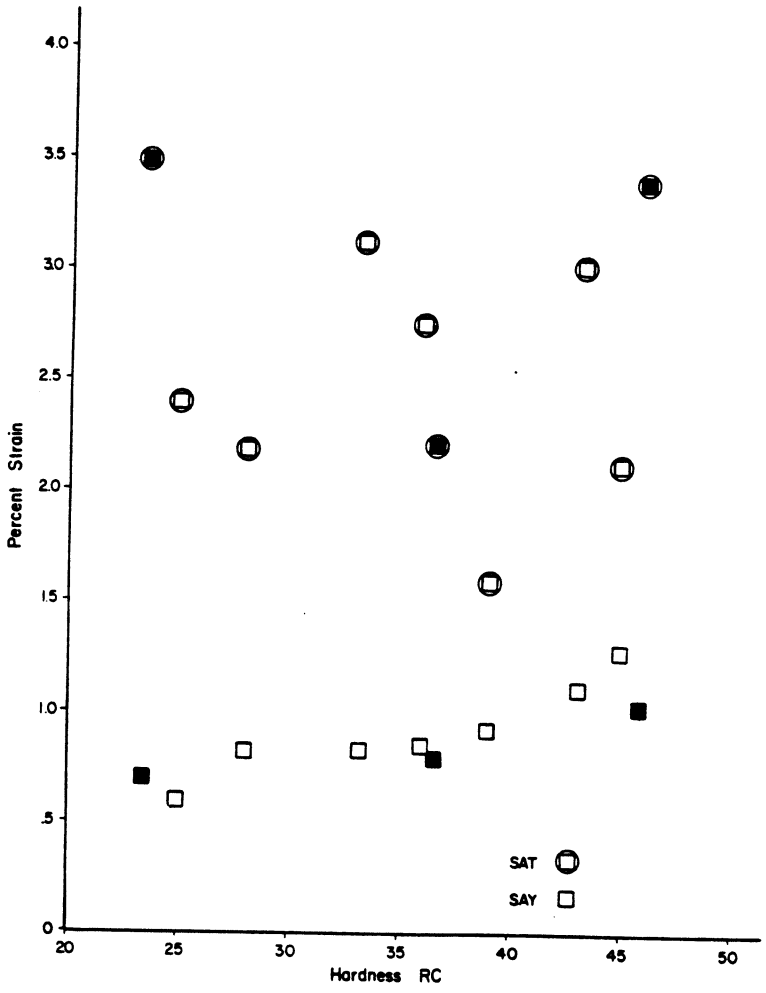
Percent Strain
4.0
3.5
3.0
2.5
2.0
1.5
1.0
.5
0
20
25
30
35
40
45
50
Hardness RC
SAT
SAY

Figure 21.

Figure 22. A yield strain energy to hardness diagram of samples in Hg and air at 10^{-5} to 10^{-4} s^{-1} to illustrate the crack initiation phase in Hg. Dark points represent 10^{-5} s^{-1} while light points represent 10^{-4} s^{-1}

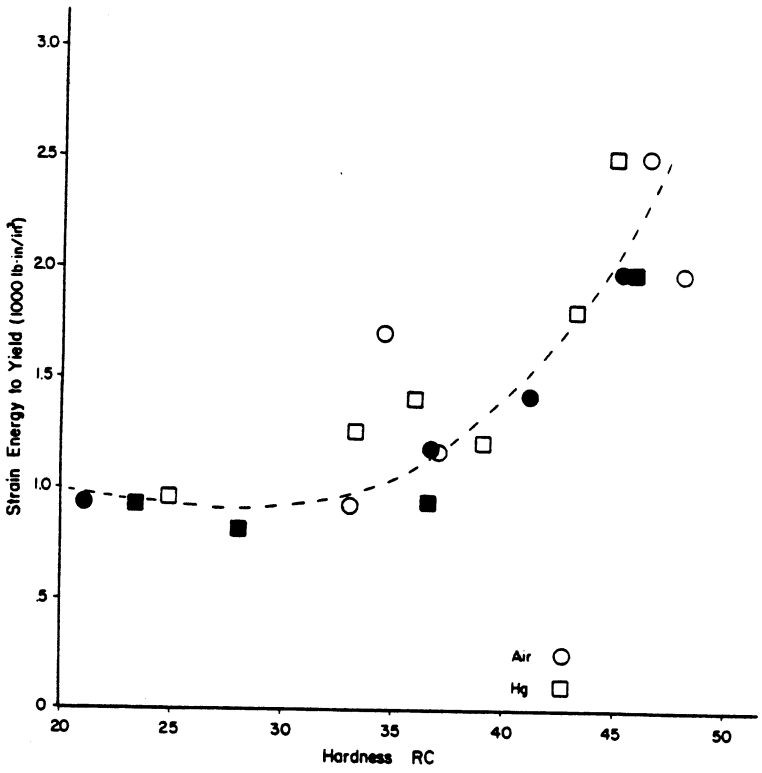
Strain Energy to Yield (1000 lb-in/in³)
3.0
2.5
2.0
1.5
1.0
.5
0
20
25
30
35
40
45
50
Hardness RC
Air
Hg

Figure 22.

Figure 23. A fracture strain energy to hardness diagram of samples in wet H_2, Hg, and air at 10^{-5} to 10^{-4} s^{-1} to illustrate the fracture characteristics of tensile specimens. Dark points represent 10^{-5} s^{-1} while light points represent 10^{-4} s^{-1}

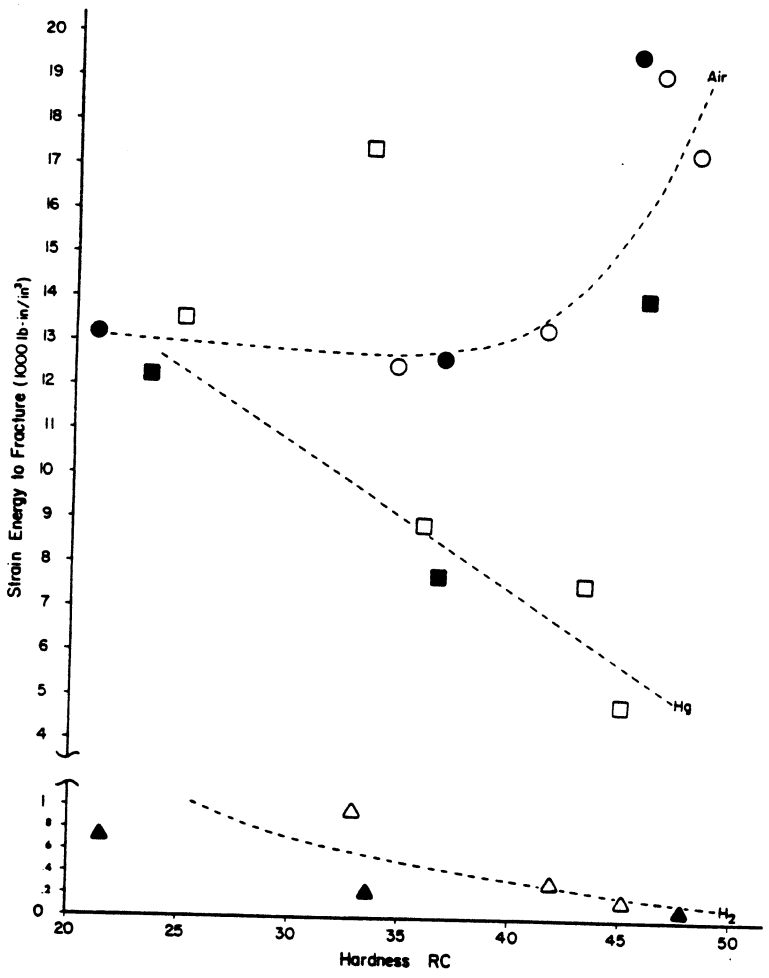
Strain Energy to Fracture (1000 lb-in/in³)
Hardness RC
Air
Hg
H₂

Figure 23.

Figure 24. A plastic work to hardness diagram of samples in Hg and air at 10^{-5} to $10^{-4}s^{-1}$ to illustrate the crack propagation phase in Hg. Dark points represent $10^{-5}s^{-1}$ while light points represent $10^{-4}s^{-1}$

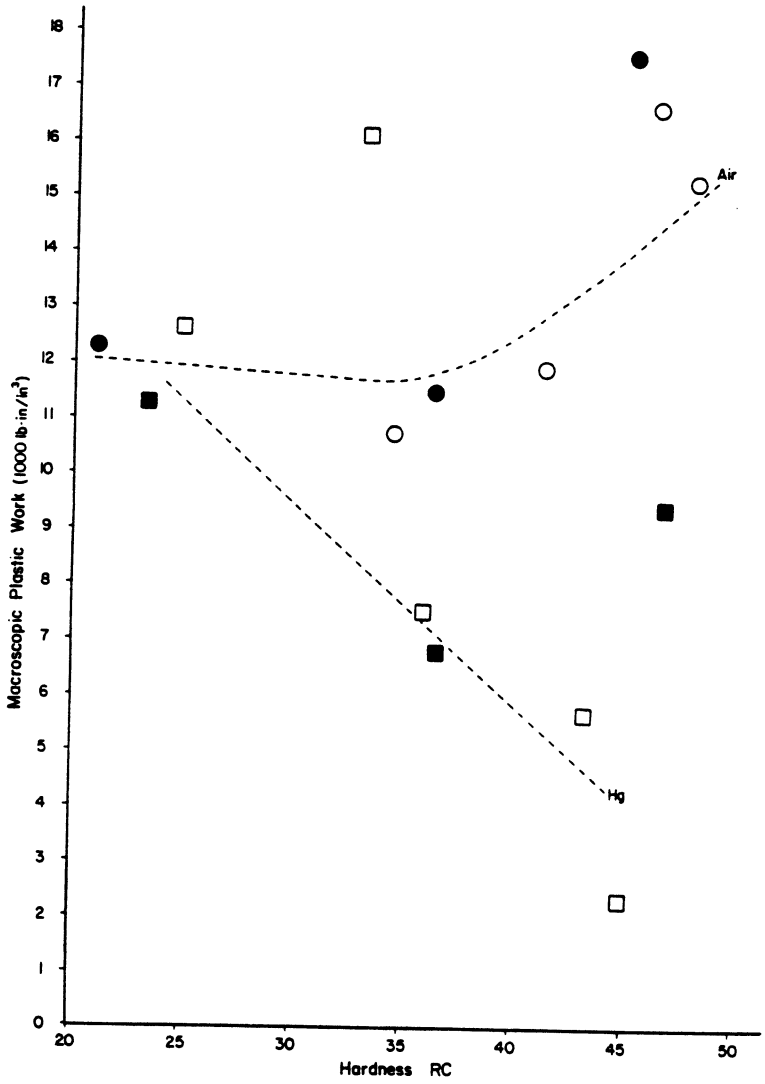
Macroscopic Plastic Work (1000 lb·in/in³)
Hardness RC
Air
Hg
0
1
2
3
4
5
6
7
8
9
10
11
12
13
14
15
16
17
18
20
25
30
35
40
45
50

Figure 24.

Figure 25. Typical cup and cone fracture of specimen 7-2, RC 21 at a strain rate 10^{-5} s^{-1} in air. Note the radial tear ridges along with extensive secondary cracking

Figure 26. Cup and cone fracture of specimen 9-1, RC 34.5 at a strain rate 10^{-4} s^{-1} in air. The reduction in area is less than that in Fig. 24 and the radial ridges are much more pronounced and cover a greater area with less visible secondary cracking

Figure 25.

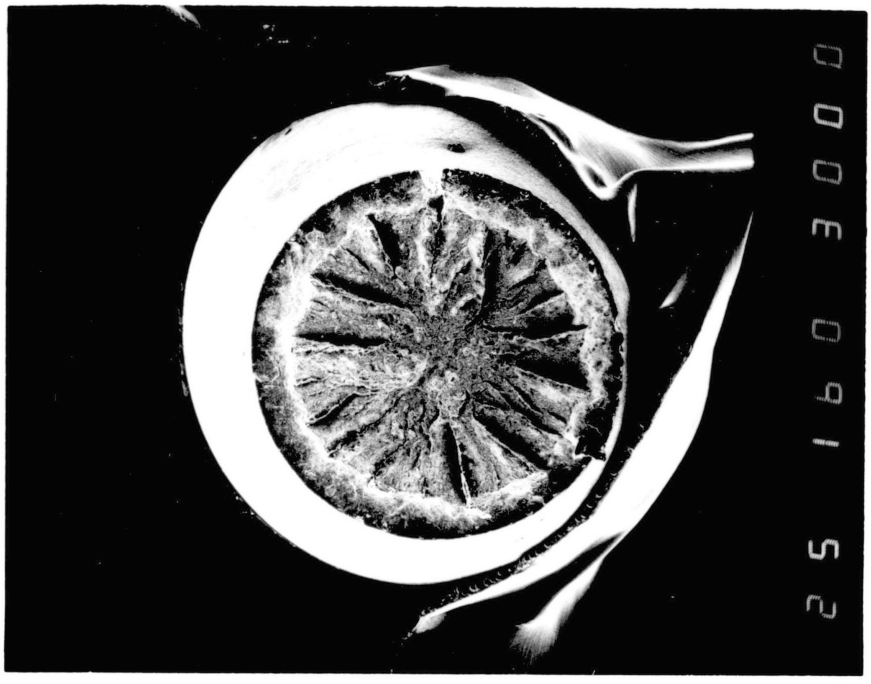

Figure 26.

Figure 27. Cup and cone fracture of specimen 8-4, RC 45.2 at a strain rate 10^{-5} s^{-1} in air. The higher hardness results for Fig.27 radial tear ridges disappear as well as the secondary cracking

Figure 28. A typical microvoid appearance from specimen 6-4, RC 33 at strain rate of 10^{-4}, RC 33 at a strain rate of 10^{-4} s^{-1} in air

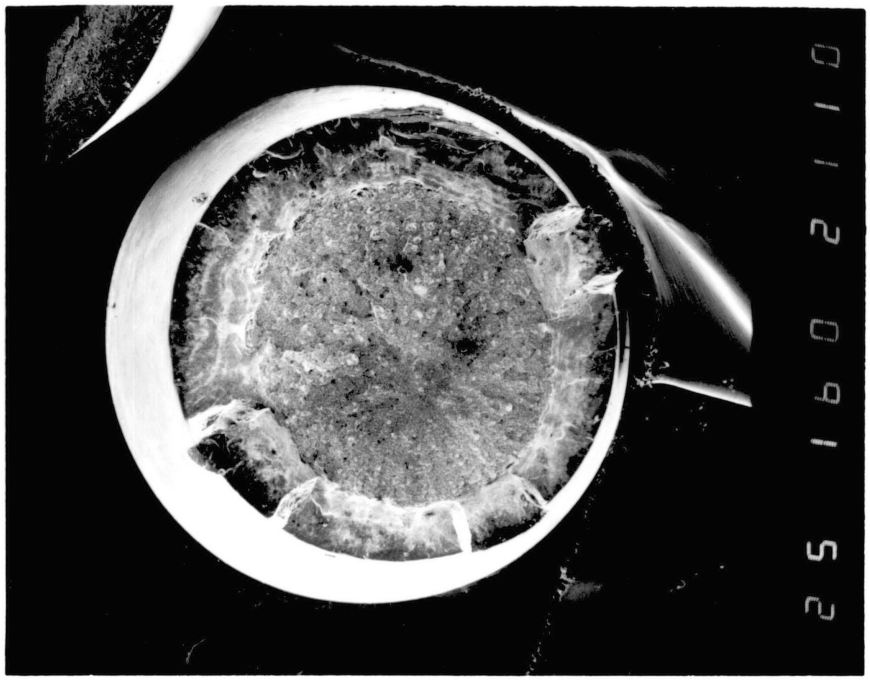

Figure 27.

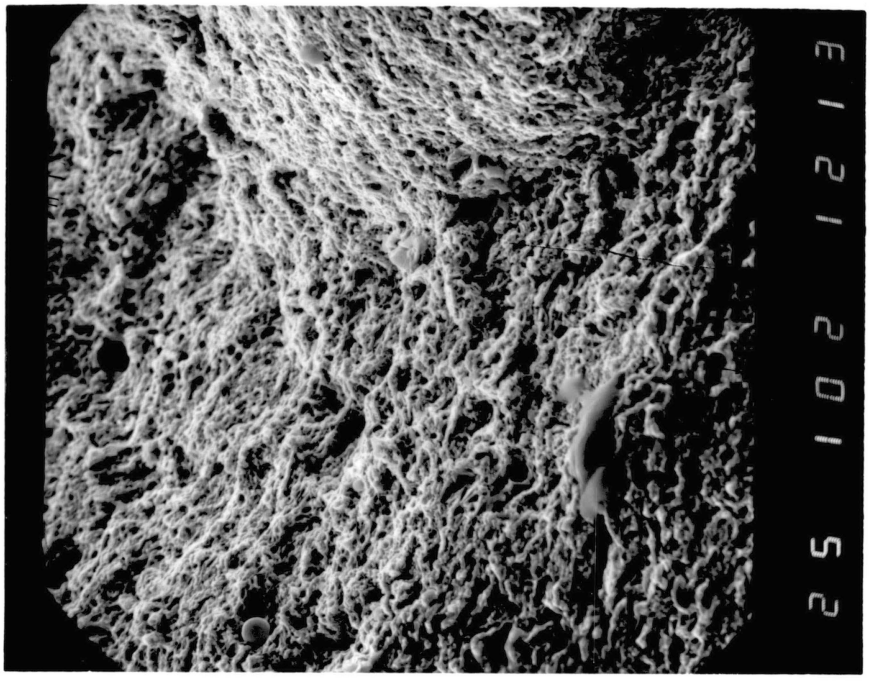

Figure 28.

Figure 29. The vicinity of a secondary crack of specimen 9-4, RC 36.6 at strain rate of $10^{-5}s^{-1}$ in air. The contour change is gradual and the fracture mode is unchanged down into the crack

Figure 30. The fracture of specimen 7-1, RC 23.4 at a strain rate of $10^{-5}s^{-1}$ in mercury. Note the multiple origin, the additional side cracks and the much greater reduction in area compared to the following two figures. There are several major and minor secondary cracks

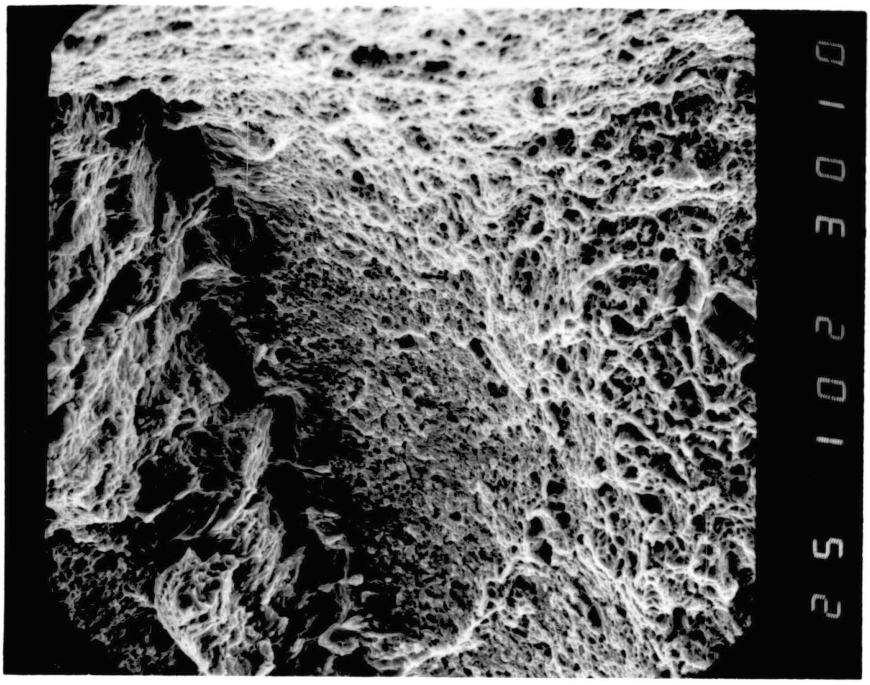

Figure 29.

Figure 30.

Figure 31. The fracture of specimen 9-5, RC 36.5 at a strain rate of 10^{-5} s^{-1} in mercury. Fractures in mercury at hardnesses of RC 30 to 40 originate from the edge as illustrated here. The final fracture area has a radial texture

Figure 32. The fracture of specimen 8-5, RC 45.7 at a strain rate of 10^{-5} s^{-1} in mercury. Fracture begins at an edge location and in the final fracture zone shows a horseshoe shaped shear lip as well as fine secondary cracks

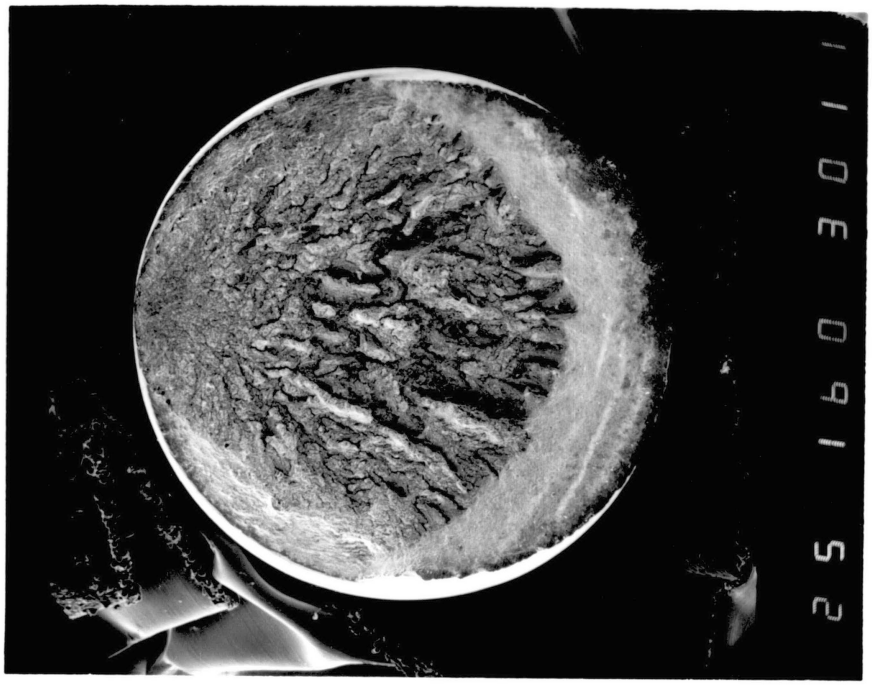

Figure 31.

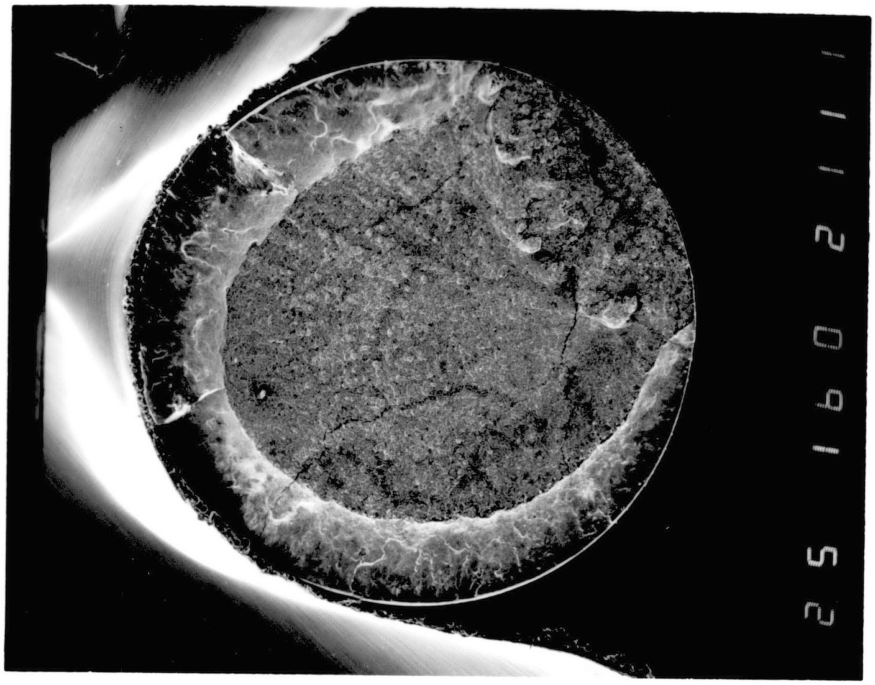

Figure 32.

Figure 33. Crack initiation for samples tested in mercury above RC 30 hardness. They are intergranular as seen in this edge view of Fig. 32

Figure 34. Transition to microvoid coalesence from intergranular. At the transition to microvoids secondary cracking is very evident in this magnification of the transition zone of Fig. 32

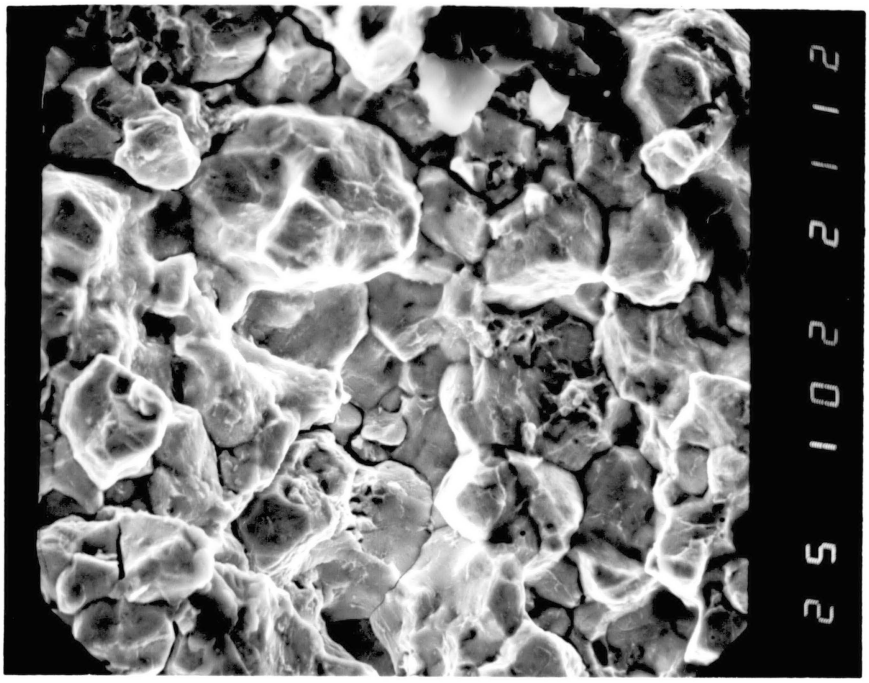

Figure 33.

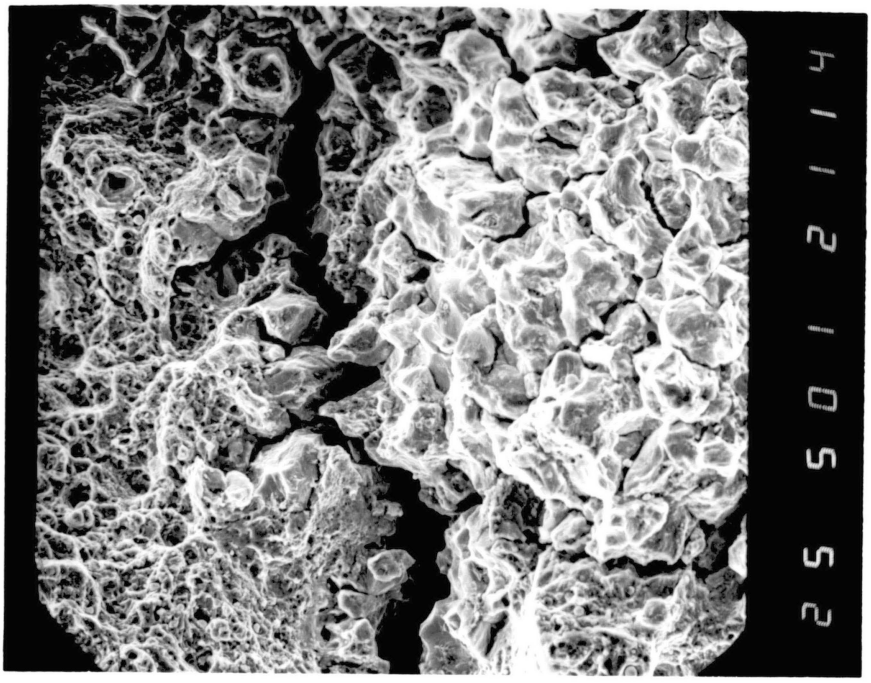

Figure 34.

Figure 35. Jagged, shallow microvoids of Fig. 32 at a major secondary crack giving way to final fracture shear slip

Figure 36. Transgranular initiation of Fig. 30. Very extensive secondary cracking masks the nature of transgranular fracture

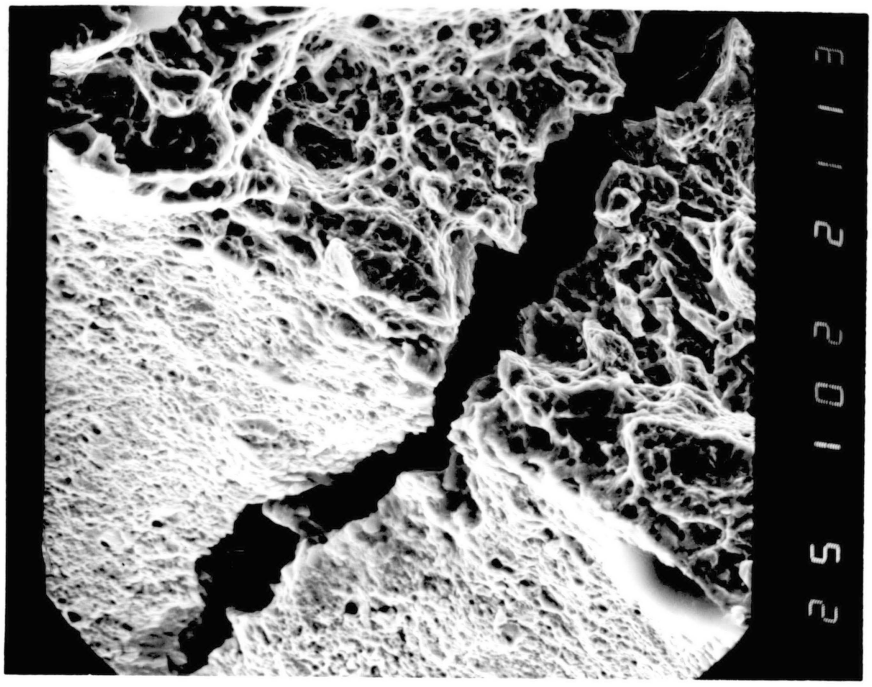

Figure 35.

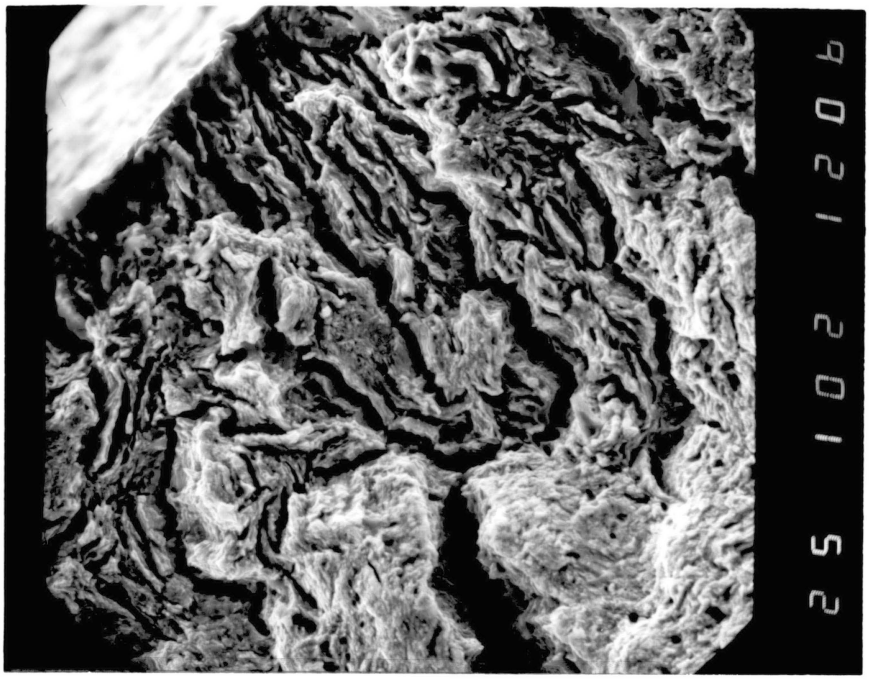

Figure 36.

Figure37. Fracture of specimen 7-3, RC 21.5 at a strain rate of $10^{-5}s^{-1}$ in hydrogen

Figure38. Fracture of specimen 9-6, RC 33.6 at a strain rate of $10^{-5}s^{-1}$ in hydrogen. The Fracture appearance Figures 37 and 38 are generally darker than those of the higher strain rate Figures 39 and 40. The lower strain rates show more microvoid are and less visible tear ridges

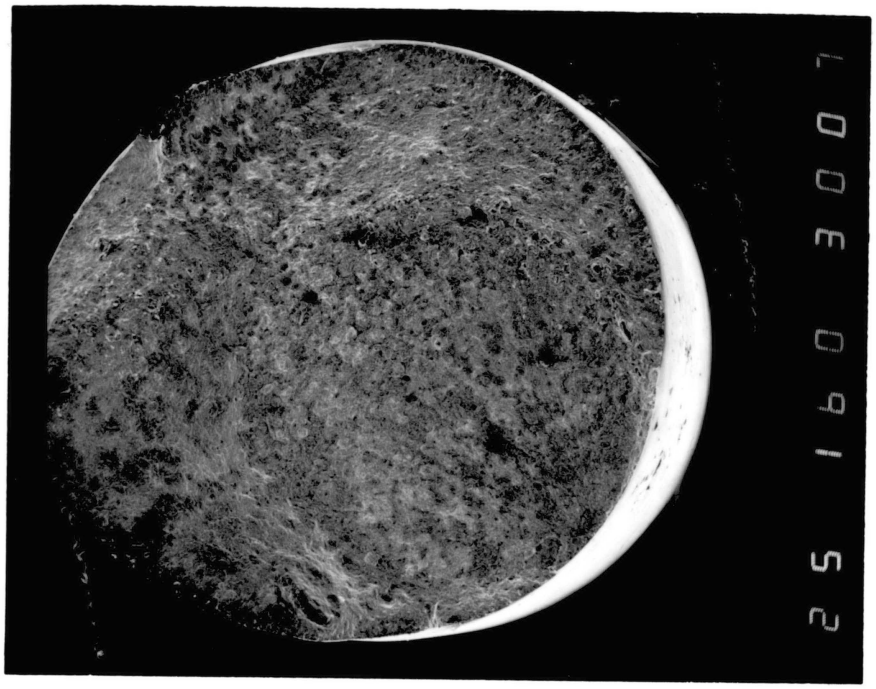

Figure 37.

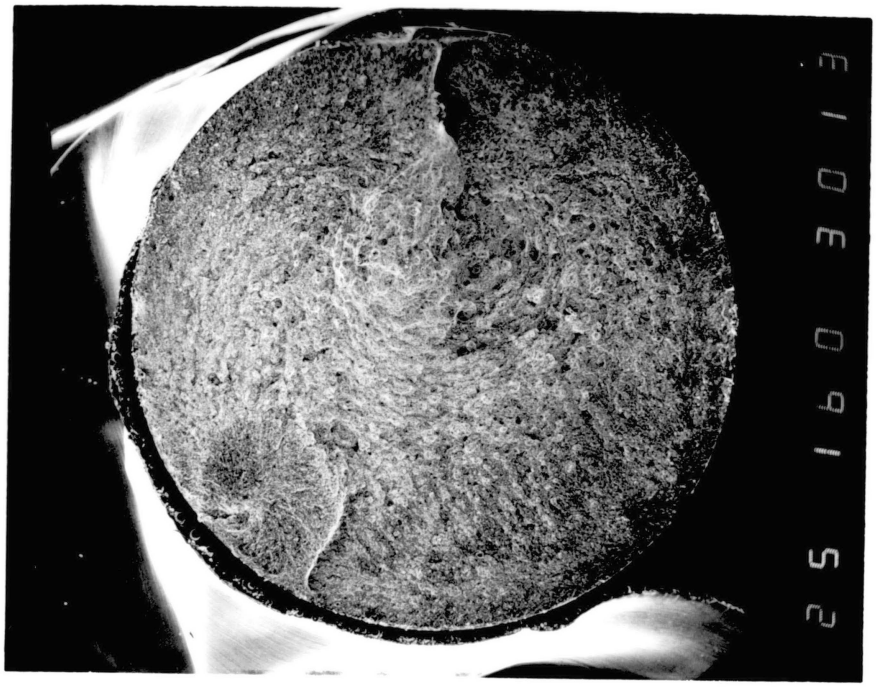

Figure 38.

Figure 39. Fracture of specimen 9-3, RC 32.9 at a strain rate of $10^{-4}s^{-1}$ in hydrogen. Several original regions are observed with a sequence of transgranular at origin to intergranular to microvoids at final fracture zone

Figure 40. Fracture of specimen 8-3, RC 45.2 at a strain rate of $10^{-4}s^{-1}$ in hydrogen. Several origin regions are observed with a sequence of transgranular at oreigin to intergranular to microvoids at final fracture zone

Figure 39.

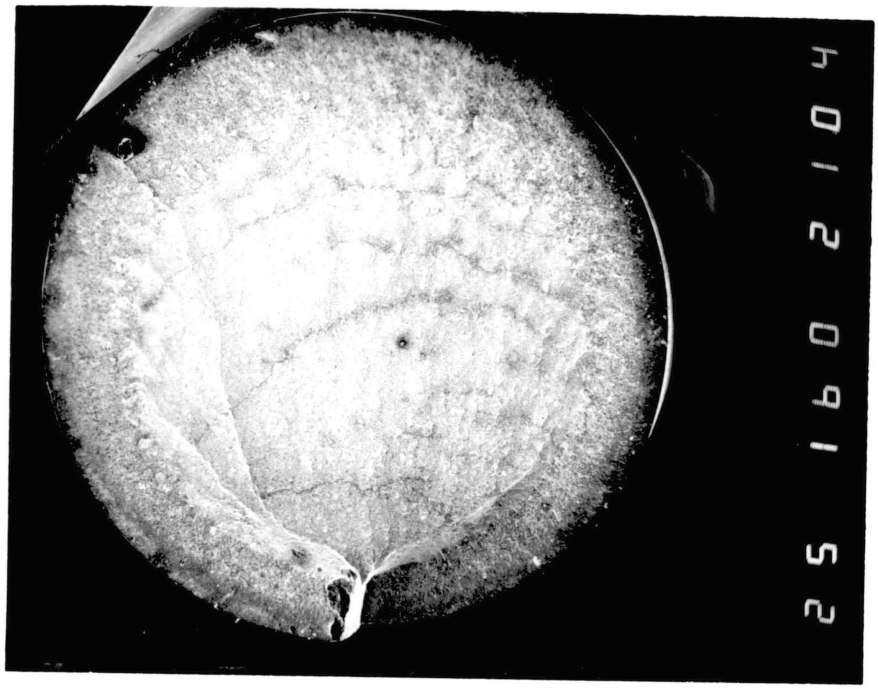

Figure 40.

Figure41. A tilted view of the bottom of Fig. 40. From bottom to top, the dark transgranular fracture of initiation works into an intergranular fracture. At the transiton nto microvoids from intergranular secondary cracks appear

Figure42. Typical transgranular fracture in hydrogen at edge of Fig. 40

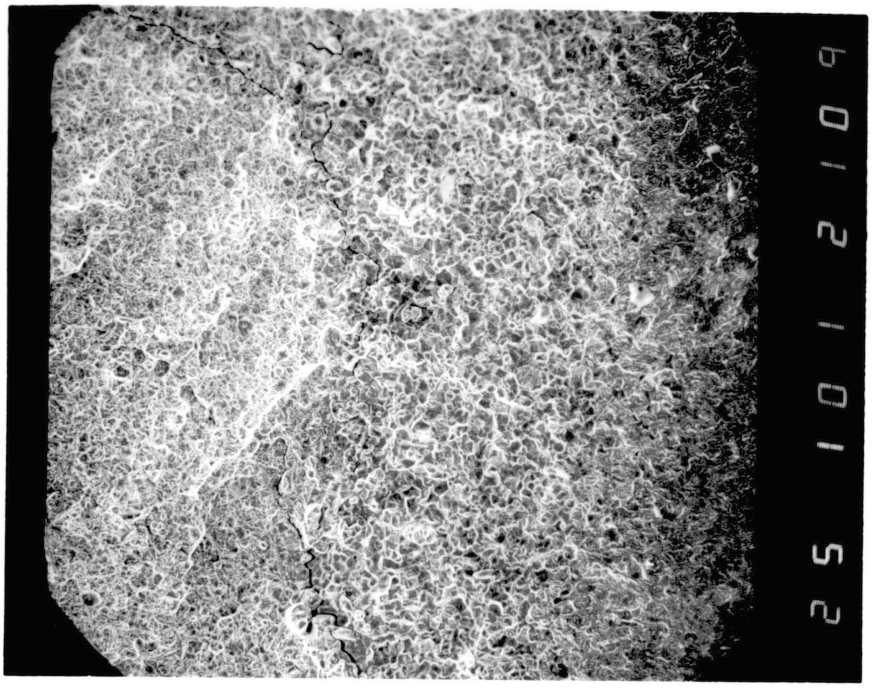

Figure 41.

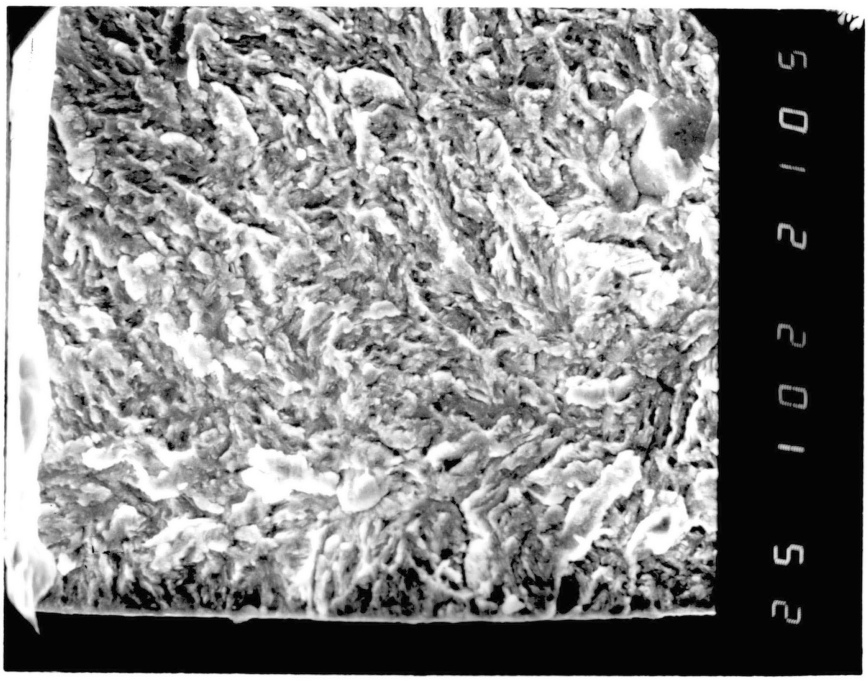

Figure 42.

Figure 43. Typical intergranular fracture of Fig. 40

Figure 44. Secondary cracks transverse to a tear ridge at transion of intergranualr to microvoids of Fig. 40

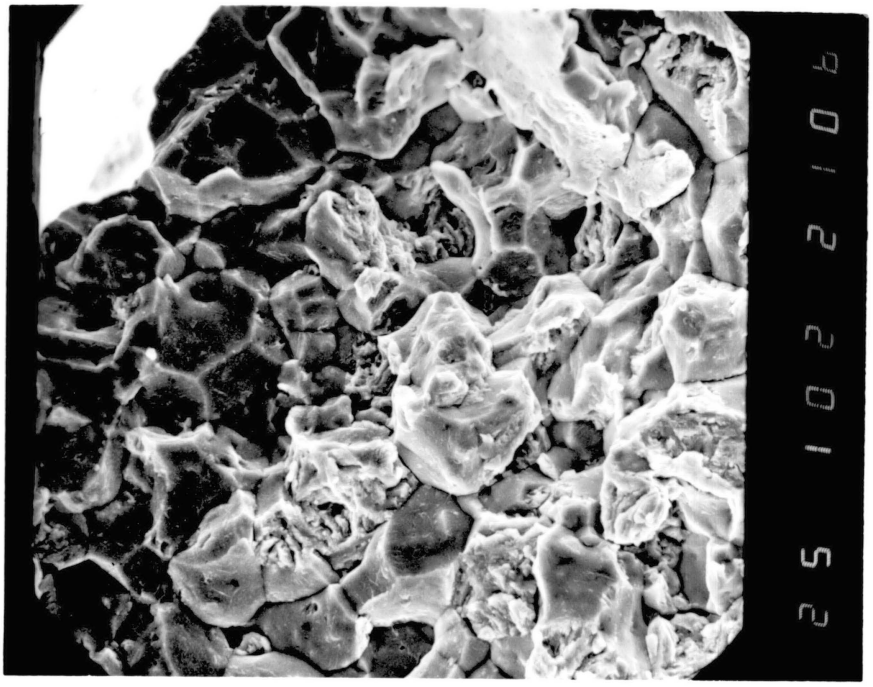

Figure 43.

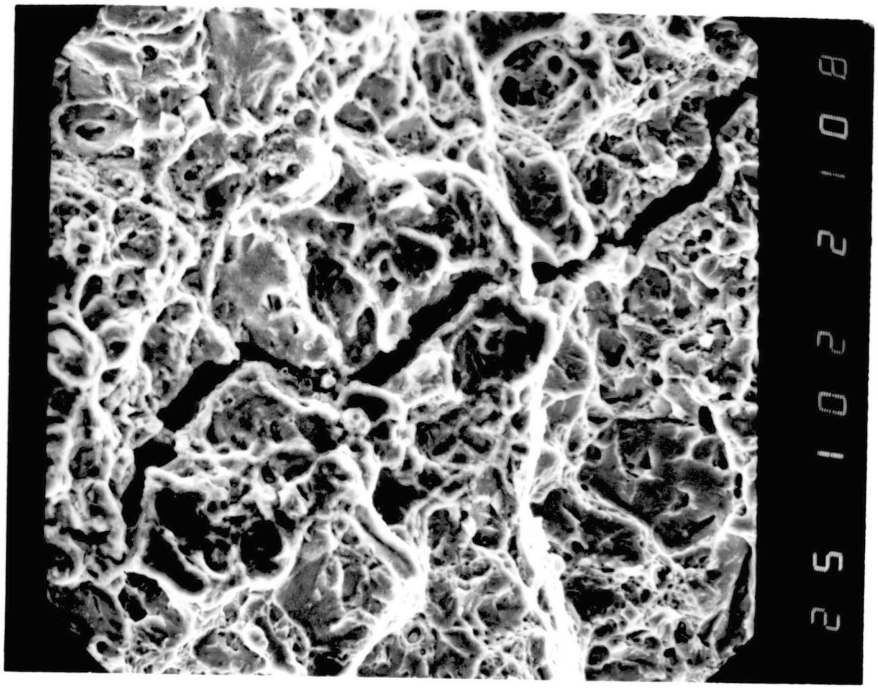

Figure 44.

Figure45. Abrupt transiton of intergranular fracture to final fracture by microvoid coalesence at a major tear ridge

Figure46. Transition of microvoids to a partially intergranular mostly transgranular fracture of Fig. 39. Secondary cracking is not as evident here as they are in Fig. 44

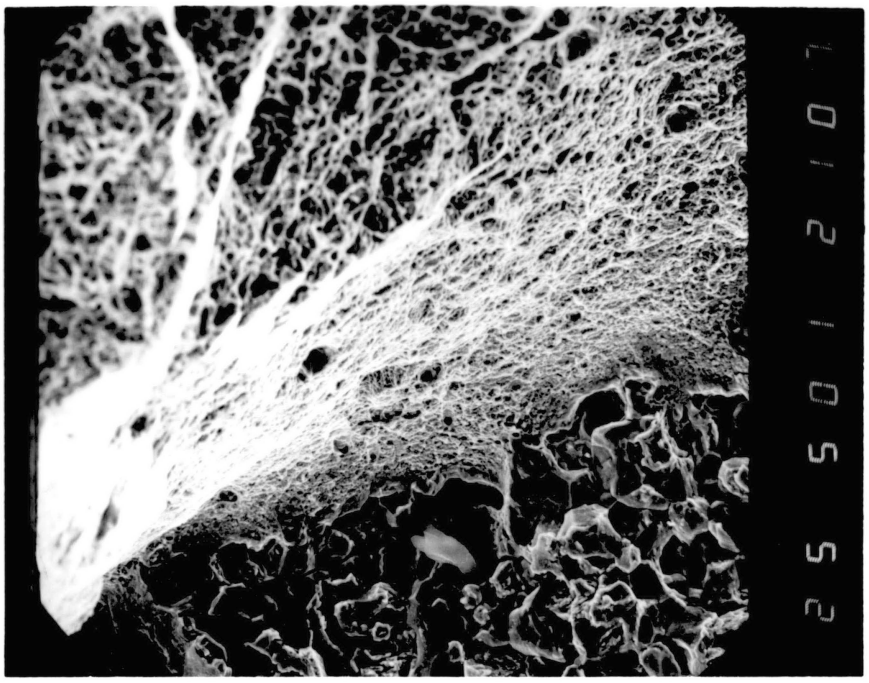

Figure 45.

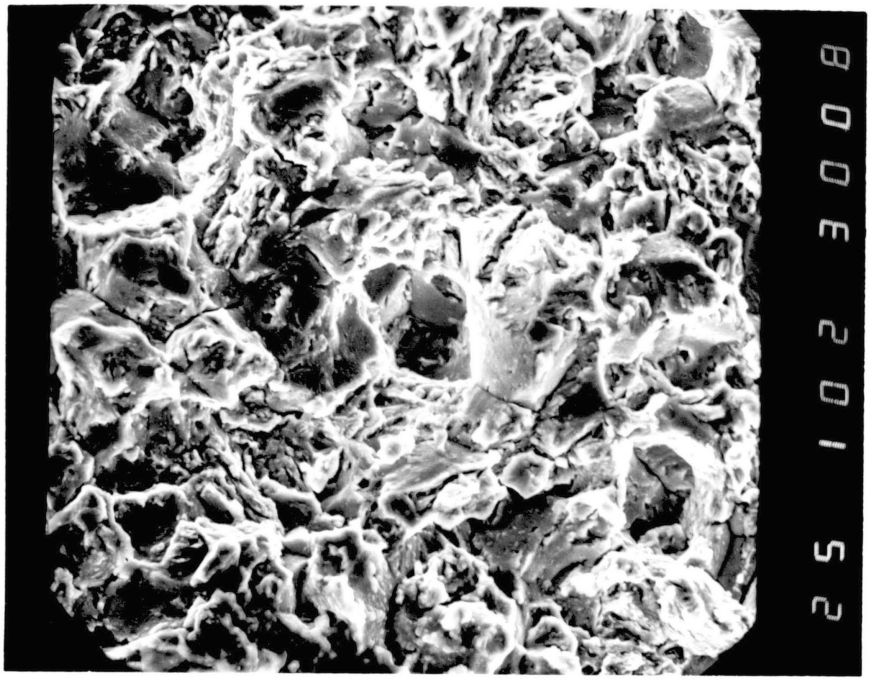

Figure 46.

Figure47. Microvoid coalesence of middle area of Fig. 39. The microvoids are sharper and deeper than those found in the middle of the higher hardness sample of Fig. 40

Figure48. Fractography of fatigue specimen in air, RC 34.1 cycled at 30 Htz with FS at 88% UTS. The sample is slightly turned to show crack propagation from smooth transgranular to ridged transgranular final fracture

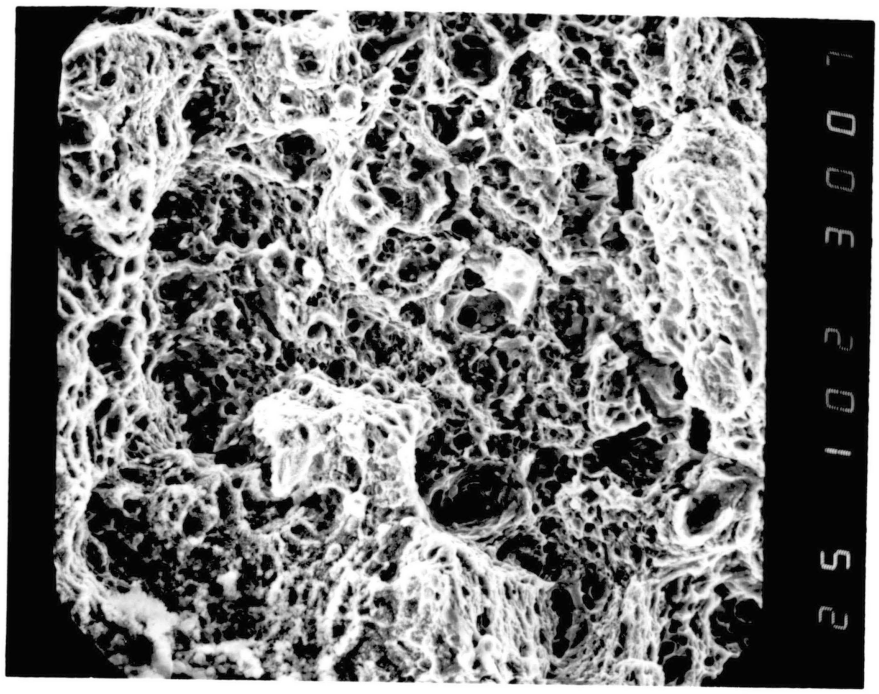

Figure 47.

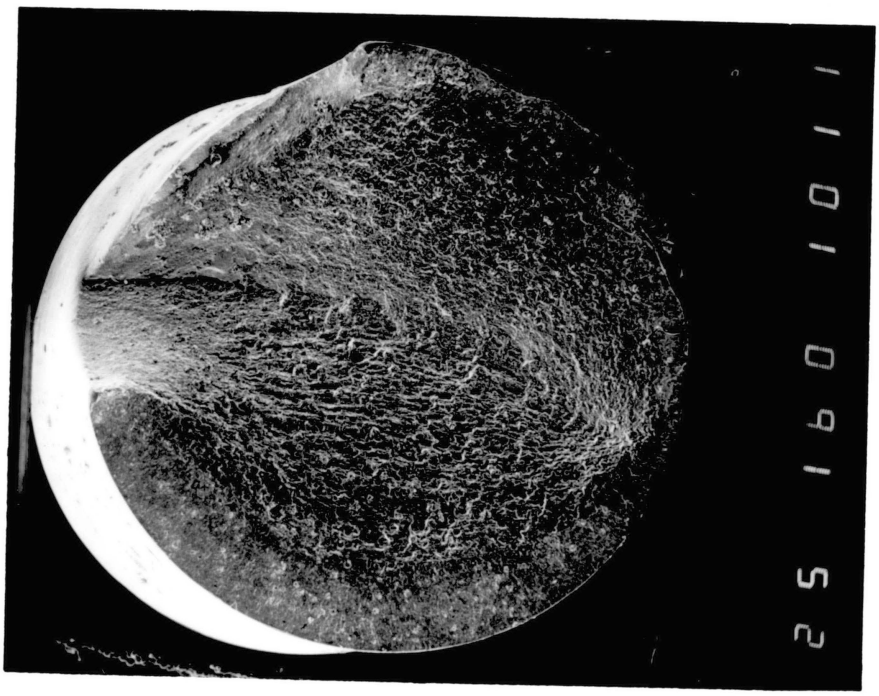

Figure 48.

Figure49. Edge view of Fig. 48 to show transgranular initiation. Tensile fracture in Fig. 42 in hydrogen is similar in appearance to this fatigue fracture in air

Figure50. Interior of Fig. 48 to illustrate the fatigue zone with secondary cracks throughout ridged transgranular region

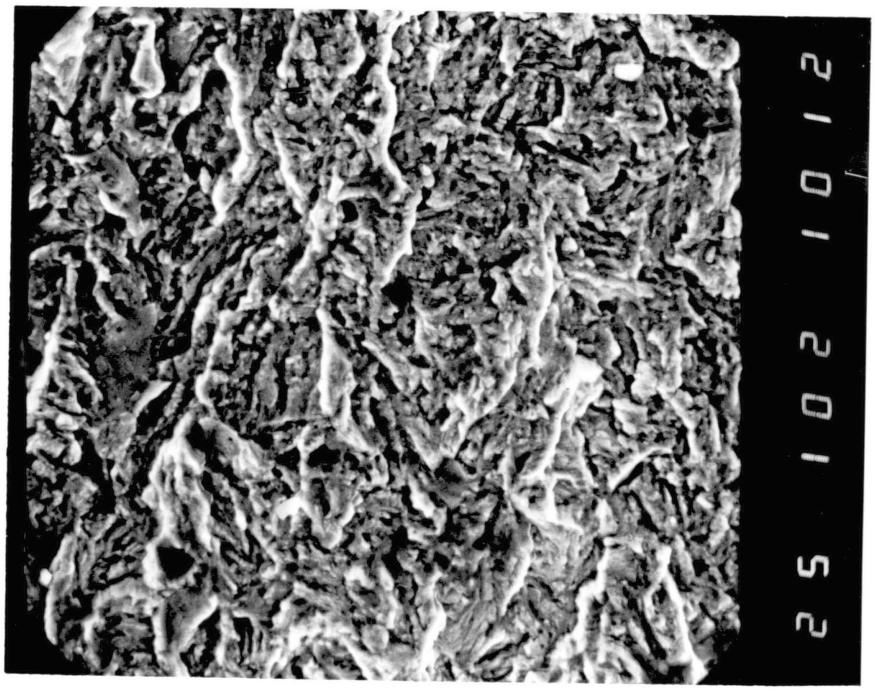

Figure 49.

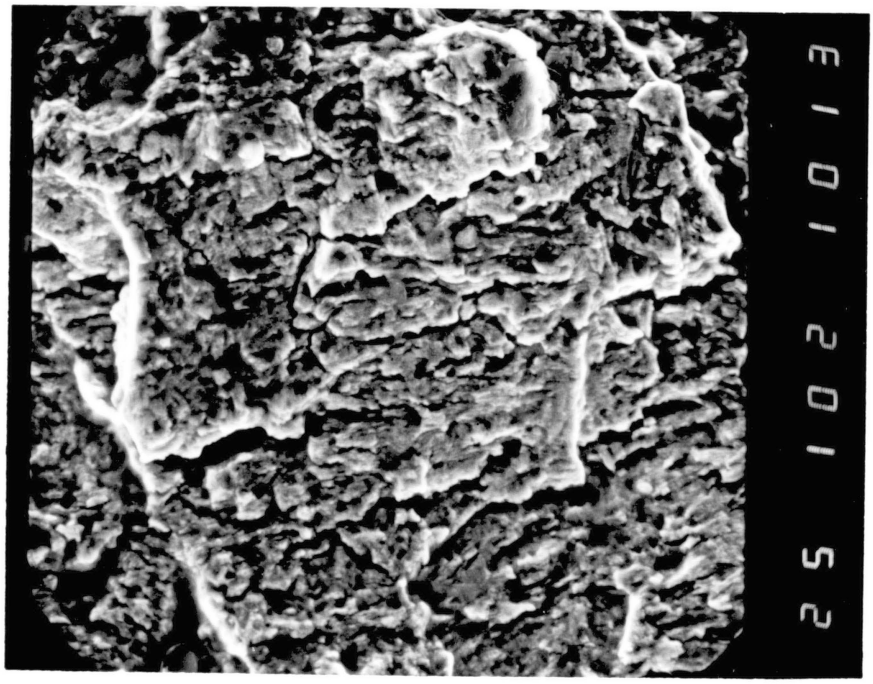

Figure 50.

Figure51. Fractography of fatigue specimen in mercury, RC 33.8 cycled at 30 Htz with FS at 70% UTS

Figure52. Intergranular crack initiation at edge of Fig. 51

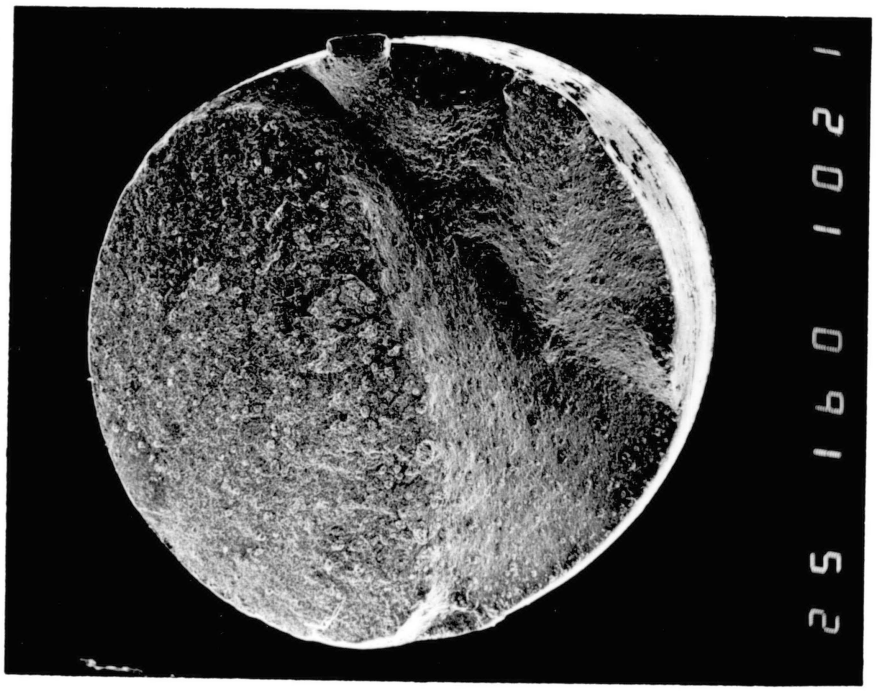

Figure 51.

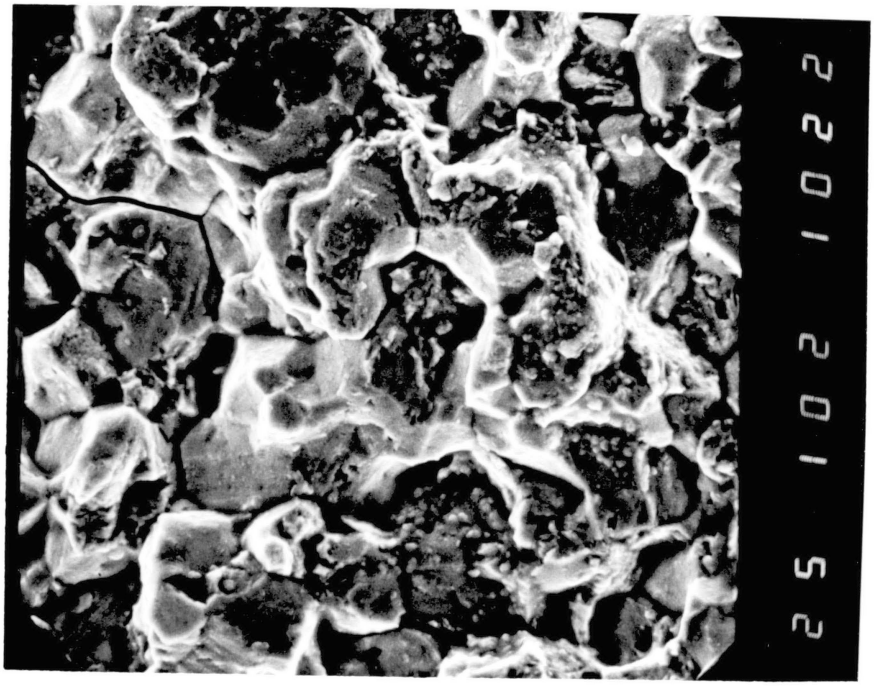

Figure 52.

Figure53. Late fatigue zone with secondary cracks of Fig. 51

Figure54. Fractography of fatigue specimen inhydrogen, RC 33.9 cycled at 30 Htz with FS at 70% UTS

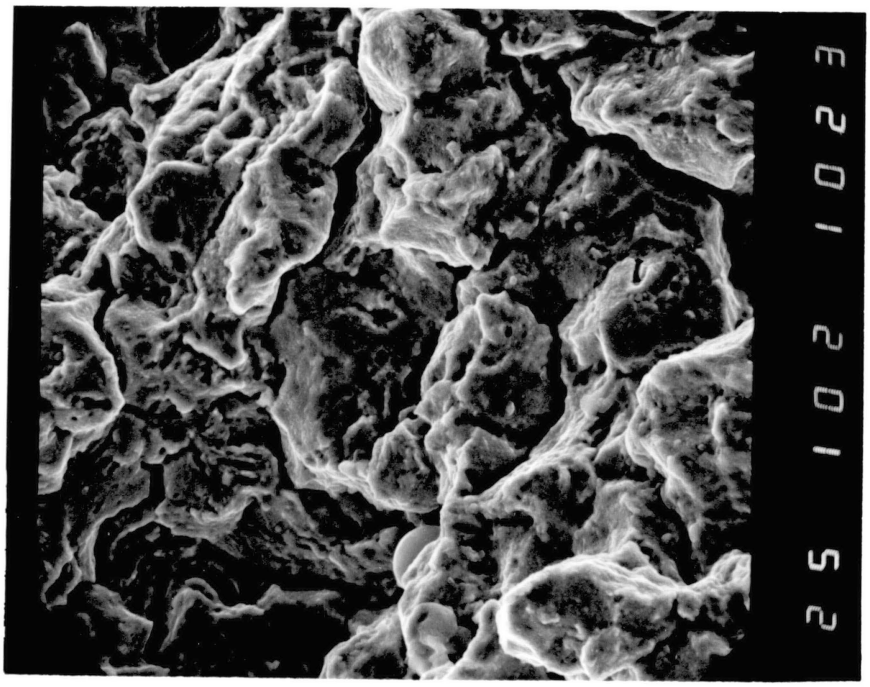

Figure 53.

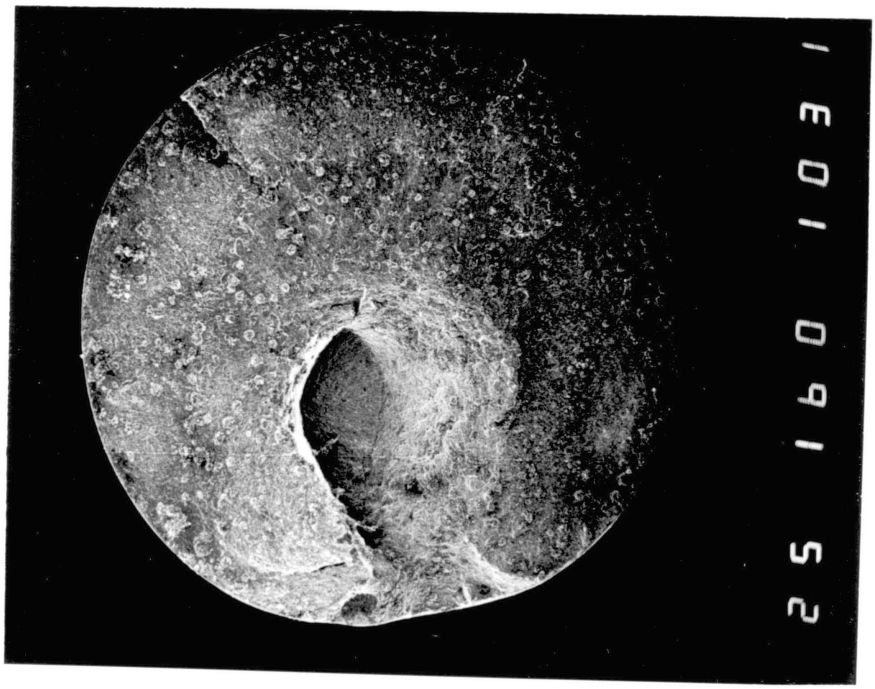

Figure 54.

Figure55. Example of transgranular with intermittant intergranular fracture throughout most of Fig. 54

Figure56. Specimen 8-5 at RC 45.7 in Hg shows longitudinal surface crack transverse to circumferential machining marks

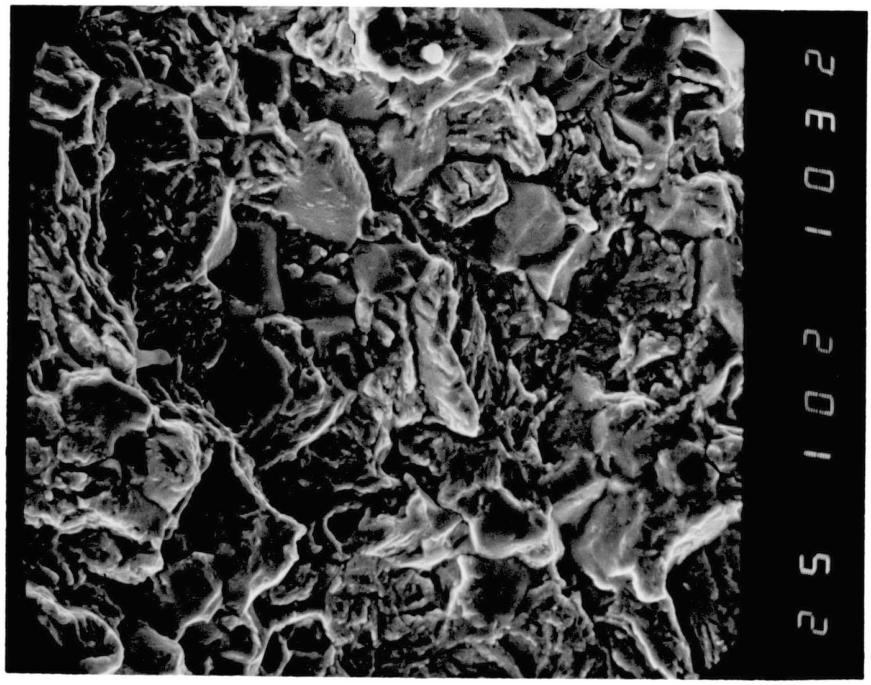

Figure 55.

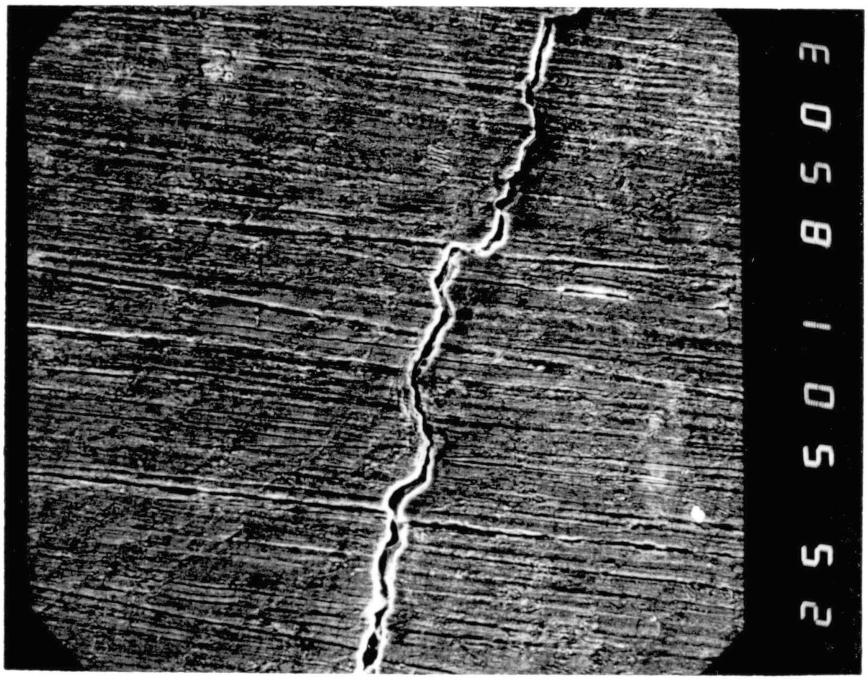

Figure 56.

Figure57. Specimen 7-1 at RC 23.4 in Hg reveals longitudinal surface cracks but also many surface cracks where machine marks used to be. The higher tempering temperature related to grain boundary segregation impurities may explain the difference to Fig. 56

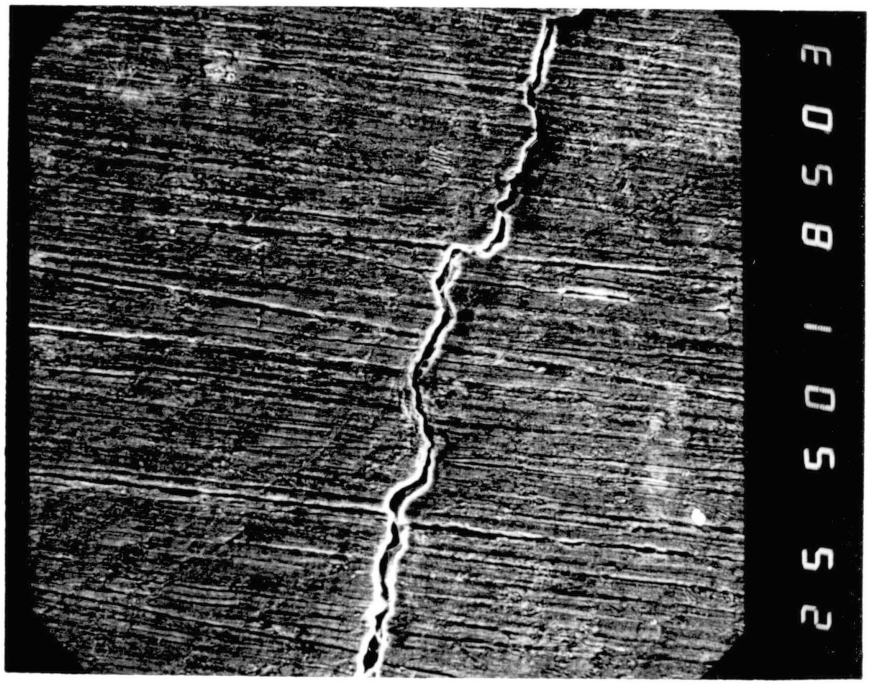

Figure 57.

APPENDIX B

TABLES

TABLE I. PHYSICAL PROPERTIES OF SELECTED ELEMENTS

ELEMENT	SYMBOL	MELTING POINT °C	ATOMIC MASS gm/mole	DENSITY gm/cm^3	MOLAR DENSITY $mole/cm^3$	ATOMIC RADIUS Å	CRYSTAL	VALENCE	ELECTRONEGATIVITY
Helium	He	-269.7	4.00	$.166 \cdot 10^{-3}$	.000041	1.79	(2),(3)	0	Inert
Hydrogen	H	-259.2	1.01	$.084 \cdot 10^{-3}$	.000083	.46	2	-1	1.0
Neon	Ne	-248.6	20.18	$.839 \cdot 10^{-3}$	.000041	1.6	1	0	Inert
Oxygen	O	-218.8	15.99	$1.332 \cdot 10^{-3}$	.000083	.6	6,9	-2	3.5
Nitrogen	N	-210	14.01	$1.165 \cdot 10^{-3}$	.000083	.71	9	5	3.0
Argon	Ar	-189.4	39.95	$1.663 \cdot 10^{-3}$	.000042	1.92	1	0	Inert
Chlorine	Cl	-101	35.45	$3.214 \cdot 10^{-3}$	.000091	1.07	6,1,3,2	-1	3.0
Mercury	Hg	-38.8	200.61	13.55	.067544	1.5	5	2	1.9
Gallium	Ga	29.75	69.72	5.91	.084725	1.35	6	3	1.6
Phosphorus	P	44.25	30.97	1.83	.059082	1.09	6	5	2.1
Potassium	K	63.2	39.10	.86	.021994	2.31	3	1	.8
Sodium	Na	97.85	22.99	.97	.042245	1.86	3	1	.9
Iodine	I	113.7	126.90	4.94	.038927	1.36	6	-1,5	2.5
Sulfur	S	119.0	32.06	2.07	.064558	1.06	6,11	-2,6	2.5
Indium	In	156.63	114.82	7.31	.063665	1.57	7	3	1.7
Lithium	Li	180.55	6.94	.53	.076956	1.52	1,3	1	1.0
Selenium	Se	221	78.96	4.79	.060664	1.16	4,10,11	-2,6	2.4
Tin	Sn	231.87	118.69	7.29	.061491	1.58	8,12	-4,4	1.8
Bismuth	Bi	271.37	208.98	9.80	.046894	1.82	5	3	1.9
Thallium	Tl	304	204.37	11.85	.057983	1.71	2,3	1,3	1.8
Cadmium	Cd	321.03	112.40	8.65	.076957	1.50	2	2	1.7
Lead	Pb	327.45	207.19	11.36	.054828	1.75	1	-4,2,4	1.8
Zinc	Zn	419.58	65.37	7.13	.109117	1.33	2	2	1.6
Antimony	Sb	630.5	121.75	6.62	.054374	1.61	5	-3,5,3	1.9
Magnesium	Mg	650	24.31	1.74	.071569	1.60	2	2	1.2
Aluminum	Al	660	26.98	2.69	.100031	1.43	1	3	1.5
Barium	Ba	729	137.34	3.50	.025484	2.17	3	2	.9
Cerium	Ce	804	140.12	6.77	.048301	1.82	3,2	3,4	1.1

(CONTINUED)

Sources:

Physics of the Atom, 3rd Edition, R.M. Wehr, J.A. Richards, Jr., and T.W. Adair III, eds., Addison-Wesley Publishing Company: Reading, Massachusetts, pp. 496-498 (1978)

Flinn, R.A., and Trojan, P.K., Engineering Materials and Their Applications. Houghton and Mifflin Company: Boston, Massachusetts, pp. 26, 27, 42 (1975)

TABLE I. CONTINUED

Arsenic	As	817	74.92	5.72	.076348	1.25	5	3,5,-3	2.0
Calcium	Ca	838	40.08	1.55	.038673	1.97	1,(2)	2	1.0
Germanium	Ge	937	72.60	5.32	.073278	1.22	8	4	1.8
Silver	Ag	961	107.88	10.49	.097237	1.44	1	1	1.9
Gold	Au	1064	196.97	19.32	.098087	1.44	1	1,3	2.4
Copper	Cu	1083.4	63.54	8.96	.141013	1.25	1	1	1.9
Uranium	U	1132	238	19.07	.080126	1.38	6	4	(1.2)
Manganese	Mn	1244	54.94	7.43	.135243	1.12,1.16,1.37	9α,9β,7	2,3,4	1.5
Beryllium	Be	1287	9.01	1.85	.205055	1.14	3	2	1.5
Silicon	Si	1412	28.09	2.33	.082959	1.17	8	4,-4	1.8
Nickel	Ni	1453	58.71	8.90	.151627	1.25	2,1	2	1.8
Cobalt	Co	1495	58.93	8.85	.150170	1.25,1.26	2,1	2,3	1.8
Iron	Fe	1536.5	55.85	7.87	.140921	1.24,1.26	3,1	2,3	1.8
Titanium	Ti	1670	47.90	4.51	.094092	1.47	2	2,3,4	1.5
Platinum	Pt	1769	195.09	21.45	.109949	1.38	1	2,4	2.2
Zirconium	Zr	1852	91.22	6.49	.071136	1.58	2,3	4	1.4
Chromium	Cr	1857	51.99	7.19	.138279	1.25,1.36	3,2	3,6	1.6
Vanadium	V	1902	50.94	6.10	.119744	1.32	3	3,4,5	1.6
Boron	B	2030	10.81	2.34	.216446	.97	4	3	2.0
Iridium	Ir	2447	192.20	22.50	.117065	1.35	1	4	2.2
Niobium	Nb	2468	92.91	8.57	.092243	1.43	3	4,5	1.6
Molybdenum	Mo	2617	95.94	10.22	.106525	1.36	3	4,6	1.8
Tantulum	Ta	3014	180.95	16.60	.091739	1.47	3	5	1.5
Osmium	Os	3027	190.20	22.57	.118664	1.35	2	4	2.2
Tungsten	W	3380	183.85	19.30	.104976	1.37,1.41	3,9	4,6	1.7
Carbon	C	3727	12.01	2.25	.187328	.77	8,4,5	4	2.5

CRYSTAL KEY

1 Face Center Cubic
2 Hexagonal Close Pack
3 Body Center Cubic
4 Hexagonal
5 Rhombohedral
6 Orthorhombic
7 Face Center Tetragonal
8 Diamond
9 Cubic
10 Trigonal
11 Monoclinic
12 Tetragonal

( ) Predicted or Estimated

TABLE II. EXAMPLE EMBRITTLEMENT COUPLES FROM GORDON AND AN (Ref. 28)

Metal	Liquid Metal	Delayed Failure	Reference
4130 Steel	Li	Yes	12
4340 Steel	Cd	Yes	54
4140 Steel	In	Yes	28
Zn (Monoxtals)	Hg	Yes	57
2024 Al	Hg	Yes	12
7075 Al	Hg-3pct Zn	Yes	12
Al-4 pct Cu	Hg-3pct Zn	Yes	12
Cu-2 pct Be	Hg	Yes	53,55
Zn	Hg	No	52
Cd	Hg	No	52
Cd	Hg+In	No	56
Ag	Hg+In	No	56
Al	Hg	No	56

TABLE III. TEST DATA FOR 4142 AND 1045 STEELS IN AIR AND Hg

Specimen	Material	Environment	Hardness	Initial Dia. in.	Final Dia. in.	Red. In Area %	Max. Stress ksi
1	4142	Air	88 RB	.240	.215	19.7	157
2	4142	Hg	86 RB	.253	.235	13.7	162
3	1045	Air	87 RB	.260	.209	35.4	114
4	1045	Hg	87 RB	.250	.211	28.7	114
5	4142	Hg	29 RC	.245	.243	1.60	187
6	4142	Air	28 RC	.260	.208	36.0	212
7	1045	Hg	40 RC	.257	.251	4.60	219
8	1045	Air	39 RC	.238	.210	22.1	218

TABLE IV. STRESS-STRAIN DATA GENERATED FROM MTS PROGRAM WITH 4142 STEEL IN H_2, Hg, AND AIR ENVIRONMENTS

ISR s^{-1}	RC	Env.	YS ksi	SAY %	UTS ksi	SAT %	FS ksi	SAF %	SEY 1000lb-in/in^3	SEF 1000lb-in/in^3	MPW 1000lb-in/in^3	TTF sec.
10^{-5}	47.8	H_2	(275)	(1.03)	47	.20	47	.20	—	.10	—	399
10^{-5}	33.6	H_2	(202)	(.86)	68	.32	68	.32	—	.23	—	980
10^{-5}	21.5	H_2	(141)	(.70)	138	.56	138	.56	—	.72	—	1280
10^{-4}	45.2	H_2	(297)	(1.28)	94	.37	94	.37	—	.37	—	94
10^{-4}	41.9	H_2	(245)	(.79)	92	.38	92	.38	—	.32	—	57
10^{-4}	32.9	H_2	127	.61	128	.69	128	.69	—	.99	—	158
10^{-5}	45.7	Hg	275	1.03	345	3.41	344	3.72	1.99	13.72	9.47	4032
10^{-5}	36.5	Hg	184	.80	197	2.21	169	4.46	.95	7.76	6.81	4453
10^{-5}	23.4	Hg	141	.70	154	3.49	102	9.11	.93	12.24	11.31	8898
10^{-4}	44.9	Hg	297	1.28	329	2.13	329	2.13	2.51	4.86	2.35	347
10^{-4}	43.2	Hg	272	1.11	327	3.04	327	3.04	1.82	7.54	5.72	330
10^{-4}	39.0	Hg	224	.93	250	1.60	250	1.60	1.22	2.79	1.57	232
10^{-4}	35.9	Hg	177	.85	207	2.76	184	4.92	1.42	8.92	7.50	501
10^{-4}	33.3	Hg	154	.83	197	3.12	126	7.78	1.26	17.38	16.12	660
10^{-4}	24.9	Hg	140	.60	156	2.40	102	8.18	.96	13.59	12.63	802
10^{-3}	28.0	Hg	164	.82	178	2.19	—	—	.82	—	—	—
10^{-5}	45.2	Air	275	1.03	345	3.36	271	6.70	1.99	19.61	17.62	6796
10^{-5}	36.6	Air	202	.86	213	2.08	136	7.08	1.19	12.66	11.47	7308
$^{\bullet}10^{-5}$	21.0	Air	141.	.70	161	3.61	101	10.04	.93	13.24	12.31	7872
10^{-4}	48.0	Air	294	1.20	343	3.73	296	5.98	1.99	17.37	15.38	613
10^{-4}	46.4	Air	297	1.28	346	3.43	273	6.50	2.51	19.19	16.68	664
10^{-4}	34.5	Air	195	.90	209	2.67	136	7.10	1.72	12.50	10.78	750
10^{-4}	36.9	Air	213	.93	227	2.23	—	—	1.19	—	—	—
10^{-4}	33.0	Air	182	.82	193	2.38	—	—	.94	—	—	—
—	41.3	Air	245	.79	261	1.68	184	5.78	1.43	13.38	11.95	—

ISR Initial Strain Rate
RC Sample Hardness
Env. Environment
YS .2% Yield Strength
SAY Strain At Yield
UTS Ultimate Tensile Strength
SAT Strain At UTS
FS Fracture Strength
SAF Strain At Fracture
SEY Strain Energy To Yield
SEF Strain Energy To Fracture
MPW Macroscopic Plastic Work
TTF Time To Fracture
( ) Predicted From Air Values
• ISR 27% Faster Than Shown

TABLE V. FATIGUE DATA FROM TESTS IN H_2, Hg, AND AIR AT 30Htz

Environment	Hardness RC	*UTS ksi	Max. Load ksi	Min. Load ksi	Cycles to Fail
Air	34.1	210	185.3	11.9	14270
Hg	33.8	200	139.7	10.2	51280
H_2	33.9	67	46.6	3.7	19010

*Maximum strength in environment under tensile loading.

TABLE VI. ESTIMATE OF FRACTURE TOUGHNESS, K, AND MINIMUM CRACK SIZE

Environment	Strain Rate s^{-1}	Ultimate Tensile Strength ksi			K $ksi\sqrt{in}$			Min. Crack Size in		
		RC 22	RC 35	RC 45	RC 22	RC 35	RC 45	RC 22	RC 35	RC 45
Air	10^{-4}	—	213	346	—	40.6	47.0	—	.0231	.0118
Hg	10^{-4}	—	207	329	—	26.1	16.2	—	.0101	.0015
H_2	10^{-4}	—	128	94	—	4.6	2.4	—	.0008	.0004
Air	10^{-5}	161	209	345	47.9	37.2	46.5	.0566	.0202	.0116
Hg	10^{-5}	154	197	344	41.5	24.3	28.3	.0461	.0096	.0043
H_2	10^{-5}	138	68	47	4.2	1.9	.79	.0006	.0005	.0002

APPENDIX C

DERIVATION OF STRAIN RATE

APPENDIX C

On the MTS system the grips in the mode control of "stroke" will displace 6 inches in the number of seconds displayed in RATE 1. At 50 percent stroke control, the grips displace 3 inches per RATE 1. To calculate strain rate, with f as frequency and t as time, the logarithmic characteristic strain is assumed to be:

$$\text{Strain} = \ln (L_{new}/L_{old}) \qquad 1.$$

The extra displacement in 50 percent stroke control is used to derive the new length, L_{new}.

$$L_{new} = L_{old} + 3'' \cdot \text{frequency} \cdot \text{time} = l_o + 3 \cdot f \cdot t \qquad 2.$$

Taking the derivative of strain with respect to time gives strain rate

$$\text{Strain} = \ln \left(\frac{lo + 3ft}{l_o} \right) \qquad 3.$$

$$\text{Strain Rate} = \frac{d \left(\ln \frac{(l_o + 3ft)}{l_o}\right)}{dt} \qquad 4.$$

$$\text{Strain Rate} = \frac{3 f}{l_o + 3ft} \qquad 5.$$

A time t=0, the initial strain rate is ISR.

$$ISR = 3f/l_o, \quad f = 1/RATE1 \qquad 6.$$

$$RATE1 = 3/l_o ISR \qquad 7.$$

APPENDIX D

DERIVATION OF EQUIVALENT INITIAL LENGTH

APPENDIX D Derivation of Equivalent Initial Length

1. Logic of Equivalent Length

The logic in developing a means of determining the strain in the smallest cross section resulted from the need in determining strain rate in variable geometry specimens. Since most strain will occur in the smallest diameter for a given displacement and since all the geometries are designed to test the smallest diameter portion of a tensile specimen, then all strains are derived in terms of an equivalent length with respect to the smallest diameter. (Note this derivation is for axisymmetric specimens only and area is taken as the longitudinal crosssectional area, not the transverse areas).

For Figure 58.the elastic strains relative to a force applied become:

$$\varepsilon_o = \frac{4F}{(do)^2 E}$$

$$\varepsilon_{l_1} = \frac{16F}{(d_1)^2 E}$$

$$\varepsilon_{l_2} = \frac{4F_2}{(d_1)^2 E}$$

The elastic strain energy over each area A, B, or C can be evaluated as a potential of strain over the length of an effective constant cross section.

If $lo = \Delta l_1 = \Delta l_2$ then

$$\frac{\varepsilon_{l_1}}{\varepsilon_o} = \frac{4d_o^2}{(d_1 + d_o)^2}$$

$$\varepsilon_{l_1} = \varepsilon_o \left(\frac{4d_o^2}{(d_1 + d_o)^2} \right)$$

$$\varepsilon_{l_2} = \varepsilon_o \left(\frac{d_o^2}{d_1^2} \right)$$

$$\text{Total Strain} = \varepsilon_o \left(1 + \frac{4d_o^2}{(d_1 + d_o)^2} + \frac{d_o^2}{d_1^2}\right)$$

APPENDIX D

Since $lo = \Delta l_1 = \Delta l_2$ then the proportion of elastic strain energy varies with respect to length for each diameter.

$$\frac{\varepsilon_o}{lo} \simeq \frac{\varepsilon_{l_1}}{l_1} \simeq \frac{\varepsilon_{l_2}}{l_2}$$

$$\varepsilon_{l_1} = \frac{\Delta l_1}{lo} \quad \varepsilon_o \frac{4do^2}{(d_1+do)^2}$$

$$\varepsilon_{l_2} = \frac{\Delta l_2}{lo} \quad \varepsilon_o \frac{do^2}{d_1^2}$$

$$\varepsilon_{\text{total elastic strain}} = \varepsilon_o \left(1 + \frac{\Delta l_1}{lo}\frac{4do^2}{(d_1+do)^2} + \frac{do^2}{d_1^2}\frac{\Delta l_2}{lo}\right)$$

By assuming a compensated lo', that is the equivalent length with a crosssection of do, the total strain may be calculated for the elastic range of tension.

$$\frac{\text{total elastic strain}}{lo'} = \frac{\varepsilon_o}{lo}$$

Therefore the equivalent length becomes

$$lo' = lo \left(1 + \frac{\Delta l_1}{lo}\frac{4do^2}{(d_1+do)^2} + \frac{\Delta l_2}{lo}\frac{do^2}{d_1^2}\right)$$

For a more accurate and simplified version of the equivalent length, the transition zone from d_1 to do is examined.

2. Two Point Polynomial Interpolation for simple angle geometry.

An example of simple angle geometries is given in fig. 59.

APPENDIX D

The diameter at 1 is do while the diameter is d_1 at 4. Area A is easily calculated.

Total Area A $=(l_1-lo)\ do$

To calculate the area of B an equation for the line passing from pt. 1 to pt. 4 is derived using two pt. interpolation.

$r_1 = do/2$; $r_4 = d_1/2$; $x_1 = lo/2$; $x_4 = l_1/2$

$p_1(r) = Po(r) + c_1 (r - r_1)$

$p_1(r) = Po/_2 + c_1(r - do/_2)$

at $r = r_4$

$l_1/2 = lo/2 + c_1 \quad d_1/2 - do/2)$

$c_1 = (l_1 - lo)/(d_1 - do)$

$p_1(r) = lo/2 + c_1 (r - do/2)$

Finally, integrate $p_1\cdot(r)$ to get the area of B

$$\text{Area B} = \int_{o}^{d_1-do} (lo/2 +(r-do/2)(l_1-lo)/(d_1-do))dr$$

$$\text{Area B} = (d_1-do)lo/2 + (d_1-do)^2(l_1-lo)/(d_1-do) - (d_1-do)(l_1-lo)/(d_1-do)(do/2)$$

$$\text{Area B} = .5\ (lo(d_1-do) + (l_1-lo)(d_1-do) - do(l_1-lo))$$

Combining A and B and multiplying Area B by two gives the total area right side and left side of the tensile specimen.

APPENDIX D

If this total area were a longitudinal crossection area of a simple cylinder of diameter or side d_1 then the length of the cylinder becomes the following, l_2'.

$$l_2' = (l_1(d_1-do))/d_1$$

The equivalent length then becomes the following.

$$lo' = lo + (l_2' + l_2)(do/d_1)^2$$

3. Three point method for parabolic geometry or a stress concentrator geometry or a stress concentrator geometry. Examples of these geometries is given in figure 60.

The logic is similar to that of the two point method but two extra measurements are necessary. At point 2 measure the diameter, d', and the length from point to point, l'.

$r_1 = do/_2$; $r_2 = d'/2$; $r_4 = d_1/2$; $x_1 = lo/2$; $x_2 = l'/2$

$x_4 = d_1/2$

Total Area $A = do\ (l_1-lo)$

Using three point interpolation the equation of the line passing through points 1, 2 and 4 is derived.

$$P_1(r) = Po(r) + (r-r_1)c_1$$

$$P_2(r) = P_1(r) + (r-r_1)(r-r_2)c_2$$

$$P_1(r) = x_1 + (r-r_1)c_1 \qquad c_1 = (x_2 - x_1)/(r_2-r_1)$$

$$P_2(r) = x_1 + (r-r_1)c_1 + (r-r_1)(r-r_2)c_2$$

$$c_2 = (x_4-x_1-(r_4-r_1)(x_2-x_1)/(r_2-r_1))/((r_4-r-1)(r_4-r_2))$$

APPENDIX D

Next integrate $p_2(r)$ and substitute values of length and diameter.

$$\text{Area of B} = \int_0^{d_1-do} p_2(r)dr$$

$$= lo(d_1-do)/2 + (.5(d_1-do)^2(do/2)(d_1-do)(l'-lo)/(d'-do) + 2((d_1-do)^3/3-(do+d')(d_1-do)^2/4 + do\ d'(d_1-do)/4))c_3$$

$$c_3 = (l_1-lo-(d_1-do)(l'-lo)/(d'-do))/((l_1-lo)(l_1-l'))$$

Simplifying and multiplying area B by two and combining with area A the longitudinal crosssectional area, TCA becomes:

$a = l_1-lo$
$b = d_1-do$
$c = (l'-lo)/(d'-do)$
$d = do + d'$
$e = do\ d'$
$f = l'$

$$TCA = do\ a + lo\ b + b^2c-do\ b\ c + (4b^3/3-d\ b^2 + e\ b)(a-b\ c)/(a\ f)$$

If TCA were a cross section of a simple cylinder of diameter or side d_1 the length of the cylinder becomes l_2'.

$$l_2' = TCA/d_1$$

Equivalent length then becomes:

$$lo' = lo + (l_2' + l_2)(do/d_1)^2$$

In the case of the stress concentrator, figure 61, geometry where lo = 0.0 then equivalent length is simply $(l_2' + l_2)(do/d_1)^2 = lo'$. (If the radius of curvature is needed for the stress concentrator specimen the following equation from figure D-4 provides a quick means of calculating it.)

$$R = (L_2^2 + L_1^2)/(2L_2)$$

Figure 58. Axisymetric Sample of Constant Diameter, do

Figure 59. Example of Simple Angle Geometries for 2 Point Method

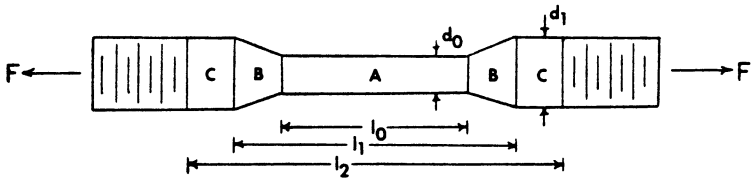

($\Delta l_1 = l_1 - l_0$, $\Delta l_2 = l_2 - l_1$)

Figure 58.

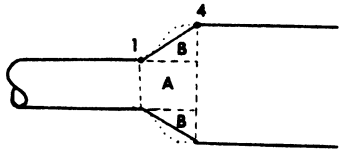

Figure 59.

Figure 60. Dimensions in 3 Point Method on Several Method Geometries

Figure 61. Figure for Calculating Radius of Curvature

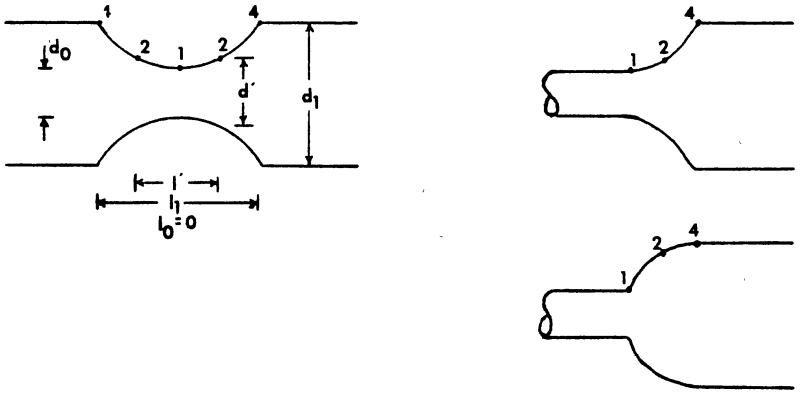

Figure 60.

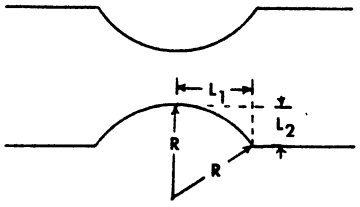

Figure 61.

APPENDIX E

CALCULATION OF ELECTROLYTE AREA

APPENDIX E Calculation of Electrolyte Length

For a cylindrical sample of constant diameter, do, the ideal length, LA, of sample to expose to the electrolyte under a constant charging rate, C.C.R, is calculated the following way.

Area exposed to electrolyte = π do LA

Ammeter Reading = AR

$$LA = AR/(CCR \ \pi \ do) \qquad 1.$$

Experimental Values were C.C.R = 200 amps/m^2

A.R. = $50 \cdot 10^{-3}$amps

do = .2 in

1 = 1550 in^2/m^2 *(constant)

$$LA = (.1233/do) \text{ inches} \qquad 2.$$

APPENDIX F

LISTING OF MTS STRESS-STRAIN PROGRAM

APPENDIX F

MTS STRESS - STRAIN PROGRAM

```
 5   INPUT "NUMBER OF POINTS ="; M
 9   DIM P(25), D(25)
10   DIM SS(25), SN(25)
11   DIM MOD (25)
15   INPUT "SMALL DIA.="; DO
20   INPUT "LARGE DIA.="; D1
25   INPUT "SECTION LENGTH="; LO
30   INPUT "MACHINED LENGTH="; L1
35   INPUT "GRIP TO GRIP LENGTH =;12
40   DL2 = L2-L1
45   DL2P = (L1-LO) * (2 * D1-DO)/D1
50   G = (DO/D1) * (DO/D1)
55   LOP = LO + G * (DL2 + DL2P)
56   LAK = LO/LOP
60   PRINT "EQUIVALENT LENGTH"; LOP
61   PAUSE
64   Y = 1
65   YES = 1
69   N = 0
70   NO = 0
71   POFF = .002
74   CP = 3.141592654
75   CN = .471404521
80   INPUT "INPUT NEW M VALVE?"; DEL
```

APPENDIX F

```
 81  IF DEC=1 THEN INPUT "M=";M
 85  FOR I = 1 TO M
 90  PRINT "1="; I
100  PAUSE 1
105  INPUT "LOAD"="; P(I)
106  INPUT "DISPLACEMENT="; D(I)
110  NEXT I
115  INPUT "CALCULATE ZLD?"; XDEC
116  IF XDEC = 0 THEN GOTO 250
120  J = 0
125  I = 1 + J
135  ZLD = D(I+1) - (P(I+J)* (D(I+J))/(PCI+J))
136  PRINT "ZLD="; ZLD
137  PAUSE
145  IF ZLD>D(1) THEN GOTO 155
150  ZLD1 = ZLD
155  ZLD = ZLD1
160  IF P(I+2) - P(I+J) = 0 THEN GOTO 215
165  ZLD = D(I+2) - P(I+2)*(D(I+2) - D(I+J))/(P(I+2) - P(I+J))
170  IF ZLD<D(1) THEN GOTO 180
175  IF ZLD>ZLD1 THEN GOTO 205 ELSE GOTO 190
180  ZLD = ZLD1
190  IF ZLD<0 THEN GOTO 240
195  J = J + 1
200  IF I = M-1 THEN GOTO 240 ELSE GOT 125
205  IF ZLD<0 THEN GOTO 225
```

APPENDIX F

```
210  ZLD1 = ZLD
215  I = I + 1
220  GOTO 235
225  IF 1>10 THEN GOTO 240
230  GOTO 210
235  IF I<M-1 THEN GOTO 130
240  ZLD = ZLD1
245  GOTO 265
250  INPUT "INPUT ZLD?"; DEC
255  IF DEC = 0 THEN GOTO 265
260  INPUT "YOUR ZLD ESTIMATE="; ZLD
265  PRINT "ZLD WILL BE ="; ZLD
270  PAUSE
275  PRINT "NOW, WE CALCULATE STRESSES"
280  PAUSE .7
285  PRINT "AND STRAINS"
290  PAUSE .8
295  PRINT "DO YOU WISH"
300  PAUSE .8
305  PRINT "TO PRINT STRESSES"
310  PAUSE .8
315  INPUT "AND UNCOMPENSATED STRAINS?"; DEC
320  FOR I = 1 TO M
330  SS(I) = 4*P(I)/((DO*DO)*CP)
335  SN(I) = CN*(CD(I) - ZLD)/LOP
340  NEXT I
```

APPENDIX F

```
345  IF DEC = 0 THEN GOTO 371
350  FOR I=1 TO M
355  PRINT "ENG. STRESS"; I; SS(I)
356  PAUSE
360  PRINT "ENG. STRAIN"; I; SN(I)
361  PAUSE
362  NEXT I
371  FOR I = 1 TO M
372  PRINT "ENGR. STRESS="; I; SS(I)
373  PAUSE .3
374  PRINT "ENGR. STRAIN="; I; SN(I)
375  PAUSE .3
376  NEXT I
380  PRINT "NOW WE CALCULATE"
385  PAUSE I
390  PRINT "THE MODULUS OF ELASTICITY"
395  PAUSE 1
400  Z = 0
401  J = J + 1
402  IF J = M - 1 THEN GOTO 439
405  X = (SS'J+1) - SS(J))/(SN(J+1) - SN(J))
410  Z = Z + X
415  MOD(J) = Z/J
420  IF J = 1 THEN GOTO 401
425  W = MOD(J)/MOD(J-1)
426  PRINT "MOD(J-1)"; J; MOD(J-1)
```

APPENDIX F

```
427  PAUSE
435  IF W>.93 THEN GOTO 401
439  U = 0
440  FOR I = 1 to J
445  E = MOD(I)
450  U = U + E
455  NEXT I
460  E = U/J
465  U = MOD(1)
466  FOR I = 2 TO J
467  V = MOD(I)
468  IF V>U THEN U = V
469  NEXT I
470  PRINT  :HIGHEST INCREMENTAL MODULUS="; U
471  PAUSE
476  PRINT "AVG. ELASTIC MODULUS="; E
477  PAUSE
478  INPUT "USE HIGHEST INCR. MOD.?"; DEC
479  IF DEC = 1 THEN E = U
480  PRINT "J"; J
481  PAUSE
485  IF J<3 THEN PRINT "THAT'S ALL FOLKS" ELSE GOTO 495
486  PAUSE
487  GOTO 850
495  PRINT "NOW, WE CALCULATE"
500  PAUSE .6
```

APPENDIX F

```
505  PRINT "THE YIELD STRENGTH"
506  PAUSE .6
507  I = 0
508  K = J
510  SAY = (SN(K) + SN(K-1))/2
511  PRINT "SAY="; SAY; K
512  PAUSE
527  INPUT 'CHOOSE INFLECTION PT.?"; DEC
528  IF DEC = 1 THEN INPUT "J="; K
537  IF K = M-1 THEN GOTO 660
538  AN = SN(K-2)
539  BN = SN(K-2)
540  COX = SS(K-2)
545  C1X = (SS(K-1) - SS(K-2))/(SN(K-1) - SN(K-2))
546  Q = (SN(K) - SN(K-2) * (SN(K) - SN(K-1)
550  C2X = (SS(K) - SS(K-2) - C1X * (Sn(K) - SN(K-2)))/Q
551  PRINT "K"; K
552  PAUSE
555  XSN2 = SN(K)
560  XSN1 = SN(K-1)
565  I = I + 1
570  HSN = (XSN2 + XSN1)12
575  SSY = E X (HSN - POFF)
580  SSP = COX  + C1X*(HSN-AN) + C2X*(HSN-AN)*(HSN-BN)
585  DC = SSP - SSY
590  IF DC>0 THEN XSN1 = HSN
```

APPENDIX F

```
595  IF DC = 0 THEN SAY = HSN
600  IF DC<0 THEN XSN2 = HSN
605  DD = ABS(1-SSP/SSY)
610  IF DD<.03 THEN GOTO 640
620  IF I>15 THEN GOTO 640
630  GOTO 565
640  SAY = HSN
650  YS = (SAY - POFF*E
660  PRINT "STRAIN AT YIELD="; SAY
665  PAUSE
670  PRINT "YIELD STRENGTH="; YS
671  PAUSE
674  INPUT "SATISFIED WITH YIELD?"; DEC
675  IF DEC = 0 THEN GOTO 527
676  INPUT "DO MODULUS AGAIN?"; DEC
677  IF DEC = 1 THEN INPUT "MODULUS="; E
678  INPUT "INPUT YOUR MODULUS?"; DEC
679  IF DEC = 1 THEN INPUT "MODULUS="; E
680  IF DEC = 1 THEN GOTO 507
681  INPUT "VARY PCT. OFSET:"; DEC
682  IF DEC = 1 THEN INPUT "POFF="; POFF
683  IF DEC = 1 THEN 507
690  INPUT  :CHOOSE A SAY?"; SAY
695  IF DEC = 1 THEN INPUT "SAY="; SAY
696  YS = (SAY-POFF)*E
697  PRINT "YS="; YS
```

APPENDIX F

```
698  PAUSE
700  SSM = YS
701  INPUT "DO MODULUS AGAIN?"; DEC
702  IF DEC = 1 THEN GOTO 678
710  LX  = LO*(1+SAY)
715  PRINT "SECTION LENGTH AT YIELD="; LX
720  PAUSE
725  J = 0
730  J = J + 1
735  IF SN(J)<= SAY THEN GOTO 730
736  SN(J) = (D(J)-ZLD)/LX - SAY
738  IF SS(J-1)<SS(J) THEN SSM = SS(J)
739  IF SS(J-1)<=SS(J) THEN SN(J) = SN(J)*LAK*EXP(YS/SS(J)-1)
740  IF SS(J-1)>SS(J) THEN SN(J) = SN(J)*(1-EXP(1-SS(J)/SSM))
741  IF SS(J-2) >SS(J) THEN SN(J) = LAK*((D(J)-ZLD)/LX-SAY)
745  IF J<M THEN GOTO 730
750  I = 0
755  I = I + 1
760  PRINT "THE COMPENSATED"
761  PAUSE .6
763  PRINT "STRESSES AND STRAINS"
764  PAUSE .5
765  PRINT "SS(I)="; I; SS(I)
766  PAUSE
770  PRINT "SN(I)=; SN(I); I
771  PAUSE
```

APPENDIX F

```
775  IF I<M THEN GOTO 755
780  INPUT "DO YIELD AGAIN?"; DEC
781  IF DEC = 1 THEN 674
840  INPUT "START OVER?"; DEC
845  IF DEC = ! THEN 80
850  STOP
860  END
```

APPENDIX G

CALCULATION OF FRACTURE TOUGHNESS

APPENDIX G Calculation of Fracture Toughness

Fracture toughness, K, and critical minimum crack size, df, are calculated by modifying Griffith's equation for cylindrical constant diameter samples.

$$K = \sqrt{EG} \qquad (1.)$$

E is Young's Modulus

G is Macroscopic Energy to Fracture

In calculating fracture toughness values the value of fracture energy is estimated by multiplying the area under the stress-strain curve, SEF, by the approximate change in volume of the sample, Vc.

$$Vc = (FD - ZLD)\ \pi\ (do)^2/4 \qquad (2.)$$

FD is Displacement at Fracture

ZLD is Zero Load Displacement

do is iniital diameter

$$G = Vc \cdot SEF \qquad (3.)$$

SEF is Strain Energy to Fracture from Stress Strain Curve.

After calculating values of K, another equation by Griffith is adopted to calculate the critical minimum crack size by using the conservative value of Ultimate Tensile Strength as the fracture stress, F.S.

$$K = F.S.\ \sqrt{\pi a} \qquad (4.)$$

a is one half the minimum crack size

$df = 2 \cdot a$

F.S. = UTS

$$df = 2(K/UTS)^2/\pi \qquad (5.)$$

VITA 2

Richard Gary Norman

Candidate for the Degree of

Master of Science

Thesis: COMPARISON OF LIQUID MERCURY AND HYDROGEN EMBRITTLEMENT ON 4142 STEEL

Major Field: Mechanical Engineering

Biographical:

Personal Data: Born in Denver, Colorado, December 30, 1956, the son of Richard C. and Elizabeth J. Norman.

Education: Graduated from Jenks High School, Jenks, Oklahoma in May, 1975; received Bachelor of Science in Mechanical Engineering Degree from University of Tulsa in May, 1982; Completed requirements for Masters of Science degree at Oklahoma State University in December, 1984.

Professional Experience: Member of American Society of Mechanical Engineers.